2014

A novel approach to central-jet forward-hadron correlations in proton-proton collisions at 200 GeV at the PHENIX experiment

Joshua Paul Perry
Iowa State University

Recommended Citation

Perry, Joshua Paul, "A novel approach to central-jet forward-hadron correlations in proton-proton collisions at 200 GeV at the PHENIX experiment" (2014). *Graduate Theses and Dissertations*. 14209.
http://lib.dr.iastate.edu/etd/14209

A novel approach to central-jet forward-hadron correlations in proton-proton collisions at 200 GeV at the PHENIX experiment

by

Joshua Paul Perry

A dissertation submitted to the graduate faculty
in partial fulfillment of the requirements for the degree of
DOCTOR OF PHILOSOPHY

Major: Nuclear Physics

Program of Study Committee:

John Lajoie, Major Professor
Craig Ogilvie
Soeren Prell
Adam Kaminski
Mani Mina

Iowa State University

Ames, Iowa

2014

DEDICATION

This thesis is dedicated to my wife, Sarah, and our families for their unwavering support and encouragement.

TABLE OF CONTENTS

LIST OF TABLES

LIST OF FIGURES

ACKNOWLEDGEMENTS

I would like to acknowledge the continuous support and encouragement by my advisor John Lajoie. His unfailing optimism made this research experience much more enjoyable and possible.

I would also like to acknowledge and thank the PHENIX collaboration for being a welcoming group of researchers, Arbin Timilsina for his helpful insights and discussions, and Chris Wilson of Grinding Gear Games for his excellent creation and direction of a much needed stress relief system.

ABSTRACT

The results of Semi-Inclusive Deep Inelastic Scattering and Deep Inelastic Scattering experiments combined in a global analysis have shown us that a transversely polarized quark undergoes an azimuthal spatially-biased neutral pion fragmentation. One goal of the PHENIX experiment at RHIC is to study similar properties in a hadron-hadron collision environment in an attempt to show the degree to which universality is broken between these differing systems as well as the relative contribution of competing processes to the observed single spin asymmetries. A novel measurement method was formulated specifically for the PHENIX experiment's detector configuration. The method and results are presented here.

CHAPTER 1. INTRODUCTION

The structure of a proton is a complex set of emergent properties born from the basic interactions of Quantum Chromodynamics (QCD) and Quantum Electrodynamics (QED). The study of these emergent (phenomenological) properties allows one to infer basic QCD principles; specifically, the way in which the phenomenological properties arise from various initial states allows one control and variance over which specific QCD principles are tested. The emergent property studied here is the quantum mechanical spin of a proton.

1.1 Goal

The goal of this research is to solve a puzzle which directly correlates to our understanding of QCD. The specific puzzle chosen is a spatial bias in particle production in polarized proton-proton collisions. Simply, when polarized protons collide they eject particles, one of which is the neutral pion (π^0). It has been observed in previous measurements that the spatial-density of neutral pions ejected from the collision depends on the orientation of the proton polarization vector from which the neutral pion was ejected. A schematic representation of such a process can be seen in Figure 1.1

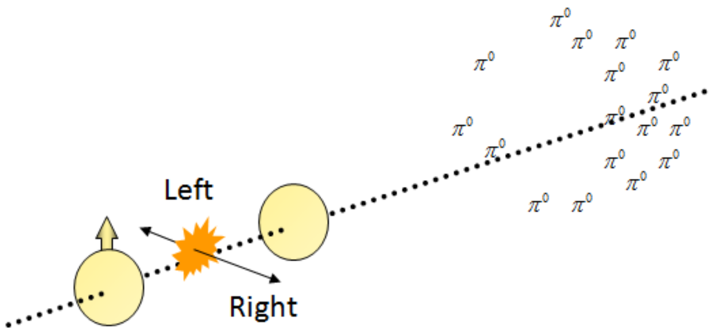

Figure 1.1 Schematic of a simplified polarized proton-proton collision producing a spatially-biased neutral pion distribution. In this example more π^0s are found to the "right" of the spin axis than to the "left" of the spin axis.

To understand how the proton spin correlates to the proton structure itself we must first understand the basic qualitative properties of QCD as well as the basic (non-spin-dependent) proton structure. Presented in this introduction chapter is a purely qualitative conceptual overview of the large-distance (greater than half a fermi) bulk properties of QCD.

1.2 QCD and QED Comparison

As a basis for comparison one can consider the case of QED in which the gauge boson (force mediator) is the photon. The photon itself carries no electromagnetic charge and is thus non-self-interacting (at leading order). As such, the electric potential falls as a function of separation distance ($V \sim \frac{1}{r}$) and the force between two electromagnetic charges falls as a function of separation distance ($F \sim \frac{1}{r^2}$). A schematic representation of the electric field lines between two point charges can be seen in Figure 1.2.

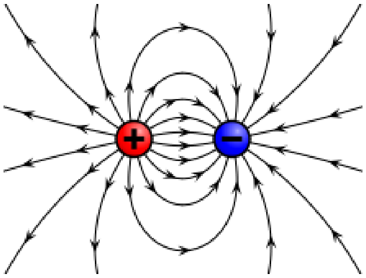

Figure 1.2 Schematic of electric field lines between two point charges [1].

Almost disparately, the QCD force is mediated by the gluon which does carry QCD charge (color charge) which in turn enables the gluon to self-interact (Figure 1.3). Gluon-gluon interactions being possible at leading order causes the potential field lines between two color charged objects to form a "tube" rather than the classical QED picture as seen in Figure 1.5. The effect of this difference between QED and QCD results in the QCD potential (Figure 1.4) to grow as a function of (large) separation distance ($V \sim k \cdot r$) like a classical mechanical spring system. Through Newton's Second Law of Motion we know that the correlation between scalar potential and force is simply a spatial gradient ($\overrightarrow{F} \sim -\overrightarrow{\nabla} V$); consequently, the (large distance) force between two QCD point charges remains constant as a function of separation distance.

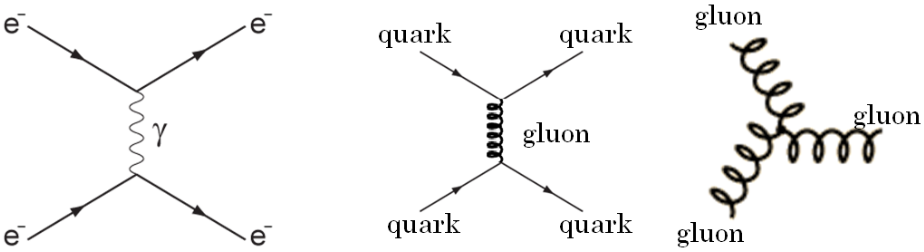

Figure 1.3 Feynman diagrams of leading order interactions. Left-most: QED, Right two: QCD.

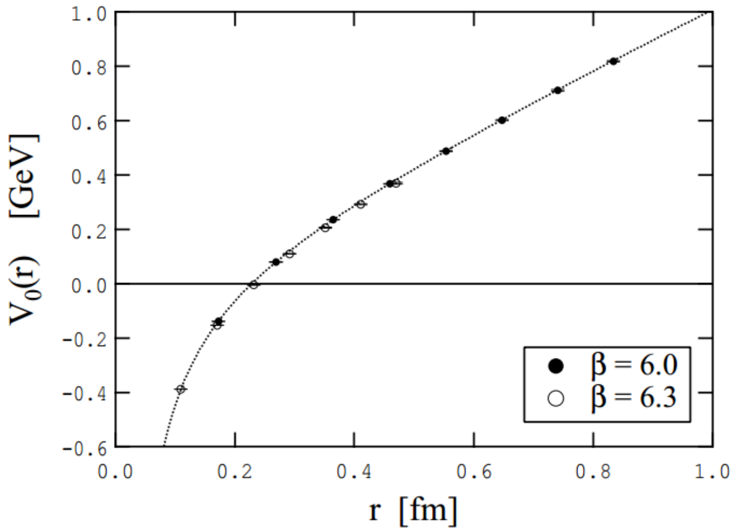

Figure 1.4 Lattice determination of the large-distance QCD potential [2].

Since the force remains constant, the work (energy) required for separation grows as the line-integral of the separation distance which implies that the energy stored in the QCD flux-tube connecting the two QCD objects grows as the objects are separated as can be seen in Figure 1.5. Just like in the QED vacuum, the QCD vacuum continuously undergoes vacuum excitation to create particle-antiparticle pairs. In the QCD vacuum one can consider the vacuum excitation of virtual quark-antiquark pairs, which, in the large (stored) energy density of a QCD flux tube allows for the easy conversion of a said virtual particle pair into a real quark-antiquark pair rather than being instantly re-converted to vacuum energy. The process by which the QCD vacuum "steals" energy from the flux tube to create particle-antiparticle pairs is called "string breaking," a schematic representation of which can be seen in Figure 1.6.

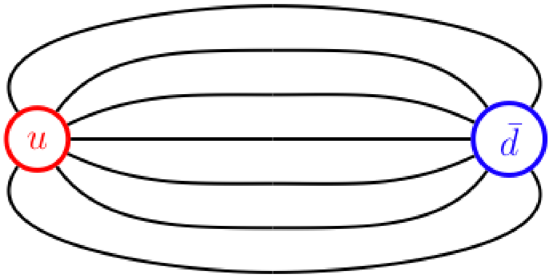

Figure 1.5 Schematic representation of the flux "tube" formed between color charged particles [3].

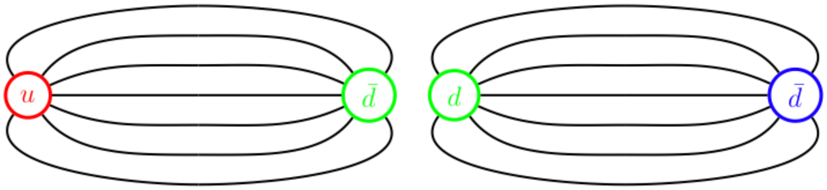

Figure 1.6 Schematic representation of "string breaking" [3].

Since the proton is a composite object comprised of partons (quarks and gluons) it will serve as our laboratory for studying QCD phenomenology. A schematic of the naive parton model of a proton can be seen in Figure 1.7. The proton contains both small-distance and large-distance QCD phenomena, making it an excellent choice for studying QCD itself. Our chosen method of study is to collide protons at (near) the speed of light and analyze what comes out.

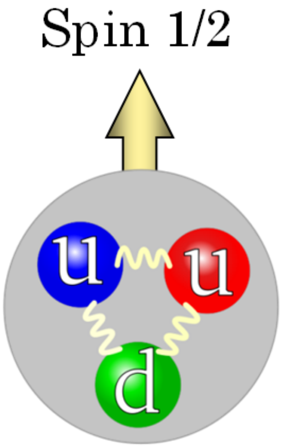

Figure 1.7 Naive quark-parton model proton schematic.

The net effect of this QCD flux-tube formation is that if a single parton attempts to leave the confines of a proton during a collision it pulls these QCD "strings." This means that the parton sees a large (constant) restoring force while its energy is converted to QCD potential energy in the flux tube that is formed. Once the flux tube is high enough energy density the QCD vacuum itself can steal energy from the flux tube for the creation of quark-antiquark pairs. As the parton continues to attempt to leave the confines of the proton this process repeats until no appreciable kinetic energy remains. This process is the result of confinement; simply, the universe does not allow a color charge to roam free, it must be bound into a net colorless state. The system is then left with many quarks and anti-quarks which can form colorless bound states (hadrons). These colorless bound states do not cause the same string-pulling effect and are able to leave the confines of the proton. This process is called "fragmentation" or "hadronization" and this specific effect is the main focus of this work and will be discussed in subsequent chapters.

CHAPTER 2. OVERVIEW

The results of Semi-Inclusive Deep Inelastic Scattering (SIDIS) and Deep Inelastic Scattering (DIS) experiments combined in a global analysis have shown us that a transversely polarized quark undergoes an azimuthal spatially-biased neutral pion fragmentation. One goal of the PHENIX experiment at RHIC is to study similar properties in a hadron-hadron [4] collision environment in an attempt to show the degree to which the universality of fragmentation processes is broken between these differing systems as well as the relative contribution of competing processes to an observed single spin asymmetries [5]. The specific effect and quantity of interest studied in this work is the Collins Effect's spatial bias on neutral pion production.

The Collins Effect, however, cannot be studied in insolation in a hadron-hadron collision environment. The hadrons' initial state parton configurations influence the final state particle production greatly. This measurement will utilize final-state particle kinematic biases to garner some control over the hadrons' initial states during the collision to enhance our measurement's purity. Since our quantity of interest is a spin-dependent quantity which depends greatly on the initial-state parton configuration we will examine that aspect first.

2.1 Spin Structure of the Proton

The proton's leading-order collinear hadronic structure at leading twist (Figure 2.1) is made of three components: the unpolarized Parton Distribution Function (PDF), the helicity distribution, and the transversity distribution. The collinear picture is one in which no partonic transverse momentum is considered. Of particular interest to this measurement are the proton's unpolarized PDF and transversity distribution; the helicity distribution is not probed in this measurement. The proton's unpolarized PDF is known quite well from past measurements (Section 2.1.1). The transversity distribution is essentially the last piece of the collinear partonic jig-saw puzzle to complete the total leading-order hadronic picture.

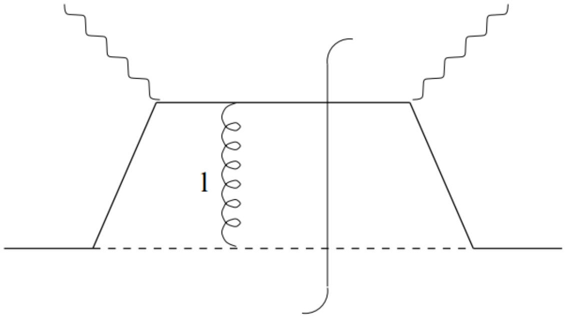

Figure 2.1 Diagram of a SIDIS interaction at leading twist order (one allowed exchange gluon) [6]. Straight lines are quarks, wavy lines are photons, the curly line is a gluon, and "1" represents the exchange gluon.

2.1.1 Parton Distribution Functions

The parton distribution function (PDF) of interest here is the unpolarized proton PDF. A PDF is a distribution function (number density) of partons within a hadron at a specific partonic momentum fraction (x, Equation 2.1). A PDF for each parton flavor (including anti-quarks) as a function of partonic momentum fraction as well as a function of interaction momentum transfer (Q) has been measured from previous experiments. The Naive Parton Model utilizes Bjorken scaling which dictates that the PDF is only a function of x, however, this is not valid at either low or high values of x [7].

$$x = \frac{\overrightarrow{p}_{parton} \cdot \hat{p}_{proton}}{|\overrightarrow{p}_{proton}|} \tag{2.1}$$

The vast majority of high-precision data used in PDF global fits comes from Deep Inelastic Scattering (DIS) experiments. The basic premise of DIS is the scattering of a lepton off of a hadron at energies such that the hadron's constituent partons can be probed via an exchange of a virtual photon. The energy required for the scattering is large enough that the hadron undergoes break-up during the interaction (i.e. inelastic scattering). The measurements performed in a

DIS experiment are fully inclusive measurements; only the initial lepton, initial hadron, and final lepton states are known or observed. The rest of the collision products in the interaction are ignored. A Feynman diagram of a DIS interaction is shown in Figure 2.2.

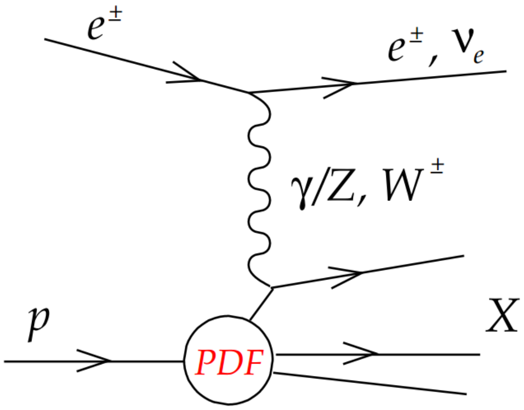

Figure 2.2 Diagram of the neutral and charged-current channels of a Deep Inelastic Scattering process where “X” denotes the hadronic final state [8].

Figure 2.3 shows the CTEQ6M extraction of the proton PDFs at two different energy scales [9]. The nomenclature oft used for the PDF number density is $f_h^p(x, Q^2)$, where “h” is the hadron species and “p” is the parton flavor.

The evolution of the PDF between energy scales is governed by the partonic splitting and recombintation functions [10] used in the DGLAP (Dokshitzer–Gribov–Lipatov–Altarelli–Parisi) evolution scheme [11]. The DGLAP evolution scheme is applicable in the perturbative regime where the QCD coupling constant ($\alpha_s(Q^2)$) is small, i.e. at large momentum transfer. The DGLAP scheme is required to match the experimental Q^2 of an interaction with an appropriately evolved PDF for that energy scale.

The naive quark-parton model provides a probabilistic interpretation of the hadronic structure. The PDF can be normalized to the total number of partons as a function of x such that the PDF can be sampled as a probability density function. The analysis presented here exploits features of the unpolarized PDFs extensively. Specifically, it relies on the fact that a central-going (predominantly perpendicular to the beam-axis) parton is likely sampled from low-x in

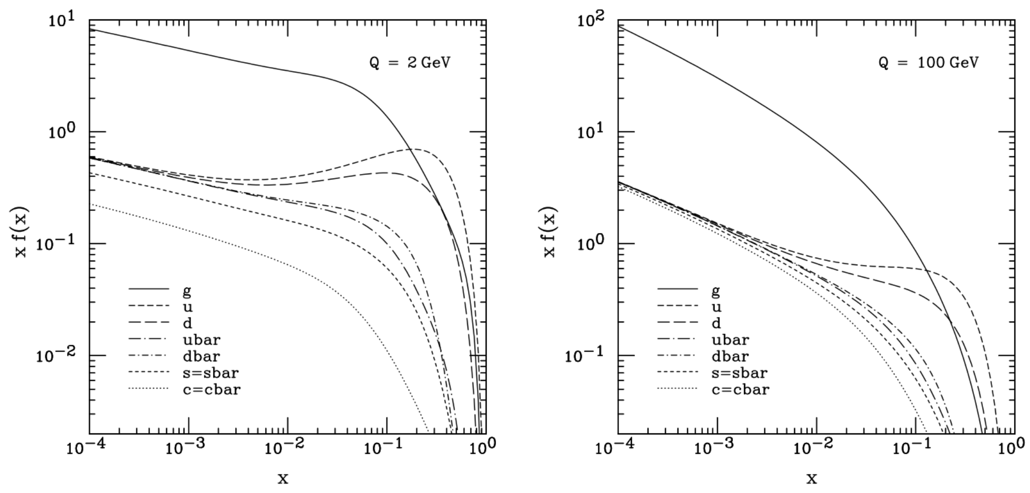

Figure 2.3 The CTEQ6M extractions of the proton PDFs. Left: Q = 2 GeV. Right: Q = 100 GeV.

the PDF which biases it to be a gluon rather than a quark (or anti-quark); also, a forward-going (predominantly parallel to the beam-axis) high-p_T particle biases the same-side-going parton to higher-x, which biases it toward quark flavors and away from the large gluon distribution.

2.1.2 Transversity

The transversity distribution describes the density of transversely polarized quarks (of a specific flavor) in a transversely polarized nucleon. The nomenclature used here for the transversity distribution is $\delta q(x)$, which describes the distribution of quark flavor "q" at a partonic momentum fraction "x". $\delta q(x)$ performs the same role as $q(x)$ in our unpolarized PDFs except now the density is weighted by the relationship between the parton and parent hadron's transverse spin directions.

Transversity is a leading-twist (one exchange gluon, Figure 2.1) partonic distribution function which is time-reversal-odd [12], making it an unobservable quantity unless coupled with another t-odd quantity. This requirement makes it impossible to extract the transversity distribution from DIS experiments alone [13]. A few candidates for coupled measurement include the Collins function (time-reversal-odd), double transverse spin asymmetry using the Drell-Yan processes, and transversity itself [14]. Since the gluon does not have a transversity distribution (massless, spin-1) it is much easier to separate out the quark and gluon components of a SIDIS measurement if it involves spin-polarized hadrons [13].

The most accessible channel for measurement of the transversity distribution is the azimuthal asymmetry in SIDIS processes ($\ell p^{\uparrow} \to \ell h X$) which convolutes the transversity distribution with the Collins function. A global analysis [15] which combines data from the HERMES, Belle, and COMPASS collaborations lead to the first breakthrough in transversity measurement (coupled with the Collins function). In reality, there should exist a transversity distribution for each parent hadron type and parton flavor, however, current data only allows for the extraction of the up and down quark transversity distributions. The latest extraction of the transversity distributions can be seen in Figure 2.4. The maxima/minima seen at $x \approx 0.3$ are primarily do to the chosen parameterization function coupled with the boundary condition that transversity must be zero at $x = 1$. The sign of the transversity value implies that the up-quark (down-quark) favors aligning parallel (anti-parallel) to the proton spin axis.

2.2 Single Spin Asymmetry

A single spin asymmetry in proton-proton collisions is defined as a difference in cross-sections for processes based on the polarization of colliding protons (Equation 2.2).

$$A_N = \frac{d\sigma^{\uparrow} - d\sigma^{\downarrow}}{d\sigma^{\uparrow} + d\sigma^{\downarrow}} \tag{2.2}$$

where $\sigma^{\uparrow,\downarrow}$ is the cross section for a $p^{\uparrow,\downarrow} + p^{unpol} \to \pi^0 + X$ process and the differential represents a derivative with respect to three-space momentum of the π^0. Previous measurements of the π^0 (or unidentified neutral cluster) A_N at the PHENIX experiment can be seen in Figure 2.5 provided by Reference [16]. One can see a large asymmetry in the distribution of unidentified neutral clusters that increases as a function of $x_F = \frac{\overrightarrow{Cluster}_z}{\overrightarrow{Proton}_z}$.

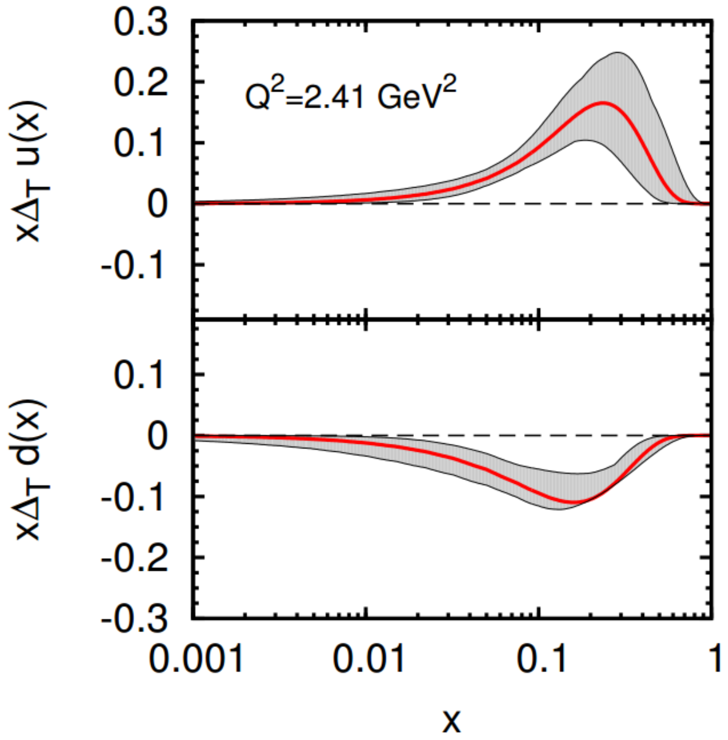

Figure 2.4 Anselmino group transversity distribution extractions ($x\Delta_T q(x) = x\delta q(x)$) [15]. The red line represents the function value with their associated uncertainty bands. Top: Up quark. Bottom: Down quark.

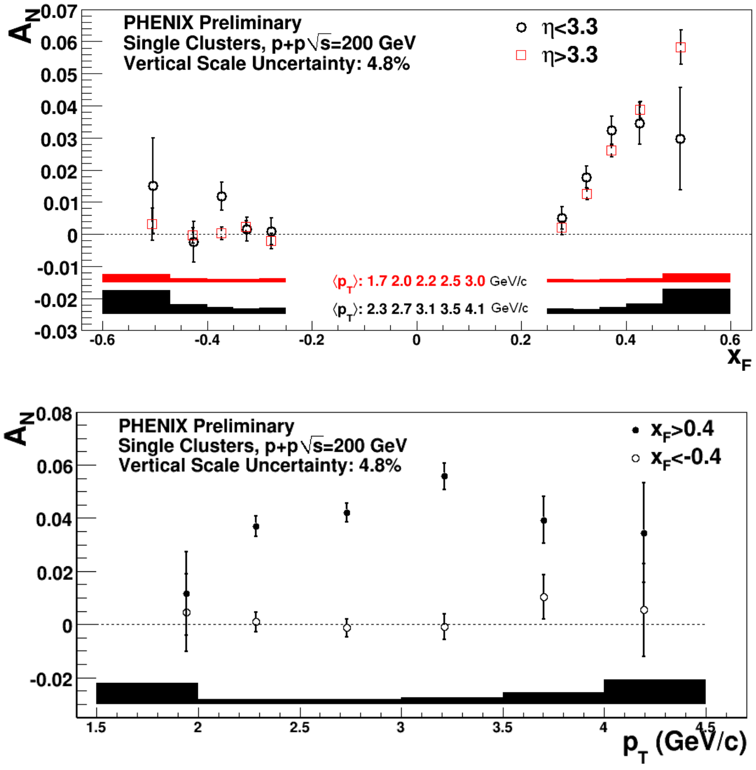

Figure 2.5 Single spin asymmetry of unidentified single clusters at forward rapidity at the

This asymmetry could have several possible contributions. The two main avenues of interpretation are the transverse momentum dependent (TMD) factorization approach and the collinear twist-three factorization approach [17]. The analysis and discussion herein utilizes the TMD factorization approach. The TMD factorization approach states that an observed single spin asymmetry is caused by a correlation between the spin and transverse momentum of the final-state hadron and its parent parton. This correlation manifests as the Collins and transversity coupling (Sections 2.1.2 and 2.3.1). Alternatively, a single spin asymmetry could be attributed to a correlation between the parent hadron's spin and the transverse momentum of the initial-state parton. This correlation implies there exists a bias in the transverse motion of partons inside its parent hadron. This correlation is called the Sivers Effect [18].

The goal of this analysis is to help determine the relative contribution of sources of a measured single spin asymmetry such as Collins coupled with transversity or the Sivers effect (in the TMD framework). It is important to note that difficulty in measurement primarily arises due to the composite and complex nature of the proton coupled with the ability to only measure final-state particles that exist after fragmentation.

2.3 Fragmentation Functions

In our context, a fragmentation function is a description of the number-density of a produced particle flavor during the QCD-dressing of a parton due to color confinement as it attempts to exit a collision system. Essentially, fragmentation functions describe the hadronization of quarks and gluons. While the number-density alone is an interesting quantity, the fragmentation function can also describe the number density as a function of z, which is the longitudinal momentum fraction of the produced hadron relative to the fragmenting parton. Additionally, a characteristic width (usually a positive-definite Gaussian with a mean of zero) of the transverse momentum ($p_\perp$) distribution of the produced hadrons with respect to the parton momentum vector direction can be defined. For our interests, the quark fragmentation functions are of particular importance. Equation 2.3 is the usual formalism to describe a fragmentation function of this type.

$$D_q^h(z,p_\perp) = D_q^h(z)\frac{e^{-p_\perp{}^2/<p_\perp{}^2>}}{\pi < p_\perp{}^2 >} \tag{2.3}$$

Where:

- q = flavor of the fragmenting parton
- h = species of the produced hadron
- $z = \frac{\overrightarrow{p}_h \cdot \hat{q}}{|\overrightarrow{q}|}$ = longitudinal momentum fraction of the produced hadron with respect to the fragmenting parton
- $D_q^h(z) = \int d^2\overrightarrow{p}_\perp D_q^h(z,p_\perp)$ = number density for a quark “q” fragmenting into a hadron “h” with a momentum fraction “z”.
- $< p_\perp{}^2 >= 0.25 GeV^2$ is a fixed value extracted from SIDIS data and can be found in Reference [19].
- $D_q^h(z,p_\perp)$ = number density for a quark “q” fragmenting into a hadron “h” with a momentum fraction “z” at a momentum transverse to the quark axis of $p_\perp$.

The $D_q^h(z)$ term is extracted from data and a comparison of the extraction to a data set can be seen in Figure 2.6 for the DSS [20] (Daniel de Florian, Rodolfo Sassot, and Marco Stratmann) extraction. Rigorous comparison between the DSS extractions and ten different experiments spanning differing and overlapping phase spaces can be seen in Reference [20].

2.3.1 Collins Function

The Collins Function is a spatial-modulation applied to the fragmentation function. We first define a few terms:

- $\overrightarrow{p}_q$ = quark momentum vector
- $\overrightarrow{P}_q$ = quark transverse polarization vector
- $\overrightarrow{p}_h$ = hadron momentum, where $\overrightarrow{p}_h = z\overrightarrow{p}_q + \overrightarrow{p}_{hT}$ where $\overrightarrow{p}_{hT}$ is relative to the quark momentum vector

- $D_q^h(z, p_T)$ = as before, our z and p_T dependent unpolarized fragmentation function
- $\Delta^N D_{q^\uparrow}^h(z, p_T)$ = Collins fragmentation function (the Δ^N term is just nomenclature). The $q^\uparrow$ term represents a transversely polarized quark.
- $\frac{\overrightarrow{P}_q \cdot (\overrightarrow{p}_q \times \overrightarrow{p}_{hT})}{|\overrightarrow{p}_q \times \overrightarrow{p}_{hT}|}$, all possible spatial modulations which allow for the conversation of momentum. See Equation 2.4.

The spatial modulation term looks complex, but due to our transverse quark spin requirement it reduces nicely:

$$\begin{aligned}
\overrightarrow{p}_q \cdot \overrightarrow{P}_q &= 0 \\
\overrightarrow{p}_q \cdot \overrightarrow{p}_{hT} &= 0 \\
A = \|\mathbf{a} \times \mathbf{b}\| &= \|\mathbf{a}\| \, \|\mathbf{b}\| \sin\theta. \\
\mathbf{a} \cdot \mathbf{b} &= \|\mathbf{a}\| \, \|\mathbf{b}\| \cos\theta, \\
\frac{\overrightarrow{P}_q \cdot (\overrightarrow{p}_q \times \overrightarrow{p}_{hT})}{|\overrightarrow{p}_q \times \overrightarrow{p}_{hT}|} &= P_q \sin(\Phi_C)
\end{aligned} \tag{2.4}$$

Where Φ_C is the Collins angle [22] measured from the quark transverse polarization to the hadron momentum in the transverse plane (relative to the quark). Equation 2.5 shows the formalism adopted for the modulation.

$$D_q^h(\overrightarrow{p}_q, \overrightarrow{P}_q; z, \overrightarrow{p}_T) = D_q^h + \frac{1}{2}\Delta^N D_q^h(z, p_T^\uparrow) P_q \sin(\Phi_C) \tag{2.5}$$

Since we are interested in measuring an asymmetry, it is useful to know the difference between "up" and "down" polarizations in which the $D_q^h(z, p_T)$ term vanishes:

$$D_q^h(\overrightarrow{p}_q, \overrightarrow{P}_q; z, \overrightarrow{p}_T) - D_q^h(\overrightarrow{p}_q, -\overrightarrow{P}_q; z, \overrightarrow{p}_T) = \Delta^N D_q^h(z, p_T) P_q \sin(\Phi_C) \tag{2.6}$$

This implies that there exists an A_N (analyzing power, asymmetry) associated with the fragmentation. Specifically Equation 4 from [22]:

$$A_q^h(\overrightarrow{p}_q, \overrightarrow{P}_q; z, \overrightarrow{p}_{hT}) = A_q^h(z, p_T) \cdot P_q \sin(\Phi_C) \tag{2.7}$$

This asymmetry would represent a contributing factor to a single spin asymmetry in proton-proton collisions[1] [24] as seen in Section 2.2. Simultaneous extractions of the Collins function and transversity were performed by the Anselmino group in a global analysis of available data. The full detail of the kinematics and data-sets involved can be seen in Reference [25]. New data is continuously generated and added to the global analysis, updated extraction results without full explanation (but with the parameterization functions shown) can be found in References [15] and [26].

In reality, there could exist a different Collins function for each quark flavor and fragmentation hadron combination ($\Delta^N D_{d^\uparrow}^{\pi^+}(z)$,$\Delta^N D_{\bar{u}^\uparrow}^{\pi^-}(z)$, etc.), but currently that level of detail is not possible given the available data. However, the Anselmino group defines two sets of Collins functions, one for "favored" and one for "disfavored" fragmentation. A favored fragmentation is one in which the fragmenting quark is producing a hadron which contains a (valence) quark of that flavor. For example, an up-quark fragmenting into a π^+ is a favored fragmentation since the π^+ has a constituent up-quark. An example of a disfavored fragmentation would be a down-quark fragmenting into a π^+. Figure 2.7 shows the latest Collins function extraction from the Anselmino group for both favored and disfavored fragmentation. Above $x \approx 0.25$ is extrapolation of the functional form, no data exists in this region.

A main goal of this analysis is to garner some control over the relative contribution of the Collins function relative to the Sivers and higher-twist contributions (which are equivalent to Sivers in equal energy regimes) to a single spin asymmetry in proton-proton collisions as seen in Figure 2.5.

---

[1] It should be noted that previous studies on the possible contribution of the Collins effect to a single spin asymmetry seen in proton-proton collisions were erroneous (Erroneous, not cited: Phys. Rev. D 71, 014002 – Published 3 January 2005) and ruled out the possibility of a Collins contribution. The error was corrected and new upper-limits on the Collins contribution were calculated [23] which allow for a sizable Collins contribution to a single spin asymmetry.

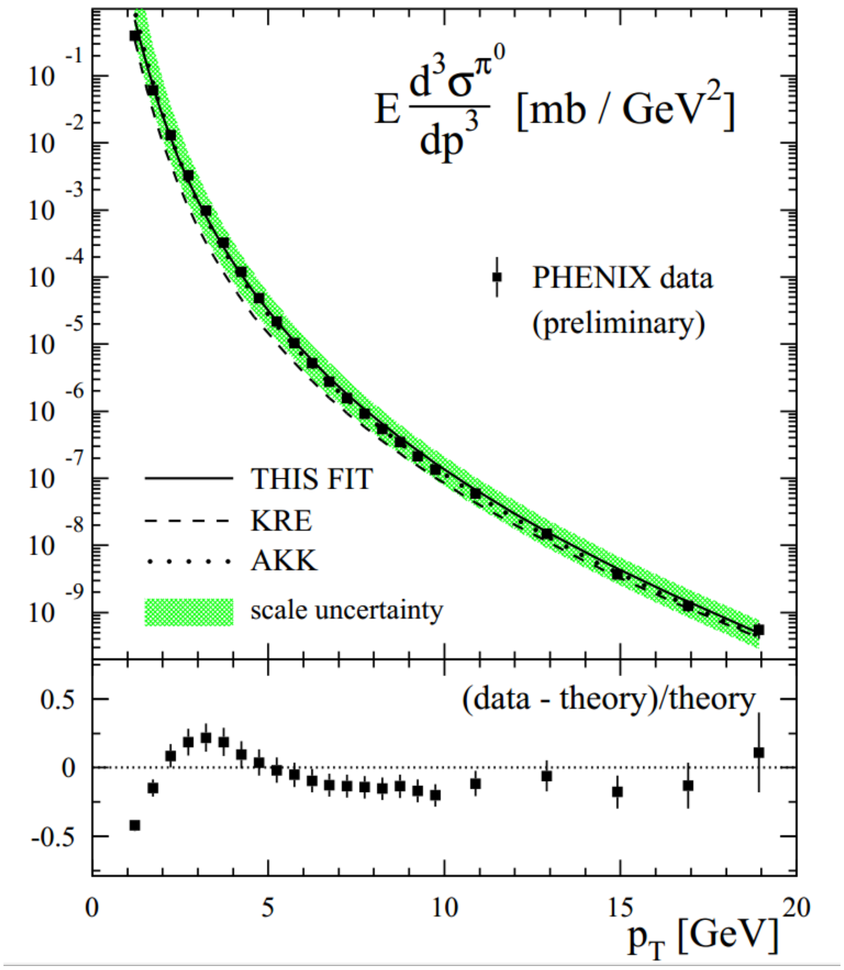

Figure 2.6 The DSS group [20] theoretical NLO calculation which determines the $D_q^h(z) = D_q^{\pi^0}(z)$ term at mid-rapidities ($|\eta| \leq 0.35$) as measured by the PHENIX experiment [21]. The Y-axis is proportional to the differential cross section ($E\frac{d^3\sigma^{\pi^0}}{dp^3}$). "THIS FIT" is the DSS theoretical fit; the KRE and AKK are other theoretical fits. A good agreement between theory and data can be seen.

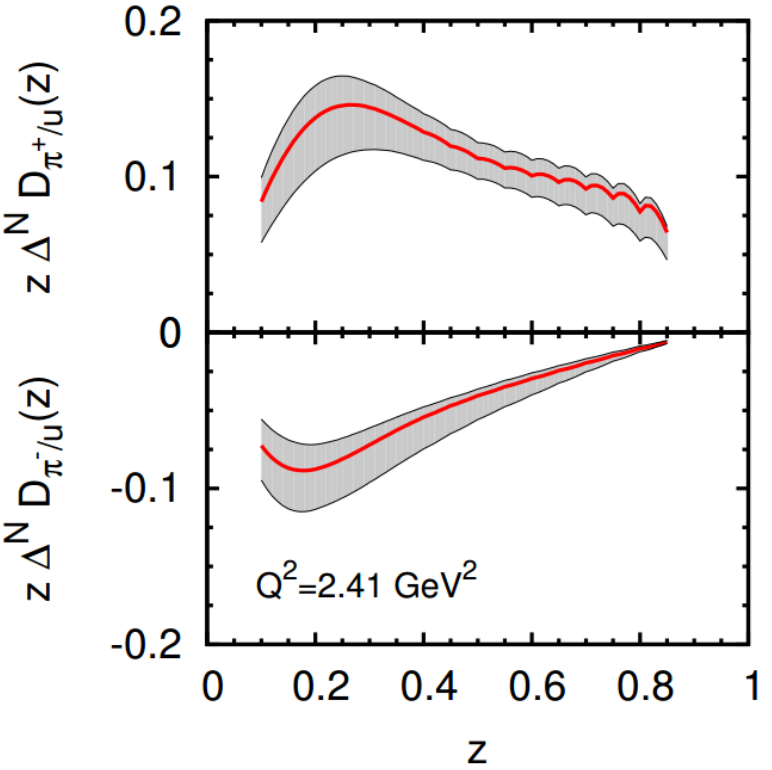

Figure 2.7 Anselmino group Collins functions extractions ($z\Delta^N D^h_{q^\uparrow}(z)$) [15]. The red line represents the Collins function value with their associated uncertainty bands. The top and bottom plots correspond to the favored and disfavored Collins functions respectively.

CHAPTER 3. EXPERIMENTAL SETUP

3.1 The Relativistic Heavy Ion Collider

The measurement performed here relies on the fact that we can probe polarized proton-proton collisions at a center-of-momentum such that our Bjorken-x value lies in the valence region where transversity is large. The only place on earth that can meet these requirements is the Relativistic Heavy Ion Collider (RHIC) at Brookhaven National Laboratory (BNL). Specifically, RHIC is used in the configuration such that it is colliding transversely polarized protons at a $\sqrt{s}$ of 200 GeV with an average polarization of roughly 60%. A schematic view of the facility at BNL can be seen in Figure 3.1. Of particular note are the PHENIX and STAR experiments; sister experiments at two different RHIC interaction points (IPs) where the proton beams collide.

3.2 Polarization and Acceleration

To obtain our polarized proton beams we first start at the Optically Pumped Polarized Ion Source (OPPIS)[28] the location of which can be see in Figure 3.1. For each beam bunch the OPPIS produces 11×10^{11} negatively charged Hydrogen atoms with a net polarization of 85%. To achieve this result the OPPIS is fed from a new Fast Atomic Hydrogen Source [29] which provides an ionized atomic hydrogen beam from a helium gas ionizer cell [30]. The unpolarized proton beam is sent through excited (optically pumped) Rubidium gas in a four Tesla magnetic field. The unpolarized protons pick up longitudinally spin-polarized electrons from the Rb vapor cell. The neutral, polarized hydrogen atoms are sent through a region with rapid magnetic field reversal that causes hyperfine splitting of the electron energy level due to the polarization of the electron and eventually transfer of the polarization to the nucleus (called the Sona-transition).

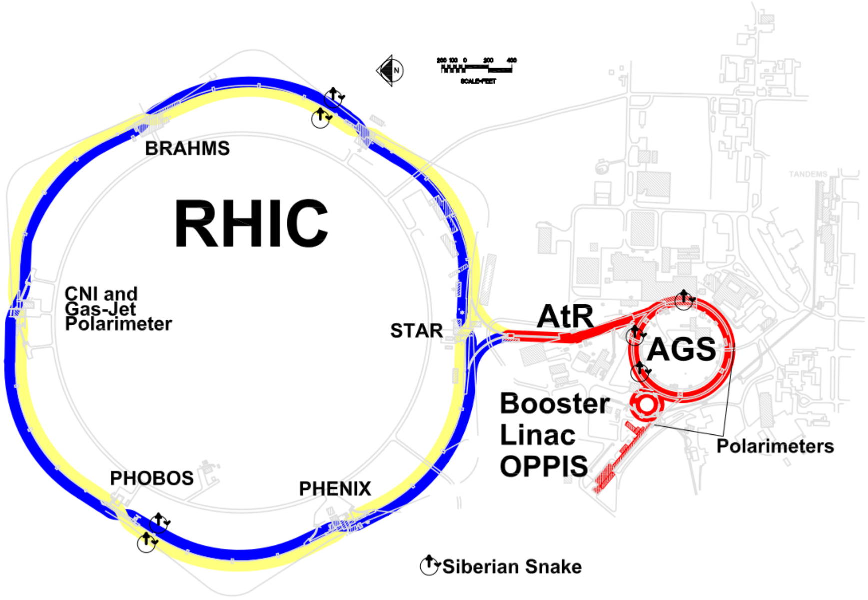

Figure 3.1 An aerial view of the Relativistic Heavy Ion Collider complex with superimposed graphics showing acceleration and detection facilities [27].

The longitudinally nuclear-polarized hydrogen is then given an extra electron via a sodium vapor cell making it negatively charged and allowing further acceleration. A flow chart of this process can be seen in Figure 3.2

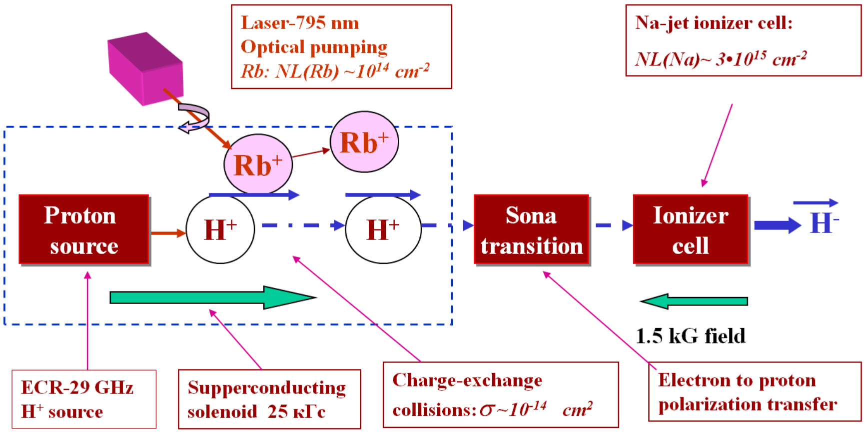

Figure 3.2 Spin-Transfer Polarization in Proton-Rb Collisions[31]

There are several points of both losses of ions/protons and polarization during the following stages. Once the longitudinally polarized-H^- ions leave the OPPIS they are accelerated through the Radio Frequency Cavity (RFQ) to 750 KeV of 11×10^{11} protons with 85% transverse polarization; the first solenoidal spin-rotator is used to change the polarization from longitudinal to transverse in the RFQ. The LINAC then accelerates the ions to 200 MeV, strips their extra electrons, and injects bunch sizes of $6.0 - 6.5 \times 10^{11}$ of 85% polarized protons into the Booster synchrotron. The Booster provides acceleration to 2.3 GeV and injects $2.2 - 2.4 \times 10^{11}$ protons at 80% polarization into the Alternating Gradient Synchrotron (AGS). The AGS then accelerates the protons to 24.3 GeV and injects $2.0 - 2.2 \times 10^{11}$ protons at 65-70% polarization into the AGS-to-RHIC (AtR) transfer line to enter the RHIC ring so the bunch is circling in either the clockwise ("Blue beam") or anti-clockwise ("Yellow beam") directions (shown in Figure 3.1). Once the bunch is in the RHIC ring it is accelerated to 100 GeV/c and has a average intensity of 1.8×10^{11} protons per bunch at 58% polarization([30],[32]).

3.2.1 Siberian Snakes

As seen in the last section, much of the initial 85% polarization is lost in the AGS and RHIC acceleration stages. The particles in these stages are in a closed orbit such that the particle trajectory remains constant from one orbital revolution to the next. A main source of polarization loss in a circular accelerator is betatron oscillation coupled with Thomas precession.

The Thomas-BMT equation (Equation 3.1) describes the behavior of a particle's spin in a static magnetic field:

$$\frac{d\vec{S}}{dt} = \frac{q}{m\gamma}\vec{S} \times [\vec{B} + G(\gamma\vec{B}_\perp + \vec{B}_\parallel)] \tag{3.1}$$

Where $\vec{B}_\parallel = \hat{v} \cdot \vec{B}\hat{v}$ and $\vec{B}_\perp = \vec{B} - \vec{B}_\parallel = (\hat{v} \times \vec{B}) \times \hat{v}$ are the longitudinal and transverse components of the magnetic field and $\vec{v}$ is the particle velocity. G is the anomalous magnetic moment of the particle, q is its charge, m is its mass, and γ is the Lorentz factor associated with the particle's relativistic motion.

At large values of γ we can ignore the $\vec{B}_\parallel$ term giving us Equations 3.2 and 3.3[33] where $G\gamma$ is the precession frequency (spin tune)[34]. The spin precession frequency is constantly changing as the particle is accelerated in the AGS and RHIC rings. If the spin precession frequency matches the frequency of either an imperfection resonance or intrinsic resonance in the accelerator a spin depolarizing effect will occur. An imperfection resonance is simply an imperfection in the magnetic field seen by the particle that occurs at a fixed interval. An intrinsic resonance is due to vertical betatron oscillations which occur when particle trajectories deviate from a flat circular orbit and the magnetic field periodically provides a restoring force (weak focusing) to correct the deviation as seen can be seen in Figure 3.3.

$$\frac{d\vec{S}}{dt} = \frac{q}{m\gamma}\vec{S} \times [\vec{B} + G\gamma\vec{B}_{\perp}] \tag{3.2}$$

$$(\frac{\Delta\phi}{2\pi})_{perloop} = \gamma(g/2-1) = \gamma G \tag{3.3}$$

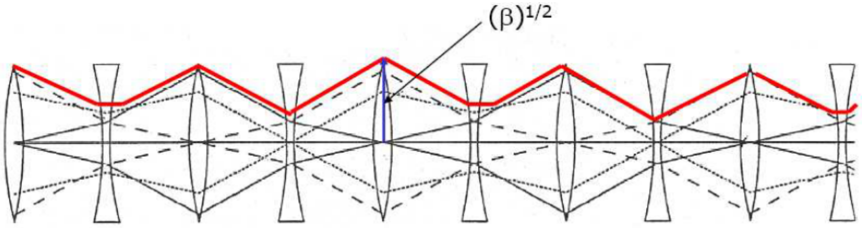

Figure 3.3 Betatron oscillation diagram. Red is the particle trajectory.[35]

To combat these resonances the transverse polarization direction of the beam is rotated at specific points along the AGS and RHIC rings using “Siberian Snakes”; the positions of which can be seen in Figure 3.1. The AGS ring contains one partial-Snake which rotates the polarization direction by 9° and the RHIC ring contains two full-Snakes which rotate the polarization direction by 180° each. The goal of the Siberian Snakes is to counter-balance the spin depolarization resonances by changing the polarization direction each time the beam encounters said resonance; this way, the depolarization is fighting against itself with each revolution of the beam. A schematic of a 180° spin flip by a full Siberian Snake can be seen in Figure 3.4.

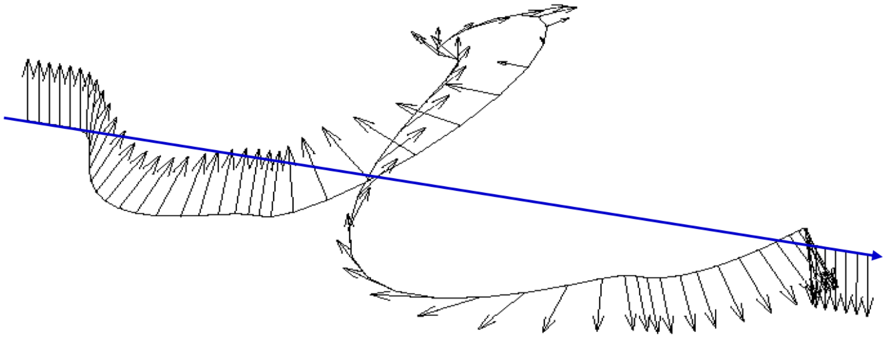

Figure 3.4 Schematic of beam polarization changing from “up” to “down” due to a full Siberian Snake.[35]

3.2.2 Polarimetry

To learn how to maintain and increase beam polarization one must measure it. There are two main polarimeters in the RHIC ring and one “local” polarimeter in each of the STAR and PHENIX experiments. The two main RHIC polarimeters are the CNI and HJet which can be seen in Figure 3.1 and will be discussed in the next sections. The “local” polarimeter is located at the PHENIX interaction point and will also be discussed in the next sections.

3.2.2.1 CNI Polarimeters

For high-statistics “fast” polarization measurements RHIC utilizes the Coulomb Nuclear Inferference (CNI) polarimeters[36] (also called the Proton-Carbon (PC) polarimeters). There are two CNI polarimeters in each ring that allow for the measurements of both vertical and horizontal beam polarization profiles. Each polarimeter utilizes horizontal or vertical Carbon targets and six Silicon strip detectors for measuring recoil Carbon ions. The detection system performs a measurement of the raw azimuthal asymmetry (ϵ_N) relative to the beam’s polarization direction (nominally vertical). These polarimeters are able to extract an asymmetry quickly (multiple times during a single fill) but are only able to make relative asymmetry measurements rather than an absolute asymmetry measurement, i.e. the CNI polarimeters are only able to measure changes in polarization rather than absolute polarization as seen in Equation 3.4.

$$A_N(physics, unknown) = \frac{\epsilon_N(measured)}{P_{beam}(wanted, unknown)} \tag{3.4}$$

3.2.2.2 Hydrogen-Jet Polarimeter

To obtain an absolute polarization measurement the high-statistics CNI relative-polarization measurements are combined with low-statistics Hydrogen-Jet polarimetery (HJet) measurements ([36], [37]). The HJet polarimeter injects a gas of ionized and polarized Hydrogen into the beam region where interactions take place. Polarized Hydrogen scatters off the beam and is detected by Silicon strip detectors (Figure 3.5) similar to how the CNI measures interactions. Because both the HJet and the beam are polarized one is able to extract the polarization of the beam via a spatial azimuthal asymmetry measurement given that the HJet polarization was already measured.

$$A_N(physics) = \frac{\epsilon_{N,target}(measured)}{P_{target}(known)} = \frac{\epsilon_{N,beam}(measured)}{P_{beam}(wanted, unknown)} \tag{3.5}$$

Equation 3.5 shows the relationship between target and beam polarizations and raw asymmetries; $\epsilon_{N,target}$ uses the target spin sign, $\epsilon_{N,beam}$ uses the beam spin sign[38] and their final physics asymmetry must be equal as they are undergoing elastic scattering. The slow collection of statistics by the HJet polarimeter means that the data from an entire Run-year is utilized to obtain the absolute polarization in conjunction with the CNI's fill-by-fill (and semi-hourly) results.

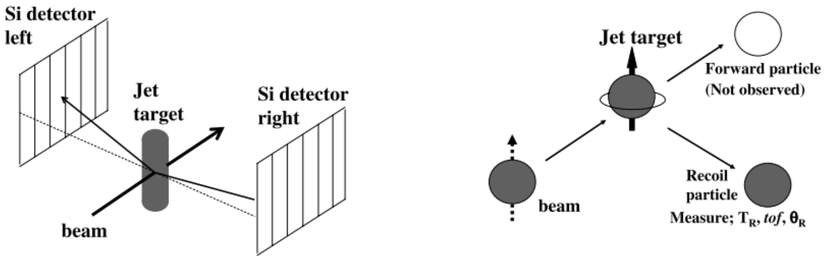

Figure 3.5 Left: Setup, Left: Elastic scattering process[37]

3.2.2.3 Local Polarimeters

As a cross-check the PHENIX experiment utilizes two Zero Degree Calorimeter (ZDC) detectors at positions that can be seen in Figure 3.8 and Figure 3.6. The ZDCs are hadronic calorimeters with a total interaction length of $5.1 \times \lambda_I$ that are able to use the large Neutron asymmetry [39] seen in proton-proton collisions as a measurement of the beam polarization magnitude and direction at the PHENIX interaction point for each beam. The ZDCs are each positioned behind the RHIC crossing-magnets (DX magnets) so that the vast majority of particles that can reach the ZDC are neutral; charged particles are swept away by the magnetic field in front of the ZDC [40]. I was part of the team that did the Run-12 ZDC calibrations and local polarimetery, the primary goal of which was to reduce the unwanted longitudinal or transverse components of the beam polarization as needed by the experiment as well as monitor the polarization throughout the year for any deviations.

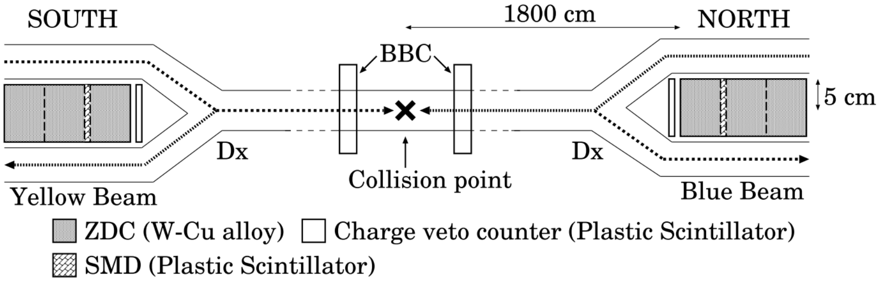

Figure 3.6 A plan view of the experimental setup at PHENIX, not to scale. Shown are the principle components for the leading neutron physics.[41]

3.2.3 Spin Pattern

Each RHIC beam bunch contains a total of 120 bunches (variable) each containing roughly 1.8×10^{11} protons per bunch. The polarization of each bunch can be pointed in any direction transverse to the motion of the bunch while in the ring. Nominally each bunch is either “up” or “down”, which is when the polarization vector of the bunches are literally pointing either toward the sky or toward the ground. Since both the Yellow and Blue beams are polarized, there are a total of four combinations of polarized collisions for our collision system: $p^{\uparrow} + p^{\uparrow}$, $p^{\downarrow} + p^{\uparrow}$, $p^{\uparrow} + p^{\downarrow}$, and $p^{\downarrow} + p^{\downarrow}$. A naive way to get such a combination is to orient the beams as shown in Figure 3.7, though the actual spin pattern changes from fill to fill in an effort to reduce possible systematic errors associated with certain bunches being specific polarizations throughout a Run, or the order of polarizations being collided.

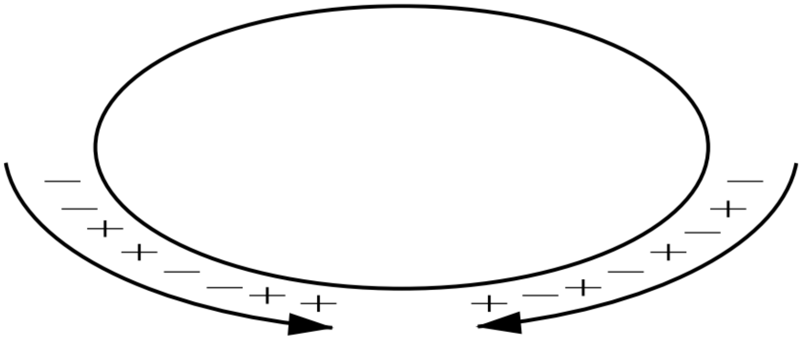

Figure 3.7 The pattern of the polarization signs of the bunches in the two counter-rotating beams in RHIC. It is typically desirable to collide equal numbers of $(+\,+, +\,-, -\,+, -\,-)$ bunches at each experiment, where $(+\,-)$ represents a bunch in one beam with polarization up colliding with a bunch in the other beam with polarization down in transverse pp mode.[41]

3.3 The PHENIX Detector

The PHENIX (Pioneering High Energy Nuclear Interaction eXperiment) detector is actually a conglomeration of over ten different sub-detectors which work in tandem to provide a complete picture of the final state of a collision at the interaction point of the experiment [42]. A set of schematics of the full detector system in the configuration that existed in 2012 can be seen in Figure 3.8. Of particular interest to this measurement are the Beam-Beam Counters, Central Arm detectors (East and West arms), and the Muon Piston Calorimeter detectors.

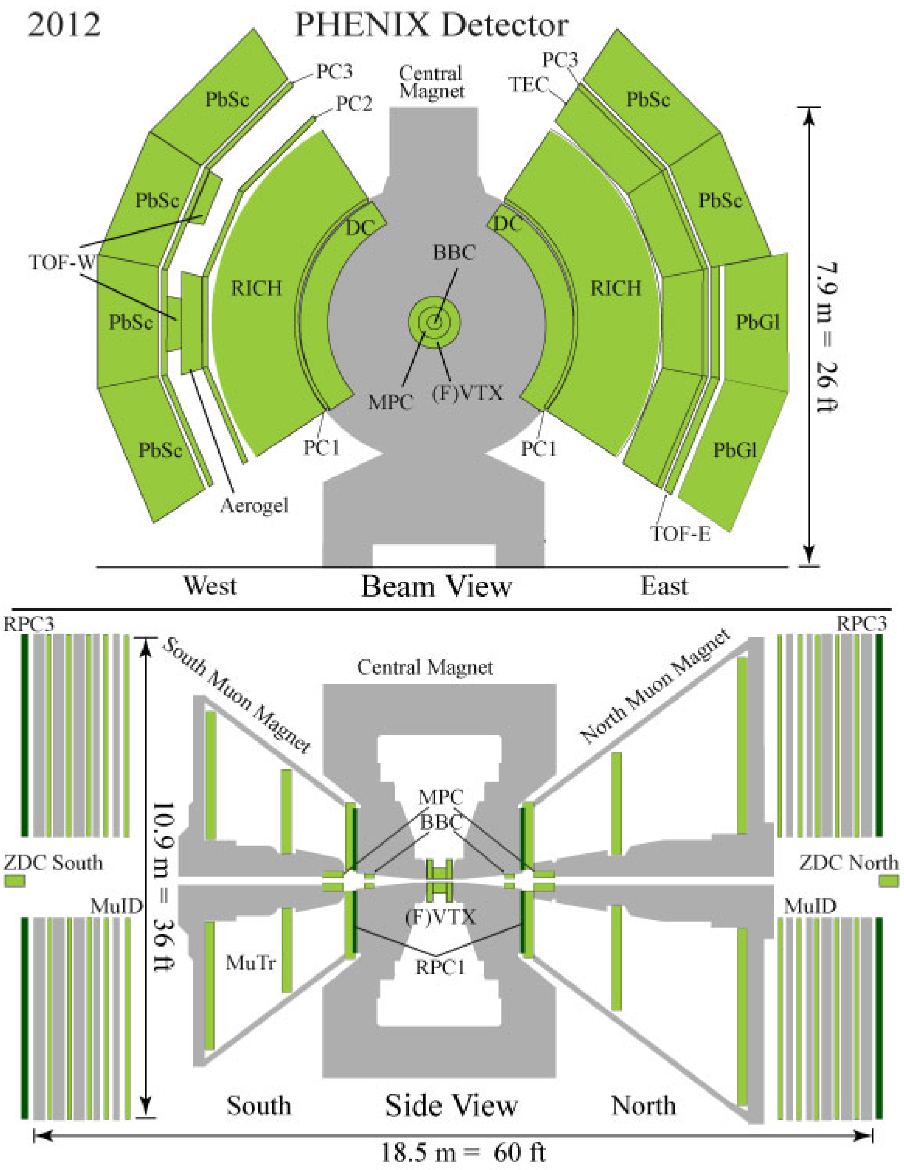

Figure 3.8 Schematics of the PHENIX detector configuration during the 2012 data taking period.

3.3.1 Beam-Beam Counters

The first step in determining whether or not an inelastic interaction occurred usually begins with the Beam-Beam Counters (BBCs) [43, 44]. They have been used in dozens of publications from the PHENIX collaboration. As can be see in Figure 3.8, the BBCs reside at large forward and backward rapidity circling the beam pipe entirely. The North and South BBCs work together to determine where (along the beam axis) and when an interaction of interest has happened. In this analysis I require a "minimum bias" event such that the interaction occurs within +/- 30cm of the middle of the PHENIX detector (z=0 point). This is crucially important as the Central Arm detector configuration is best utilized for collisions in this region. Along with determining the z-vertex of the interaction, the BBC detectors determine the time at which the interaction occurs (t=0 for each event). This is important so that other detector systems use the same start-time for each individual event and the detectors are kept synchronized.

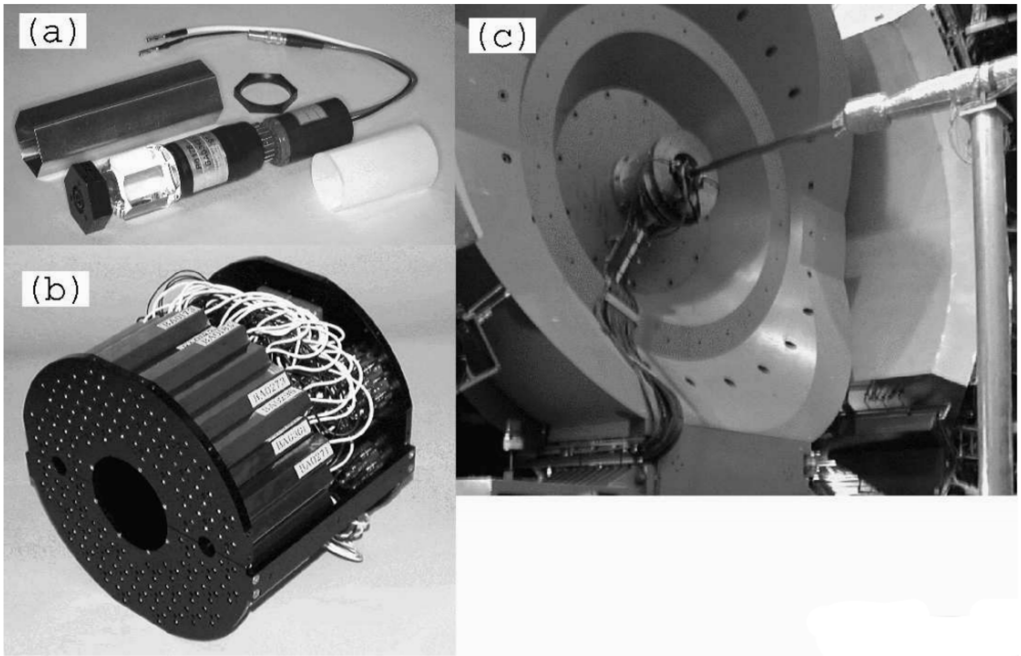

Figure 3.9 (a) Single PMT tube and quartz radiator. (b) One arm of the BBC detector (c) Location of one of the BBC detectors in the PHENIX setup. The BBC is encircling the beam pipe in this image.

The BBC detectors themselves are an array of quartz radiators coupled with photomultiplier tubes which can be seen in Figure 3.9. The BBCs lie between a pseudorapidity of 3.1 and 3.9 in both the backward in forward direction at a distance of 144cm from the center of the PHENIX detector as seen in Figure 3.8. An average of the detected signals' times in both the North and

South detectors are used to determine both the z-vertex and time (t=0) of the interaction.

3.3.2 Electromagnetic Calorimeter

The primary use of the PHENIX Electomagnetic Calorimeters [45] is for the measurement of electromagnetic energy deposition and time-of-flight measurement (relative to the BBC's t=0 timing point). The electromagnetic calorimeters are divided into eight sectors which span in total 90° (East arm) + 90° (West arm) in azimuth and from -0.35 to 0.35 in pseudorapidity. Four sectors of lead-scintillator calorimeters reside in the West arm; two sectors of lead-scintillator and two sectors of lead-glass calorimeters reside in the East arm. In total, the PHENIX EMCals are made of 24,768 detector channels which give precise spatial positioning information of detected electromagnetic clusters. It is important to analyze the Pb-Glass and Pb-Sc calorimeters independently since they behave quite differently. In general, an EMCal works by introducing a photon or charged particle to "radiation lengths" (electromagnetic mean-free-path) of material which causes Bremsstrahlung ($e \rightarrow e^{-}\gamma$) and pair-production ($\gamma \rightarrow e^{+}e^{-}$) (electromagnetic shower). The relative contribution of these processes to the total cluster are energy dependent. Light from charged particle scintillation in the medium is collected and funneled to a device such as a semiconductor Avalanche Photo-Diode (APD) or Photo-Multiplier Tube (PMT) and the signals are read out by electronics.

3.3.3 Lead-Glass Calorimeters

The lead-glass calorimeter is a homogeneous calorimeter comprised of 9,216 towers of a transparent material which both produces scintillation light from charged particles traversing the medium and funnels it to a photo-multiplier. The towers are grouped into super modules in sets of 24 towers and share common electronics but maintain independent read-outs for each channel. Each tower has a cross-sectional area of 4cm × 4cm and a depth of 40cm. The lead-glass type used has a Moliere radius of 3.68cm, which means that a single electromagnetic shower spans several towers that must be summed together into a "cluster". The Pb-Glass material has an interaction length (hadronic mean-free-path) of 38cm, so only minimal neutral Hadron energy is measured; this is beneficial to our measurement as we do not want neutral hadron contamination. The total energy resolution for the lead-glass type towers is $\frac{6\%}{\sqrt{E(GeV)}}$.

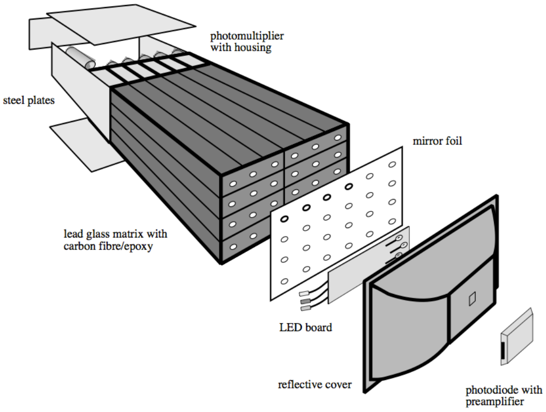

Figure 3.10 Exploded view of a lead-glass detector super module.

3.3.4 Lead-Scintillator Calorimeters

The lead-scintillator calorimeter is a sampling calorimeter comprised of 15,552 towers, each consisting of alternating lead and scintillator material. The lead material is the catalyst for electromagnetic showers while the scintillation fibers that run the entire depth of the tower collect and funnel the light to PMTs. Four towers are combined into a single module (as seen in Figure 3.11), but each tower is then read out individually by electronics. With an active depth for each tower of 37.5cm this equates to only 85% of an interaction length of material, also leading to minimal neutral Hadron energy deposited. The total energy resolution for the lead-scintillator type towers is $\frac{8.1\%}{\sqrt{E(GeV)}} \bigoplus 2.1\%$.

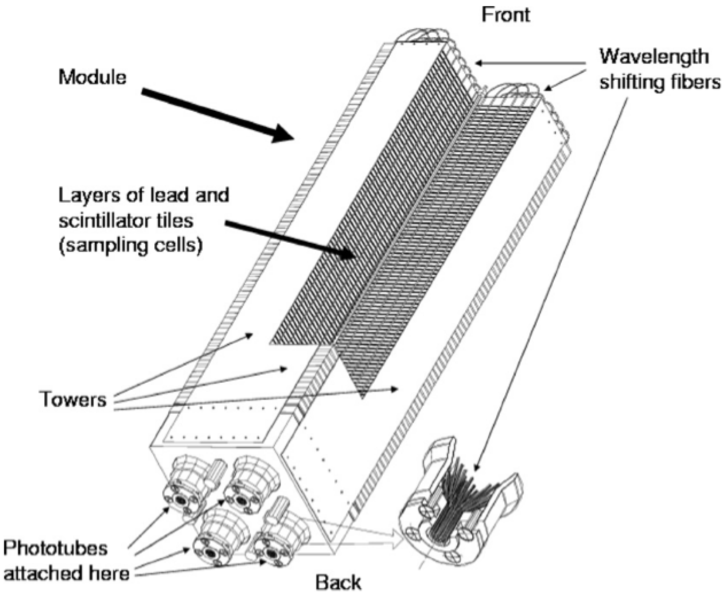

Figure 3.11 Interior view of a Pb-scintillator calorimeter module showing a stack of scintillator and lead plates, wavelength shifting fiber readout and leaky fiber inserted in the central hole.

3.3.5 Drift Chamber

The PHENIX Drift Chamber (DC)[46] detectors measure charged particle tracks in the PHENIX central arms. Each Drift Chamber covers the full area of the East and West PHENIX arms. The face of the Drift Chamber starts at 2.0 meters from the beam line, this is far enough from the interaction region to only experience a minimal magnetic field. The charged tracks through the DC are thus straight lines which are measured in the r-ϕ direction to determine the bend caused by the magnetic field as the particle traversed the central region of the interaction region. The bend associated with the particle's traversal is used to determine the transverse momentum (p_T) of the particle. In general, a drift chamber is just a wire chamber that uses drift-time information (both “fast” and “slow”, negative and positive signals respectively) to localize where an interaction (ionization) in the scintillating or interacting gas occurs.

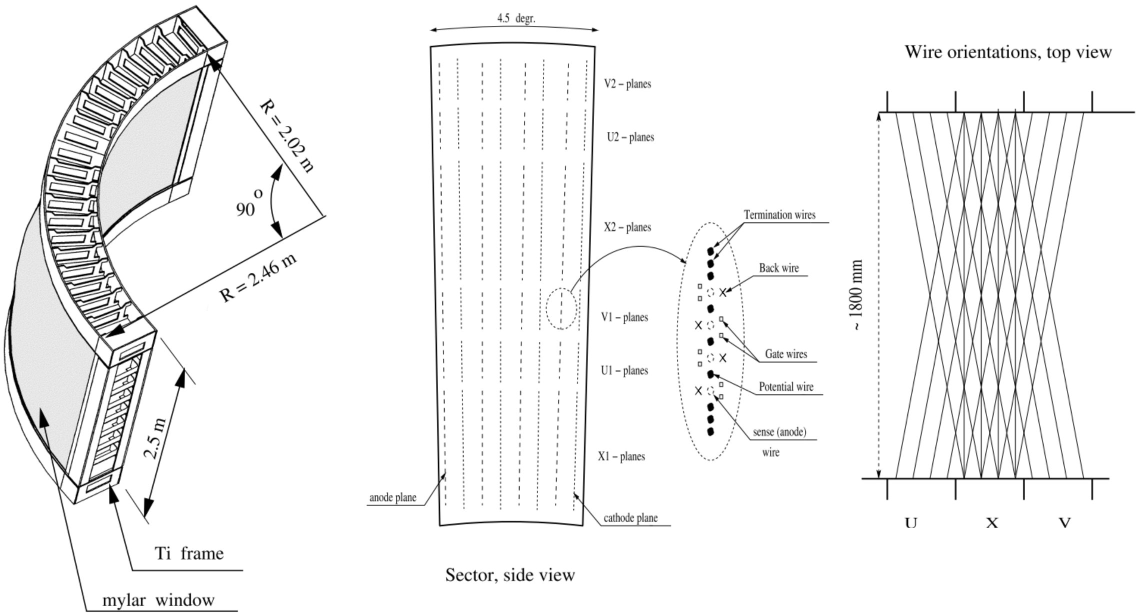

Figure 3.12 Left: Construction of DC frame, Middle: The layout of wire position within one sector and inside the anode plane (side view), Right: A schematic diagram of the stereo wire orientation (top view).

Each DC is comprised of a gas volume containing 50% Ar and 50% Ethane, though this specific balance is adjusted by DC experts to maintain constant high performance. The gas contains wires of differing orientation called the X, U, and V orientations as seen in Figure 3.12. The X orientation wires run parallel to the beam pipe and give the r-ϕ coordinate of the track; the U and V wires run at stereo angles of about 6 degrees relative to the X wires to give the an estimate of the z-coordinate of the track. In total the DC detectors contain a total of roughly 13,000 readout channels.

3.3.6 Pad Chambers

The PHENIX Pad Chamber (PC)[46] detectors (PC1, PC2, and PC3 as seen in Figure 3.8) are multi wire proportional chambers which specialize in the determination of the z-coordinate of a charged track traversing the PHENIX central arms. The PCs and DCs work in tandem to provide a full picture of the charged track reconstruction (but not necessarily particle identification) in PHENIX.

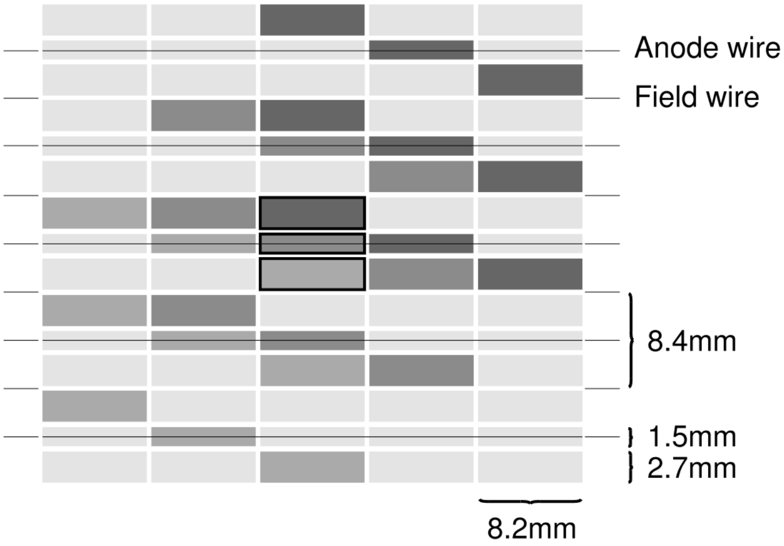

Figure 3.13 Cross-section of a pad chamber from the interaction region's vantage point. The anode and sense wires can be seen in front of the silicon pad detectors.

The PCs are composed of a gas volume containing a plane of anode wires that is bound by two cathode planes on either side. One of the cathode planes is composed of finely segmented pads (pad board), each of which contains three pixels while the other is a solid cathode as can be seen in Figure 3.13. For a valid hit to be found, an entire pad of three pixels must detect a charged particle avalanche on the pad board. Requiring three separate pixels to fire reduces the chance of electronics noise causing false signals. The pads are oriented such that they optimize the z-position resolution of a charged track. The z-position resolution of the PC1 detector is ±1.7mm and the PC3 detector has an equivalent angular resolution. Only the PC1 and PC3 are used in this analysis.

3.3.7 Ring-Imaging Cherenkov Detector

The Ring-Imaging Cherenkov detector[47] (RICH) provides electron-hadron separation between approximately 0.2 GeV/c and 4.0 GeV/c. The main purpose of this detector in this analysis is the rejection of hadrons.

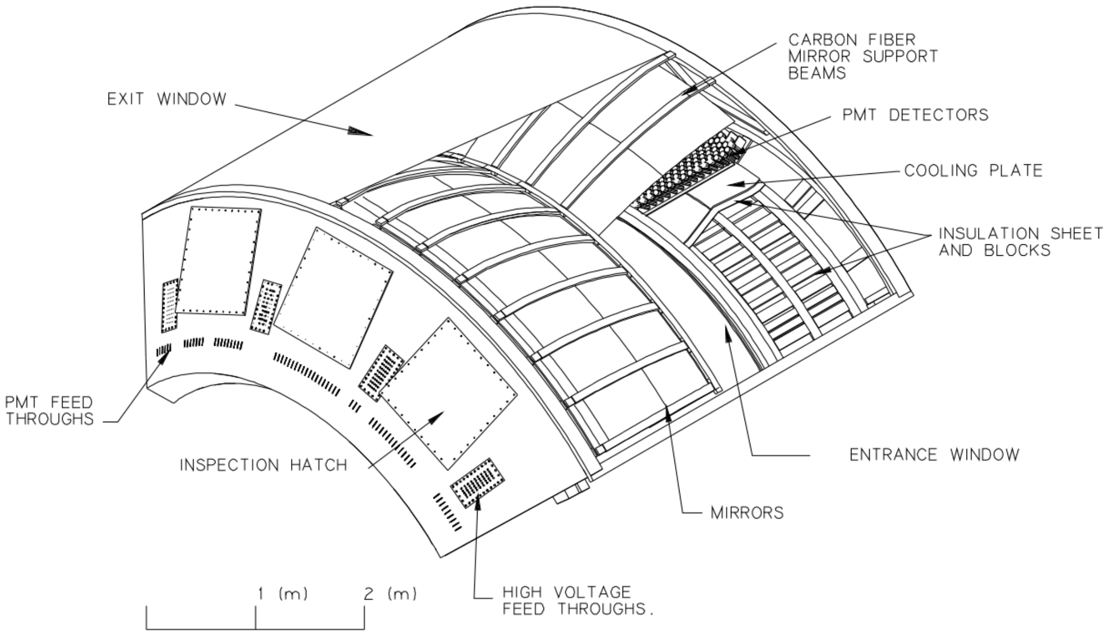

Figure 3.14 A cutaway view of one arm of the PHENIX RICH detector.

The RICH detectors in both PHENIX arms are identical. Each is filled with ethane or CO_2 gas and contains 48 composite mirror panels in two intersecting spherical surfaces which cover the back of the detector as seen in Figure 3.14. As an electron traverses the gas it produces scintillation light which is focused by the mirrors onto arrays of 1,280 photomultiplier tubes near the front of the detector. One can identify an electron using the RICH detector from the unique ring pattern that is formed on the PMT array from the spherical mirrors. To reduce the possibility of conversion electron creation the entire RICH detector was designed such that its thickness is only 2% of a radiation length when using ethane gas (though CO_2 gas was in use during Run-12).

3.3.8 Muon Piston Calorimeter

The Muon Piston Calorimeters (MPCs) are electromagnetic calorimeters sitting at forward rapidities and covering the full azimuth around the beam pipe as can be seen in Figure 3.8. Because the South MPC detector was undergoing an electronics upgrade during the Run-12 data-taking period this analysis only utilizes the North MPC detector. The North MPC detector sits between a pseudorapidity of 3.1 and 3.9 at a distance of 220cm from the interaction region. The North MPC is composed of 220 Lead-Tungstate ($PbWO_4$) crystals (towers) measuring 2.2cm × 2.2cm × 18cm. Each crystal is glued to an avalanche photo-diode (APD) which sends its output to read-out electronics.

The $PbWO_4$ crystals have a radiation length of $X_0 = 0.89cm$[48] and an interaction length of $\lambda_I = 22.4cm$[38], with a tower depth of 18cm this means that most of the energy collected is due to electromagnetic interactions. The Moliere radius of $PbWO_4$ is 2cm, meaning that an electromagnetic shower is roughly 90% contained within a single crystal if it starts at the center of said crystal. In reality, the shower extends and is summed over a 3x3 set of towers and made into a “cluster” similarly defined in the EMCal (Section 3.3.2). An extremely comprehensive resource for the MPC construction, design, and implementation can be found in reference: [38].

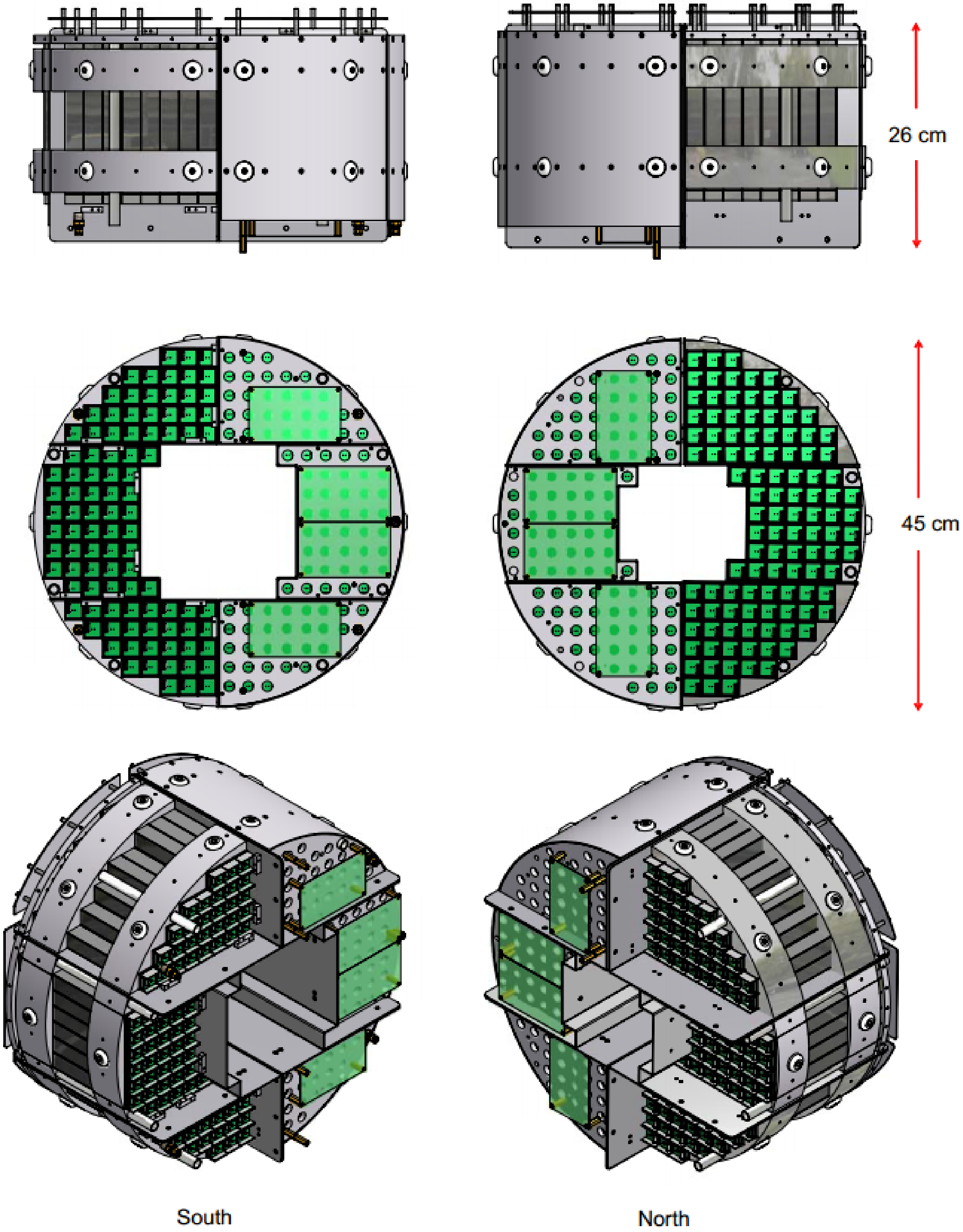

Figure 3.15 AutoCAD model rendering of the South (left) and North (right) MPC's. The bottom panel shows the the front side of the detector which faces the collision point[38].

CHAPTER 4. DATA QUALITY ASSURANCE AND CALIBRATIONS

To obtain usable experimental data for this analysis one must perform both detector calibrations and data quality assurance. I will first cover the calibrations I performed, all of which were made available to the PHENIX collaboration through the calibrations databases. A full GEANT3 [49] simulation using the PHENIX Integrated Simulation Application (PISA) of the detector systems was used for simulation studies. The results of both the real-detector QA and the simulated-detector QA will be shown where relevant.

4.1 Beam Offset Calibration

The PHENIX central arms are situated on a carriage system which allows each of the arms to be retracted for ease of access. After a carriage is moved there exists some error in returning it to the same location for data-taking (on the order of millimeters). To account for possible shifts in positions between the PHENIX East arm, West arm, and the beam-pipe due to carriage movement a calibration is performed to correct for any offset. A brief explanation of the calibration is shown here; a detailed explanation can be found in PHENIX Analysis Note 1120 [50]. The calibration is performed by turning the PHENIX central magnetic field(s) off and collecting data as usual. Since the magnets are off, charged particle tracks follow a straight line from the collision point (beam pipe) and the central arm tracking system as seen in Figure 4.2, i.e. the value of α should always be zero.

$$\alpha = \frac{dx}{R_{DC}} sin(\phi) + \frac{dy}{R_{DC}} cos(\phi) \tag{4.1}$$

Where:

- R_{DC} = radial distance from PHENIX coordinate (0,0,0) to the drift chamber detectors (nominally taken to be 220cm). The PHENIX coordinate system can be seen in Figure 4.1.
- ϕ = azimuthal angle defined by the PHENIX coordinate system
- α = angular separation between a straight line from (0,0,0) to the drift chamber hit position at R_{DC} for a charged track and the charged track's momentum vector at the drift chamber, this can be see in Figure 4.2
- dx = beam position displacement in the x direction in centimeters under the PHENIX coordinate system.
- dy = beam position displacement in the y direction in centimeters under the PHENIX coordinate system

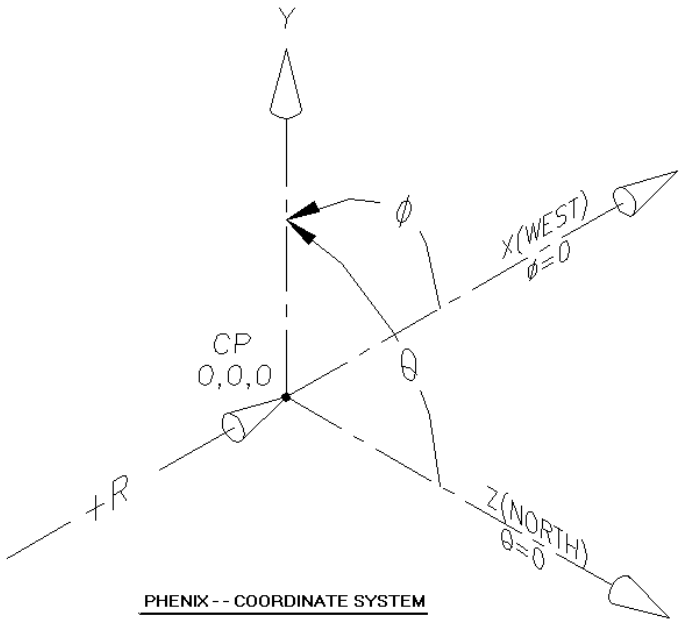

PHENIX local orgin (0,0,0) is referenced to the RHIC secondary survey control network

Beam is on th Z axis

Position of detector assemblies in the central arms is measured in r, phi, and Z (at least most of them)

Position of detector assemblies in the muon arms is measured in X, Y, and Z

6/13/95

Figure 4.1 PHENIX coordinate system

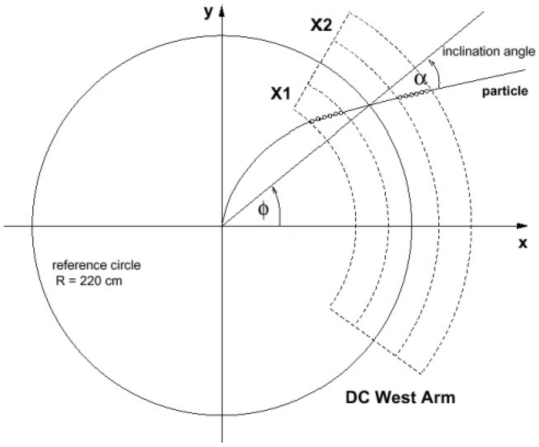

Figure 4.2 Definiton of α in PHENX

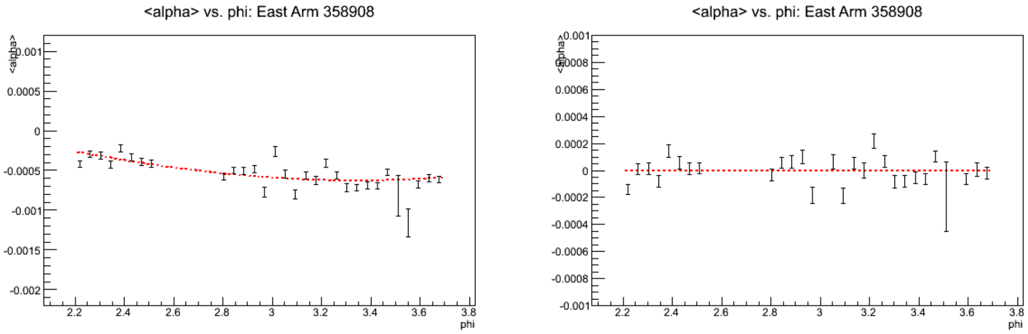

Figure 4.3 East Arm $< \alpha >$ plots; Left: before calibration, Right: after calibration. Red line the fit function from Equation 4.1.

Figure 4.3 shows data extracted from field-off data before and after the beam-offset calibration has been performed. Before the calibration is performed there are non-zero values of dx and dy in the fit function from Equation 4.1. After calibration one can see that the fit function is flat, meaning that dx and dy are both zero.

4.2 Global Momentum Scale Calibration

Changes in the magnetic field strength and gradients over time can result in the incorrect determination of the absolute momentum scale in the experiment. A brief explanation of the calibration is shown here; a detailed explanation can be found in PHENIX Analysis Note 1120 [50]. To correct for this change the global momentum scale calibration was performed. The global momentum scale calibration requires the beam offset calibration to be complete as described in the previous section. There are a few different ways to do the momentum scale calibration. I have chosen to use the Time of Flight (TOF) East detector to find protons' and antiprotons' masses and apply a correction relative to the Particle Data Group (PDG) value for the proton and anti-proton mass values of $0.938272\frac{GeV}{c^2}$ [51]. Figure 4.4 shows distributions of detected charged particle mass-squared values. To reduce backgrounds a minimum p_T cut of $1.0\frac{GeV}{c}$ is applied to the data during the calibration.

The global momentum scale correction is calculated as follows:

$$ProtonScaleFactor = \frac{ProtonMass_{measured}}{ProtonMass_{PDG}} \tag{4.2}$$

$$AntiProtonScaleFactor = \frac{AntiProtonMass_{measured}}{ProtonMass_{PDG}} \tag{4.3}$$

The final global momentum scale correction is the average of the proton and anti-proton scale factors. These should not, and did not, differ by more than a few hundredths of a percent. The measured proton (anti-proton) mass value was $0.9349\frac{GeV}{c^2}$ ($0.9332\frac{GeV}{c^2}$), meaning the momentum of all tracks is increased or decreased according to Equations 4.4 and 4.5 such that the average proton and anti-proton masses match the PDG value of $0.938272\frac{GeV}{c^2}$ as best possible. After the calibration was performed the scale factors were recalculated; their values were 0.999981 for the proton and 1.00087 for the anti-proton.

$$AvgScaleFactor = \frac{ProtonScaleFactor + AntiProtonScaleFactor}{2} \tag{4.4}$$

$$CorrectedMomentum = \frac{Momentum}{AvgScaleFactor} \tag{4.5}$$

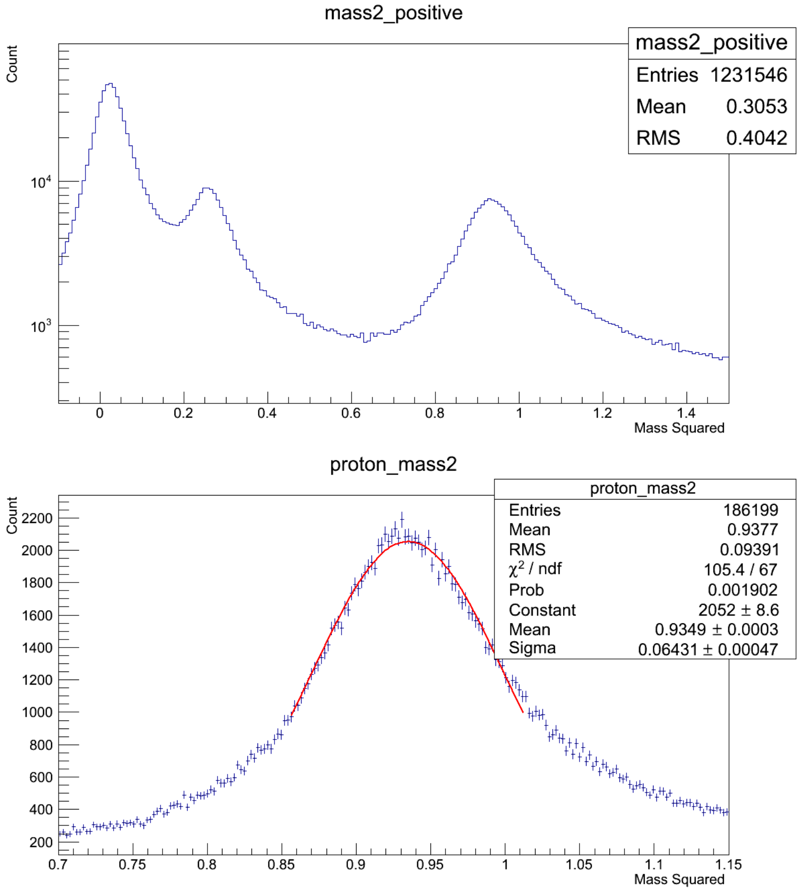

Figure 4.4 Positively charged tracks. Left: Full mass region, Right: Proton mass region with fit

4.3 EMCal and PC3 Track Matching Calibration

In this analysis we require that charged tracks in the PHENIX central arms are matched to a hit in the EMCal or PC3 hit. This requirement is used to reject false electromagnetic clusters in the EMCal as well as reduce the conversion electron and hadronic backgrounds; all of which have incorrect reconstructed momentum and energy as determined by the tracking system. A brief explanation of the calibration is shown here; a detailed explanation can be found in PHENIX Analysis Note 1117 [52]. Requiring a hit in either the PC3 or EMCal detectors also reduces the probability of fake track reconstruction due to combinatorics, e.g. three random hits or noise lining up and looking like a track. To enforce our PC3/EMCal hit requirement we measure the distance from the central arm track to the hit in PC3/EMCal in the z-direction (dz) and ϕ-direction (dϕ). A small value of the quantity $Distance = \sqrt{dz^2 + d\phi^2}$ means that the hit is likely associated with the track in question. To quantify a "small" *Distance* value we perform a calibration which "sigmalizes" (normalizes) the dz and dϕ values as follows:

$$sdz = \frac{dz - < dz >}{\sigma_{dz}} \tag{4.6}$$

$$sdphi = \frac{d\phi - < d\phi >}{\sigma_{d\phi}} \tag{4.7}$$

Where sdz and sdϕ are the "sigmalized" variables representing the standard deviation from the mean of the dz and dϕ distributions. The reasons for creating these sigmalized variables is so that they can be used for differing track charge values, p_T, ϕ, η, and PHENIX arms with ease; a single cut can be used for all the previously mentioned scenarios with known efficiency. Figure 4.5 shows dϕ and sdϕ as a function of track p_T. The usual track requirement used in PHENIX data analysis is that $|Distance| < 3.0$. The spread in the final calibrated sdϕ and sdz values are small enough such that they have no real impact at the $3 \cdot \sigma$ level.

4.4 EMCal Warnmap

Out of the 24,768 EMCal towers roughly 20% of them are not usable for my measurement. A "warnmap" was made which sets a classification for each tower from the following list:

- Good: this is a usable tower
- Hot: this tower fires too often or indiscriminately
- Dead: this tower does not fire with high enough frequency to be reliable
- Uncalibrated: this tower was not able to be calibrated properly (gain calibration)
- Edge: this tower is on the edge of a sector and is not able to be used
- Around Hot/Dead/Uncalibrated: A tower adjacent to a hot, dead, or uncalibrated tower

The EMCal is divided into eight physical sectors, there is thus one warnmap for each sector. Figure 4.6 shows the number of EMCal hits with p_T between $0.5\frac{GeV}{c}$ and $0.8\frac{GeV}{c}$ for all runs in the analysis. The colors correspond to different EMCal physical sectors. Many outlier towers can be seen. A distribution of the number of hits in a single EMCal sector in the same p_T region can be seen in Figure 4.7. The green lines in this figure are $3 \cdot \sigma$ from the mean of the Gaussian fit; towers below the lower green line are considered "dead" and towers above the upper green line are considered "hot". Each of which are eliminated from the analysis and can be seen in Figure 4.8.

Since the Moliere radius of the EMCal material is roughly the width of three EMCal towers, a single electromagnetic cluster is composed of a 3x3 grid of towers. If a single tower in that 3x3 grid is deemed bad (hot, dead, or uncalibrated), the cluster itself cannot be used. To prevent this, the towers around (touching) a bad tower are also eliminated from being a central tower in the cluster.

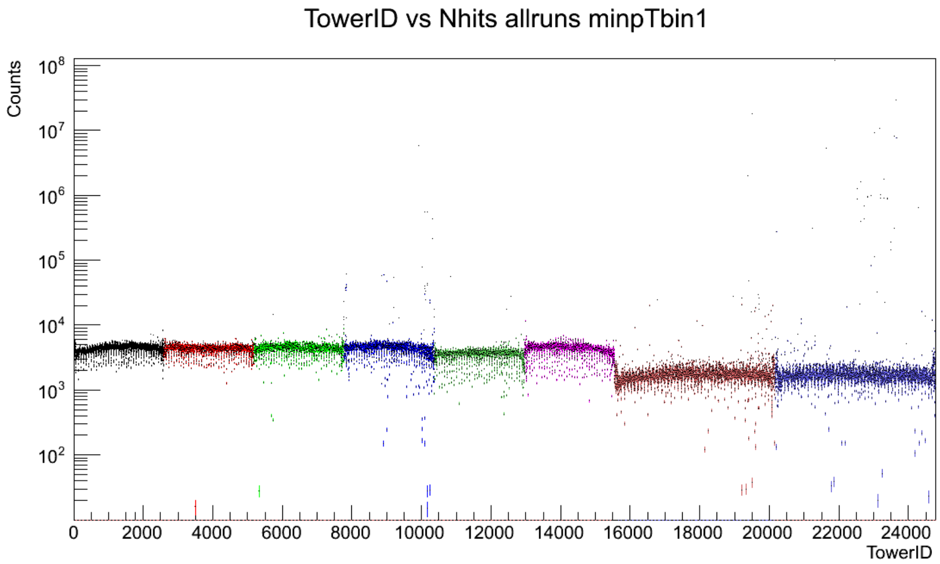

Figure 4.6 Number of EMCal hits per tower with p_T between 0.5 $\frac{GeV}{c}$ and 0.8 $\frac{GeV}{c}$ for all runs. X-axis is a tower identification number; Y-axis is counts.

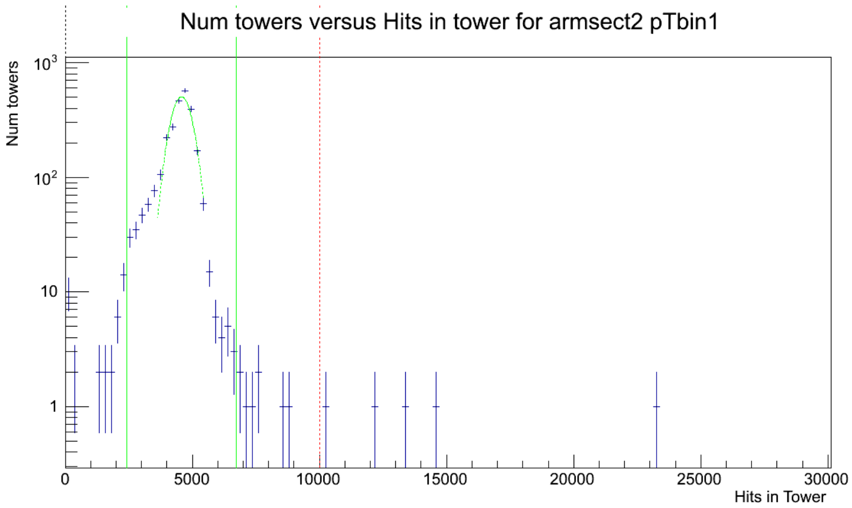

Figure 4.7 Distribution of the number of EMCal hits in Sector #2 between a p_T of 0.5 $\frac{GeV}{c}$ and 0.8 $\frac{GeV}{c}$. The red line represents an iterative upper limit (hot) cut. The green lines are 3σ from the mean of the Gaussian fit; they represent the final lower (dead) and upper (hot) cuts used in the analysis.

4.5 Drift Chamber Modified Quality Map

For a measurement that is attempting to reconstruct jets it is important to understand detector acceptance (active area). It is also important to have as uniform of acceptance as possible. To aid in this goal, a modified quality map for the DC and PC1 detectors is used. A complex pattern recognition system is used to take a system of X1, X2, U, V, and PC1 detector hits and filter them such that charged tracks can be properly reconstructed. A summary of the track finding procedure can be found in Reference [53]. For a charged track to be reconstructed we can require the following criteria:

- An X1 wire hit is used in the reconstruction
- An X2 wire hit is used in the reconstruction
- A U and V set of wire hits were found, unambiguous, used in the reconstruction
- A PC1 hit is found, unambiguous, and used in the reconstruction

However, there are several known broken or dead X1, X2, U, and V wires. Since these wires are known dead, no tracks in that acceptance region can be used. The total dead area because of these requirements can be seen on the left side of Figure 4.12. This level of track quality isn't required for this analysis, it is more important to have increased acceptance and good track quality. To achieve this, mappings of the known dead wires were made. These can be seen in Figures 4.9 to 4.12. Using this modified quality mapping, we can require the following criteria for a reconstructed track:

- If the track is in a good X1, X2, and UV region we require the previous criteria
- If the track is in a known bad X1 region we require that we find an X2, UV hit found and unambiguous, and PC1 hit found
- If the track is in a known bad X2 region we require that we find an X1, UV hit found and unambiguous, and PC1 hit found
- If the track is in a known bad UV region we require that we find an X1, X2, and PC1 hit found and unambiguous

Due to the wire orientations within the DC and PC1 detectors each wire provides better resolution in one direction and worse resolution orthogonally. The X1 and X2 wires primarily provide track ϕ-positioning. The PC1 provides precise track z-positioning. The UV wires provide both track ϕ-positioning and z-positioning (with less precision than PC1) [53]. There is no PC1 modified warnmap as a PC1 hit is always required for an accepted track.

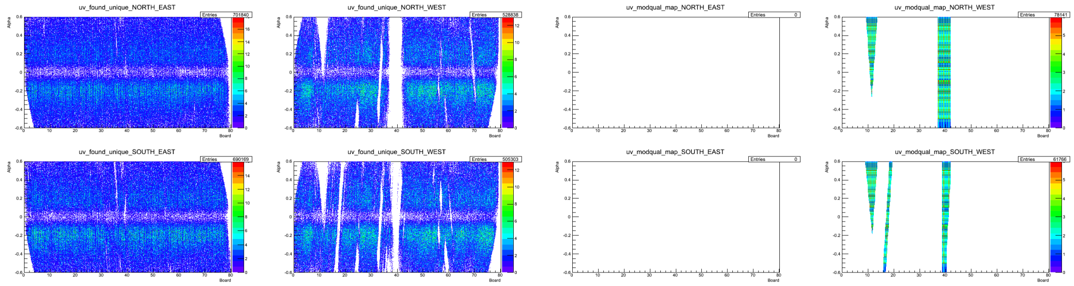

Figure 4.9 Various DC physical sections. Left: Real data, distribution of tracks with UV wire hit found, unique, and associated with a track. Right: Modified quality map applied to UV hits. X-axis: Board number; Y-axis: Track alpha value

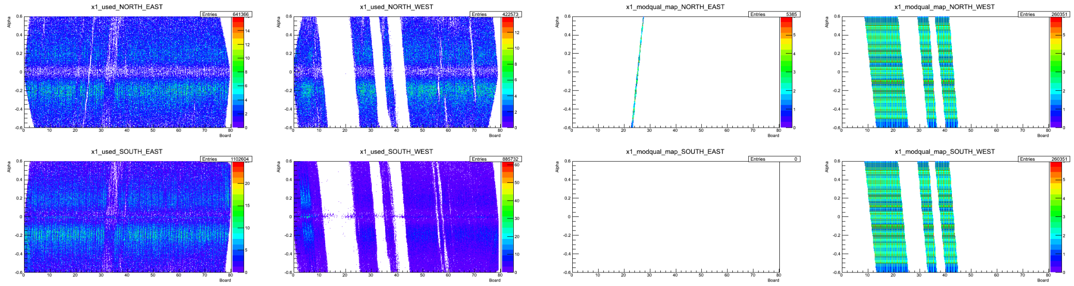

Figure 4.10 Various DC physical sections. Left: Real data, distribution of tracks with X1 wire hit found and associated with a track. Right: Modified quality map applied to X1 hits. X-axis: Board number; Y-axis: Track alpha value

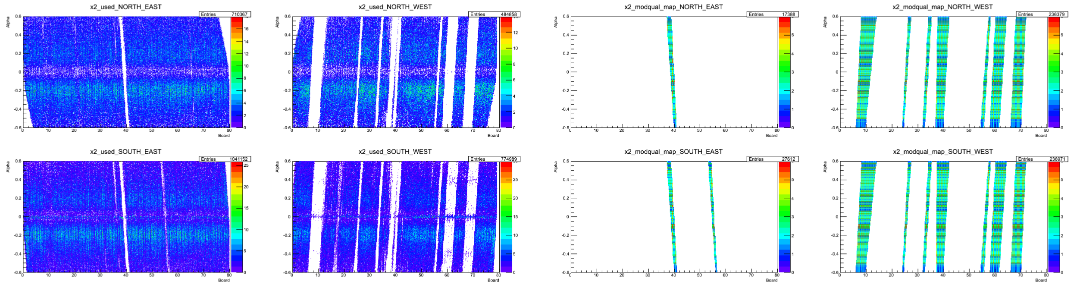

Figure 4.11 Various DC physical sections. Left: Real data, distribution of tracks with X2 wire hit found and associated with a track. Right: Modified quality map applied to X2 hits. X-axis: Board number; Y-axis: Track alpha value

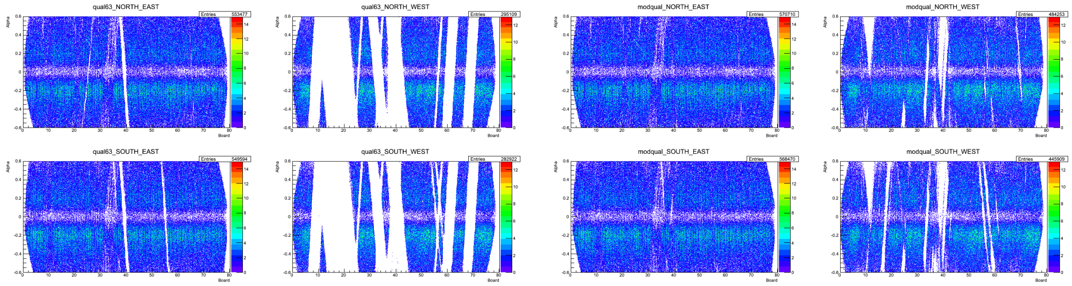

Figure 4.12 Various DC physical sections. Left: Real data, distribution of tracks with UV (unique), X1, and X2 wire hit found and associated with a track. Right: Modified quality map applied. X-axis: Board number; Y-axis: Track alpha value

4.6 MPC Calibration

The calibration of the North MPC detector for Run-12 proton-proton running was performed primarily by myself. The full details of the calibration can be found in PHENIX Analysis Note 1094 [54]. The calibration consists of several parts:

1. Identification of the point at which the Analog-to-Digital Converters (ADCs) values overflow and cutting out said ADC values (Figure 4.13).

2. Identification of the point at which the Time-to-Digital Converters (TDCs) values overflow and cutting out said TDC values (Figure 4.13).
3. Determining the ratio of the Low-gain ADC to High-gain ADC such that their combination can yield a true and continuous single ADC spectrum (Figure 4.14).
4. Reconstruction of two-cluster π^0 masses for each tower (Figure 4.15).
5. Iteratively adjusting the gain of each tower such that the π^0 mass measured by each tower is correct (Figure 4.16).
6. Reconstruction of two-cluster π^0 masses for each run (over time) and adjusting the global gain value (for all towers) as a function to time to correct for transient effects such as temperature variations which impact APD gain (Figure 4.17).

The final calibration values mentioned above were added to the PHENIX calibration database for use by the collaboration and were all utilized in this analysis.

4.7 Triggering and Statistics

The data set used in this analysis was gathered using a coincidence trigger between the central arms and the MPC detectors. The central arm trigger, called the ERT2x2, is a trigger which sums the energy in EMCal towers in a 2x2 area and issues a trigger if that energy is above some threshold (roughly $700MeV$ for the ERT2x2 in Run-12). Similarly, the MPC portion of the coincidence trigger was the MPC4x4c, which sums energy in a 4x4 grid and issues a trigger if it above its threshold (roughly $2.0GeV$). A total of roughly 150 million coincidence triggers were analyzed in this analysis.

The projected integrated luminosity of transversely polarized proton-proton collisions at $\sqrt{s} = 200\frac{GeV}{c^2}$ available for this analysis between Run-12 and Run-13 was roughly $66\frac{1}{pb}$ (pb is pico-barns) over a total of 10 weeks [55] of run time ([56],[57]). The sampled luminosity was roughly half that ($37.9\frac{1}{pb}$) over 4.4 weeks as the Run-13 portion of transverse proton-proton running did not occur [58].

Additionally, the projected total analyzable statistics included the use of the South arm MPC detector, but its calibration with newly installed electronics was not ready at the time of this analysis. These two compounding factors reduced the size of the expected statistical sample greatly.

4.8 Track Quality Assurance

Using the track to EMCal matching from Section 4.3 we eliminate a EMCal cluster from the analysis if it is within 3.0σ from a reconstructed track. This eliminates double counting of a track and its associated energy deposit in the EMCal. Additionally, a set of ghost and DC internal conversion cuts are utilized, these are itemized below:

- Ghost pair definition: for same charge pair, if $|\Delta\phi| < 0.024$ rad and $|\Delta z| < 0.066$ cm it is a "ghost"
- If asymmetry in p_T of ghost pairs $(\frac{p_{T\,i} - p_{T\,j}}{p_{T\,i} + p_{T\,j}}) < 0.3$, reject one track; else, reject both tracks
- For different charge pair, if $|\Delta\phi| < 0.072$ rad and $|\Delta z| < 0.066$ cm, reject both tracks

4.8.1 Conversion Electrons

Conversion electrons come from the process $\gamma \rightarrow e^+ + e^-$. The location of the conversion production impacts the reconstructed momentum of the detected electron/positron. A simulation was performed by Sasha Lebedev in which he produced π^0s with a flat p_T distribution from 1 GeV to 10 GeV (Dalitz decay disabled) [59]. The π^0s then decay to photons and produce conversions in the material of the simulated detector (using PISA). The source of detected conversion electrons can be seen in Figure 4.19 [60]. A comparison of truth ($p_{T,true}$) and reconstructed ($p_{T,rec}$) conversion electron momenta can be seen in Figure 4.18. A minimum track p_T cut of 500 MeV is used and eliminates a large portion of the misreconstructed conversions. The band at $p_{T,true} = p_{T,rec}$ are conversion electrons that are properly unreconstructed. The band at $p_{T,true} \approx 0$ are incorrectly reconstructed and must be eliminated.

The conversions from the beam-pipe can be seen at very small R-value and z-vertex = 0. If the conversion happens at the beam-pipe the electron/positron still traverses the entire length of magnetic field and can be detected by the central arm tracking systems; in this case, the reconstructed momentum is roughly correct. The VTX detector in PHENIX (Figure 3.8) sits just outside the beam pipe at roughly $3cm < R < 17cm$ and was a candidate for conversion production, but it produces negligible background as can be seen here. The VTX detector is not used in this analysis.

If the conversion happens at the face of the Drift Chamber the electron momentum vector is incorrectly reconstructed as its α value (Figure 4.2) will be extremely small. The reconstructed momentum will thus be much higher than the real momentum of the electron. The face of the Drift Chamber sits at a nominal R=220cm; a band of conversion electrons at that radius can be seen in Figure 4.19. The locations of conversion electrons in z-ϕ space at a radius of roughly 220cm can be seen in Figure 4.20. The four vertical bands of conversions are the locations of the edges of the Drift Chamber's physical sections in the West arm (the East has similar features). Charged tracks pointing back to the regions within the red dashed lines are eliminated from the analysis.

The charged track is then matched to an EMCal cluster (Section 4.3). The charged particle deposits energy in the EMCal via the mechanisms discussed in Section 3.3.2 to give the equation $E(x) = E_0 e^{\frac{-x}{X_0}}$ where the total integrated energy is related to the incident momentum. A conversion electron will have a measured $E_0 \approx |\overrightarrow{p_{e^{\pm}}}|$ that is too large when matched to the integrated $\frac{dE}{dx}$ energy loss in the EMCal material. This situation can be seen in Figure 4.21.

The conversion cuts used in the analysis are the following:

- Track eliminated if: (ϕ0 > -0.65 and ϕ0 < -0.49)
- Track eliminated if: (ϕ0 > 0.89 and ϕ0 < 1.05)
- Track eliminated if: (ϕ0 > 2.10 and ϕ0 < 2.26)
- Track eliminated if: (ϕ0 > 3.62 and ϕ0 < 3.78)
- Track eliminated if: $\sqrt{sd\phi^2{}_{emc} + sdz^2{}_{emc}} < 3.0$ and ecore < 200 MeV
- Track eliminated if: $p_T < 4.5$ and n0 >= 2 and (ecore / momentum) < 0.6

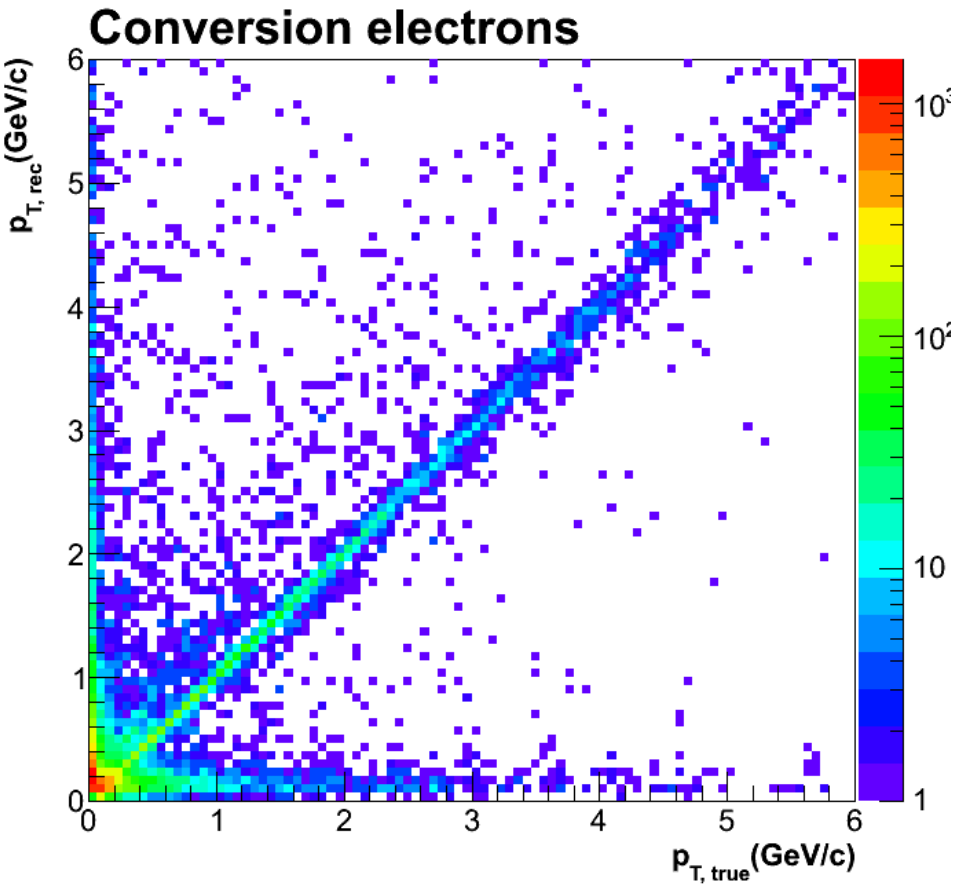

Figure 4.18 The p_T spectrum of conversion electrons from simulation. The region that needs to be reduced or eliminated is when a conversion electron/positron reconstructs with high-p_T when it should not have (the left-most region of the plot). Y-axis: Reconstructed p_T, X-axis: True p_T.

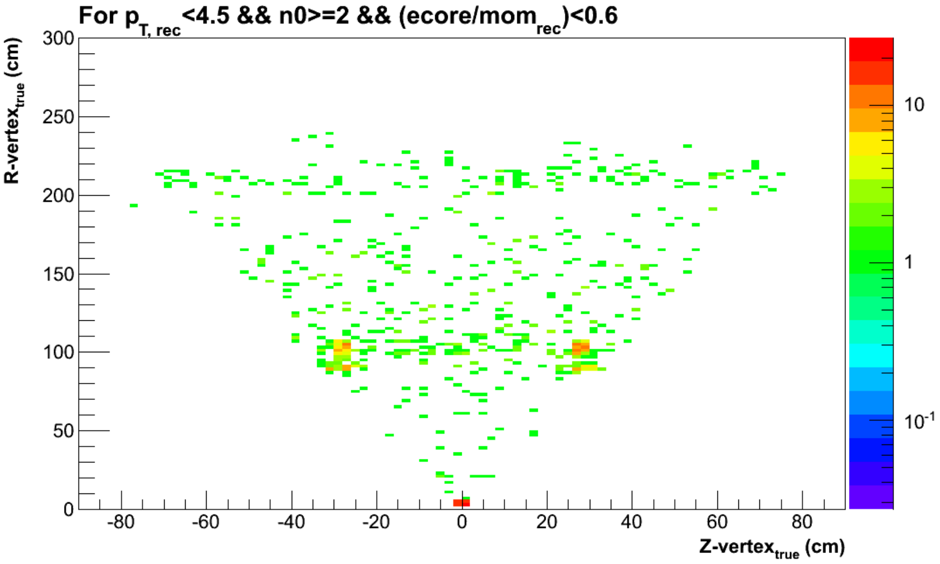

Figure 4.19 Location in R-z space in which a detected conversion electron was created. The red concentration at roughly z=0 and R=5 is due to the beam pipe.

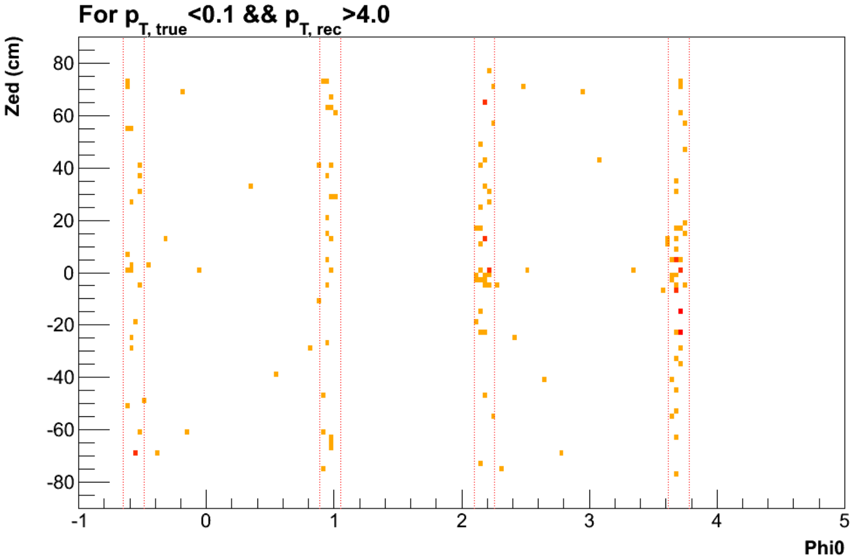

Figure 4.20 The location in ϕ0-z space on the face of the DC from which conversion electrons originated. The red bands surround mechanical staging, those regions have been eliminated from the analysis.

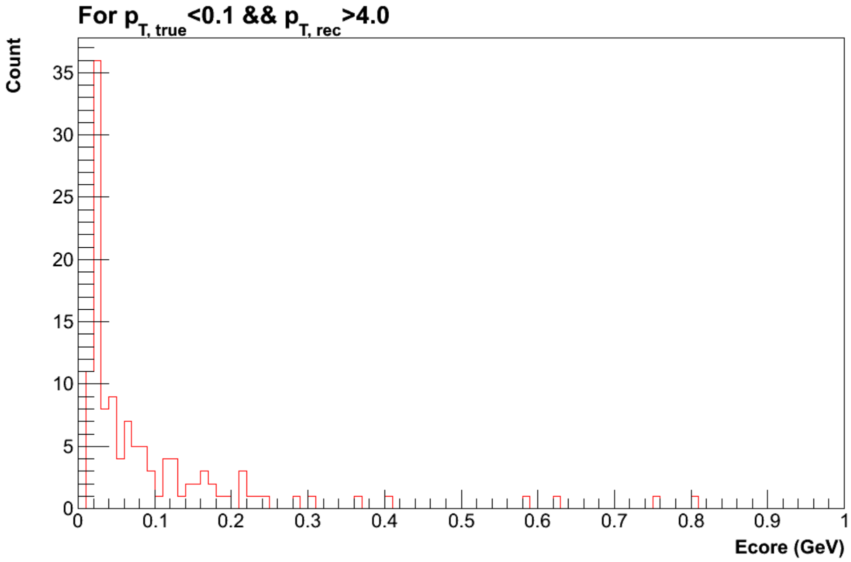

Figure 4.21 The Ecore (EMCal energy deposition) for a misreconstructed conversion electron where $p_{T\,true} < 0.1\frac{GeV}{c}$ and $p_{T\,reco} > 4.0\frac{GeV}{c}$. Tracks which deposit minimal energy into the EMCal were eliminated from the analysis.

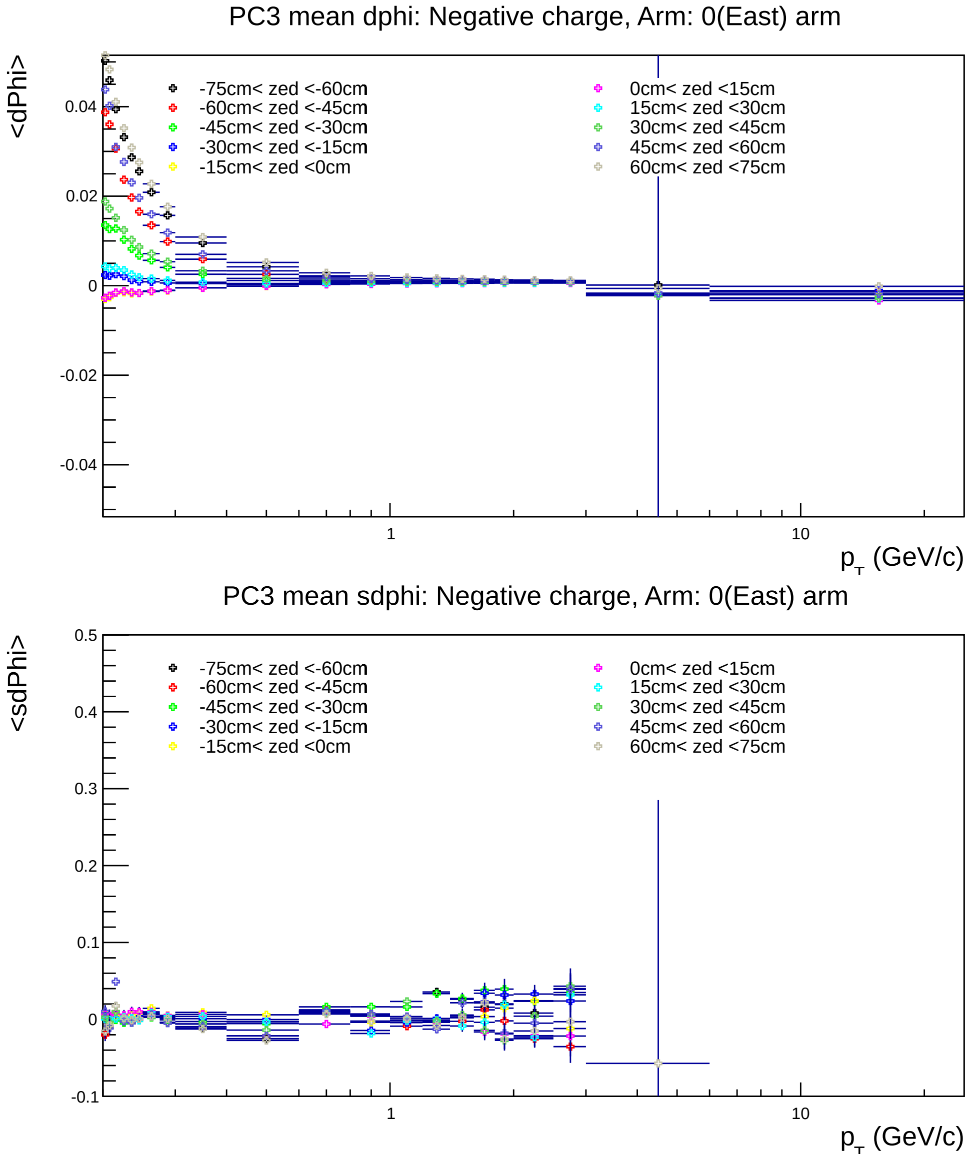

Figure 4.5 Sigmalized mean distributions versus p_T for negatively charged particles in the East arm. Top: Before calibration, y-axis is absolute physical units; Bottom: After calibration, y-axis is sigma

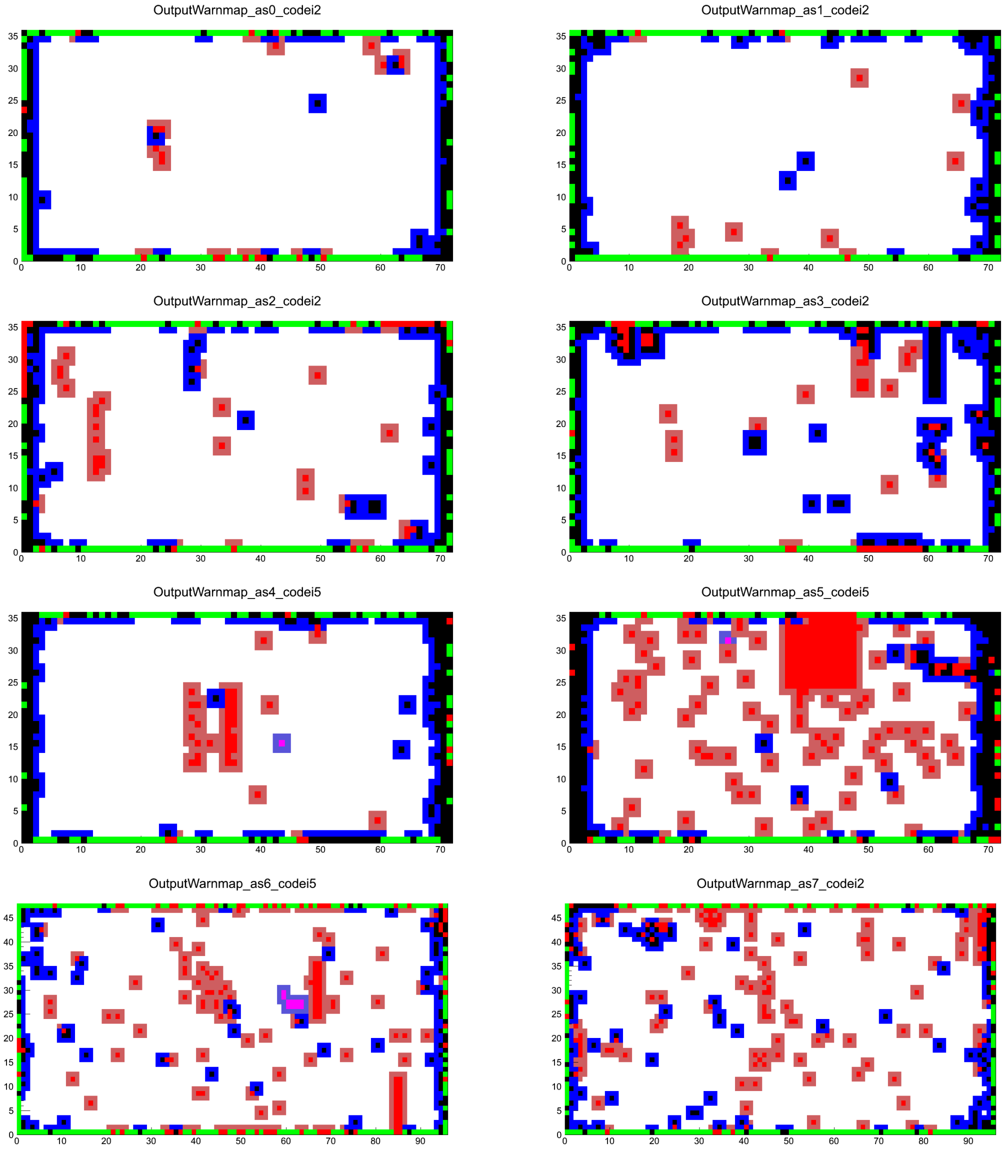

Figure 4.8 EMCal warnmaps, one for each sector. Colors and precedence: Black = Dead, Blue = Around Dead, Red = Hot, Light Red = Around Hot, Pink = Uncalib, Purple = Around Uncalib, Green = Edge. The plots labeled “as6/7” are the PbGl sectors.

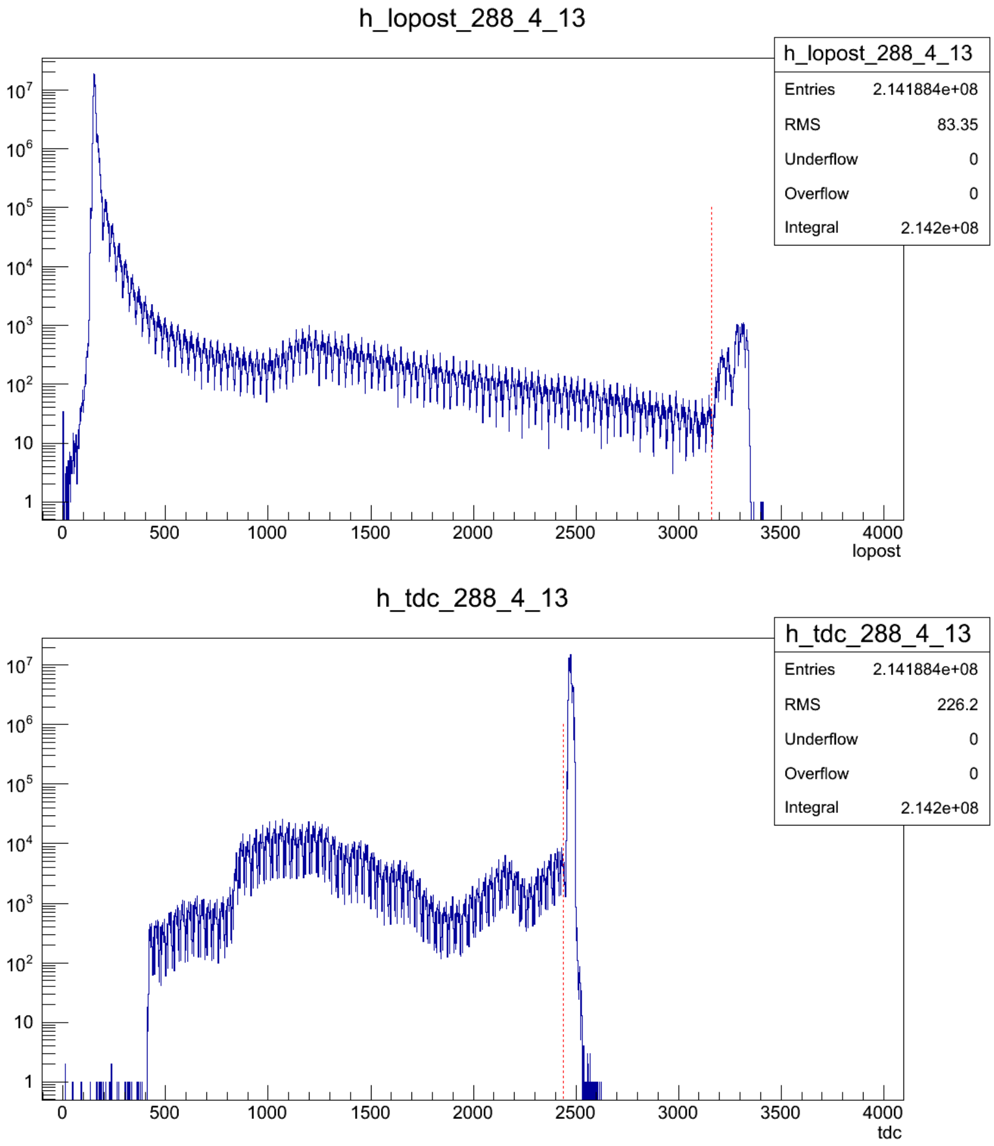

Figure 4.13 Top: corrected low-gain ADC distribution and ADC overflow cut, Bottom: TDC distribution and TDC overflow cut. The vertical dashed red lines represent the overflow cut values used for this tower.

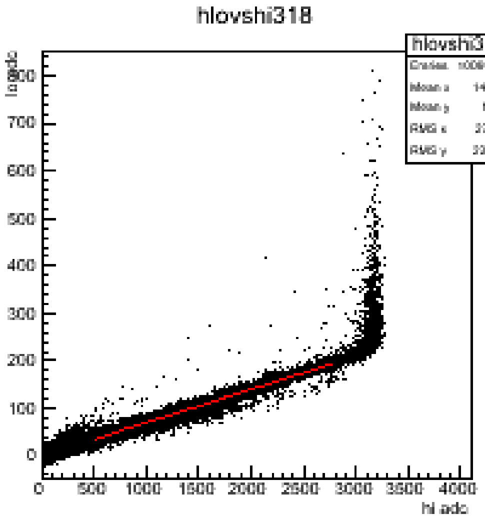

Figure 4.14 X-axis: High gain ADC; Y-axis: Low gain ADC; Left and Right are two different towers.

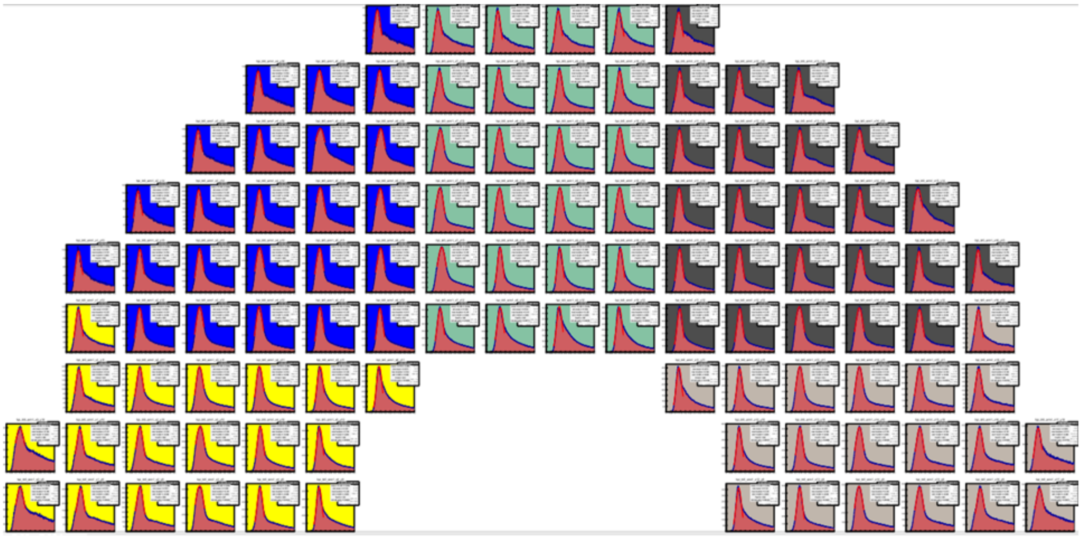

Figure 4.15 The top half of the North MPC. Each plot is a single tower. The color code identifies regions of common electronics. X-axis: Reconstructed mass; Y-axis: Counts.

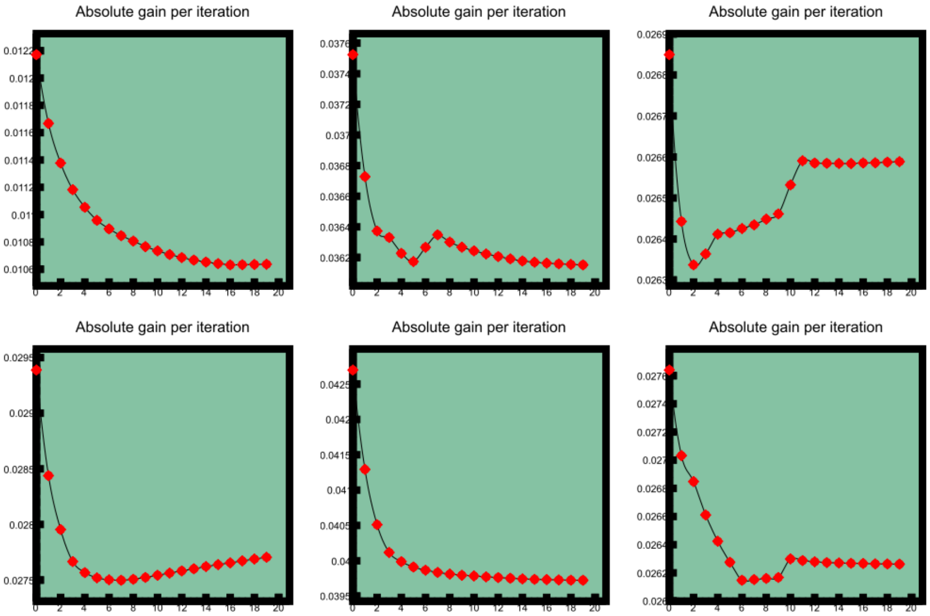

Figure 4.16 X-axis: Iteration number; Y-axis: Tower gain value; A representative sample of towers is shown. The green background implies that the towers are all connected to common electronics as seen in Figure 4.15. The gain of each tower depends on the gain of all other towers, so a stable gain for a tower may change as other towers' gains are updated (as can be seen in the lower-right figure).

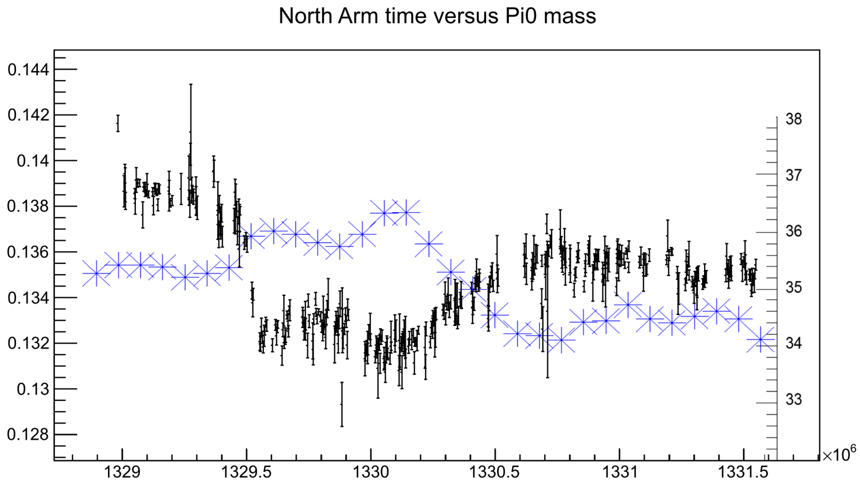

Figure 4.17 X-axis: Time; Y-axis, left (black points): Average North arm reconstructed π^0 mass value; Y-axis, right (blue points): Thermocouple temperature reading, relative scale.

CHAPTER 5. ANALYSIS METHOD

An ideal scenario for measuring the Collins-induced asymmetry in proton-proton collisions would be if a forward-going (high-x) quark were to fragment (shower) into a detector system placed at large pseudorapidity. If the detector system was built to reconstruct jets at forward rapidity one could detect both a forward jet and a single π^0 within that jet in an event. One could then relate the forward parton's momentum vector (approximated from jet reconstruction) and spin axis (due to parton transversity in the polarized proton) to the π^0 momentum vector. An asymmetry here would be purely due to the Collins' effect during the fragmentation of the quark to the π^0. Since there does not exist a forward jet detector at a high-energy polarized-proton accelerator/collider facility we

From this crayon-physics level picture one can see that this “Boost, Flip, and Swap” procedure allows for the determination of the “jet proxy” which in turn allows us to approximate the forward quark's direction.

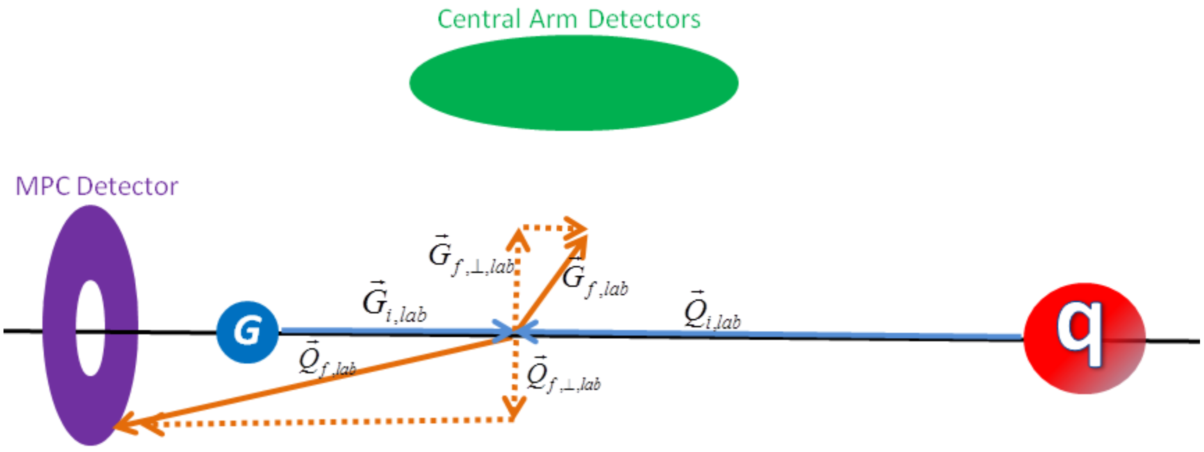

Figure 5.1 Lab frame quark-gluon 2→2 scattering with no initial-state k_T

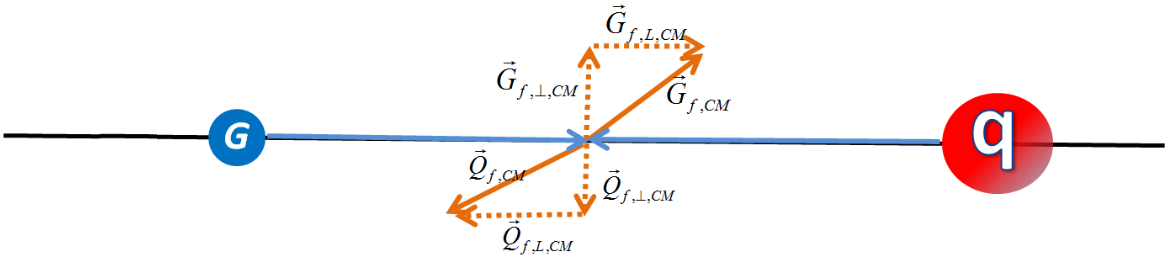

Figure 5.2 Center-of-momentum frame of the final-state quark and gluon system

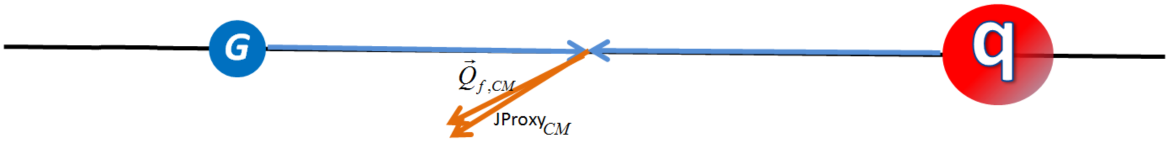

Figure 5.3 Final-state forward quark and “jet proxy” in the center-of-momentum frame

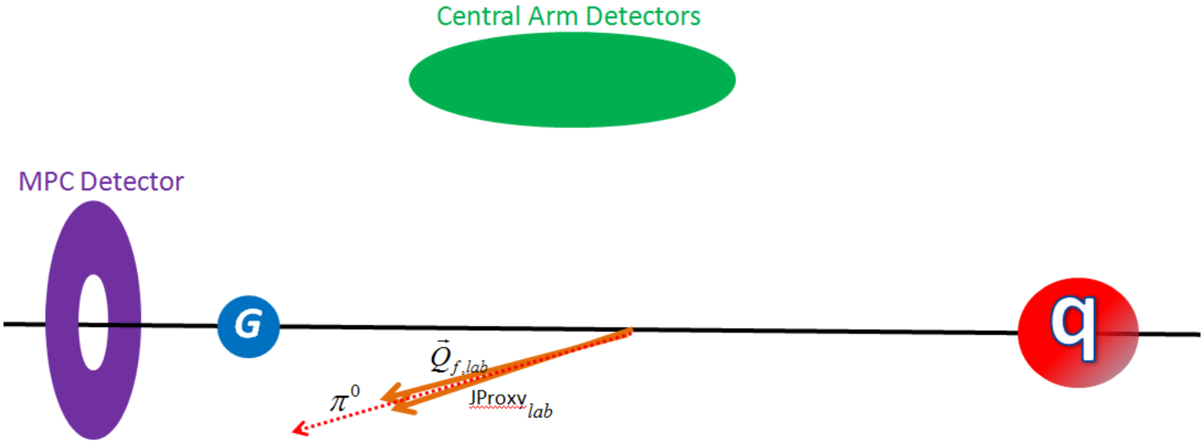

Figure 5.4 Final-state forward quark, π^0, and “jet proxy” in the lab frame

5.1 Conservation of Momentum

The analysis method used here is conceptually based on a QCD leading-order 2→2 scattering scenario. In a leading-order 2→2 process the initial state partons are assumed to have zero momentum in the transverse plane (k_T). Since there is a vector-sum of zero k_T in the initial state there must be a vector-sum of zero k_T in the final state due to momentum conservation. This implies that the transverse momentum of the two final-state partons must be equal in magnitude and opposite in direction (Equation 5.1 and Figure 5.5). Because of this symmetry, if we can reconstruct the $\overrightarrow{k_T}$ of one of the final state partons we can determine the $\overrightarrow{k_T}$ of the other. While momentum conservation does apply to the z-momentum of the 2→2 scattering system it is not utilized as an explicit input to the analysis. Information about the partons' initial state z-momentum (partonic longitudinal momentum fraction of the proton) is unknown on an event-by-event basis, so z-momentum conservation is exploited between the initial-state and final-state as an assumption that is satisfied exactly on an event-by-event basis (Figure 5.6).

$$\overrightarrow{p1}_{f_\perp} = -\overrightarrow{p2}_{f_\perp} \tag{5.1}$$

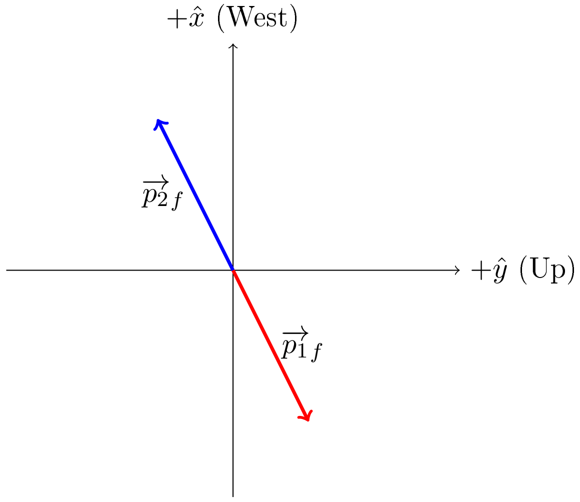

Figure 5.5 Conceptual drawing of parton-parton 2→2 scattering in the transverse plane with no initial state k_T. The proton beams are into and out of the page on this figure.

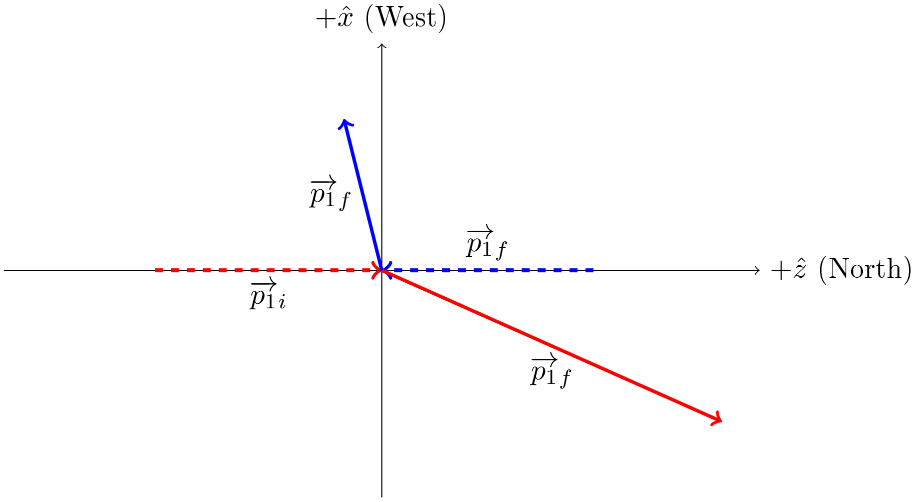

Figure 5.6 Conceptual drawing of parton-parton 2→2 scattering in the x-z plane with no initial state k_T. The proton beams momentum vectors are along the ±z-axes in this picture.

5.2 Analysis Requirements

Since it is not possible to observe the final state partons directly we must infer their properties via jet reconstruction (Section 5.3).

A main challenge in this analysis is working with the limitations presented by the available detector systems for jet reconstruction and detector acceptance at forward rapidities in the PHENIX experiment. As stated previously, a strong Collins' asymmetry is present at high-x which, experimentally, means looking at large values of pseudorapidity (η). The PHENIX experiment has only one detector which can measure neutral pions at large (non-infinite) values of η. This detector is the MPC discussed previously in Section 3.3.8. The MPC cannot reconstruct a full jet axis with its limited acceptance and emphasis on electromagnetic cluster (photon) detection while being mostly blind to the hadronic and charged particle portions of a jet.

The PHENIX's central arm, however, is able to reconstruct jets within its acceptance using the central arm detectors discussed in Section 3.3. We are able to successfully reconstruct jets in the central arm acceptance in both simulation and real data (Section 5.3.4). The basic final-state kinematic event structure is thus a reconstructed jet in one of the PHENIX central arms coupled with a π^0 (electromagnetic cluster) in the North MPC detector as seen in Figure 5.7. These kinematic requirements bias our partonic final-state to central-going gluon and a forward-going quark (See Section 5.5).

Given a reconstructed jet in the PHENIX central arm acceptance we can approximate the transverse component of the central-going final-state partons' kinematics ($\overrightarrow{p}_{cent,f,\perp}$) (Section 5.3.4). Similarly, a North MPC π^0 can be correlated with the forward-going quark. Thus, two requirements of this analysis are that we must reconstruct a central arm jet and an MPC π^0. Additionally, the central arm jet and the MPC π^0 must be separated by an opening angle in ϕ by more than $\frac{2\pi}{3}$ (i.e. the jet and π^0 must be roughly back-to-back in ϕ). The next sections cover these requirements.

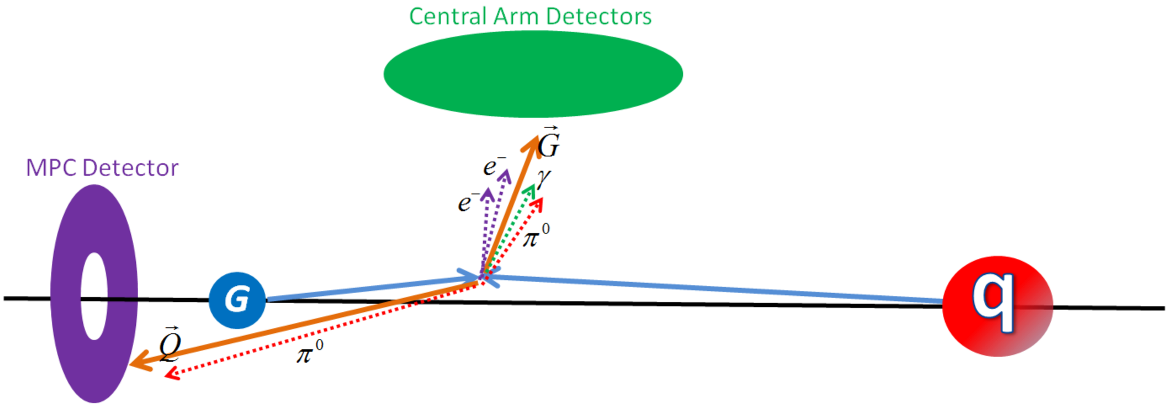

Figure 5.7 Quark-gluon 2→2 scattering with fragmentation. The gluon produces a jet detected by the central arm and the quark produces a pi^0 detected by the North MPC.

5.3 Jets

The definitions of a "jet" are varied and often disparate. Michael J. Tannenbaum of Brookhaven National Laboratory has summed the matter up nicely when he said (paraphrased) "a jet is not a physical quantity but a legal contract between experimentalists and theorists" [61]. The "legal contract" I am using here is the following:

- Given a set of QA-filtered final-state charged tracks and electromagnetic clusters I perform an *anti*$-k_T$ sequential recombination to find "inclusive" jets (using the FastJet package in decreasing-p_T-ordering mode) with a specific "R" parameter (Section 5.3.2).
- The set of jets has QA performed through a series of cuts based on simulation study results (Section 5.3.3).
- The final set of jet kinematics are used as an approximation of post-scattering partonic kinematics (Section 5.5).

The specifics of each contract clause is presented in subsequent sections.

5.3.1 Jet Reconstruction

The field of jet reconstruction in high energy physics is vast, I will only be covering a single technique in the family "sequential recombination" algorithms. Many techniques used in other experiments are not applicable to this data set due to limited acceptance, hadronic blindness, and maximum p_T reach. The algorithm used here for coalescing our collection of particles into a reconstructed jet is the *anti*$-k_T$ algorithm applied by the FastJet [62] software package.

5.3.2 *Anti*$-k_T$ Algorithm

The *anti*$-k_T$ algorithm can be summarized as an algorithm which takes momentum vectors in $\eta-\phi$ space and sequentially combines them using a weighting based on their transverse momentum and spatial separation. The moniker *anti*$-k_T$ is used to emphasize that the recombination scheme incorporates the k_T of each particle raised to a negative power (inverse of k_T). When particles are combined in this manner during intermediate iterations of the algorithm the objects are called "pseudojets" since they are neither real particles nor full jets. Throughout this section all statements that apply to "particles" also apply to "pseudojets". The *anti*$-k_T$ algorithm is an infrared-safe in regards to the number of jets found when a minimum particle p_T cut is enforced, which is the case in this analysis [63].

The $anti{-}k_T$ algorithm's first step is determining a distance parameter between particle pairs as defined by Equation 5.2.

$$d_{ij} = d_{ji} = min(p_{\perp,i}^{-2}, p_{\perp,j}^{-2})\frac{\Delta p_{i,j}^{-2}}{R^2} \tag{5.2}$$

Where:

- i,j = index of all particles in the system
- $\Delta R_{i,j}$ = distance in $\eta - \phi$ space ($\sqrt{\Delta\eta^2 + \Delta\phi^2}$) between particles i,j.
- R = a parameter of the algorithm which roughly describes the size of the jet, though the jet boundaries are mutable based on combined particle/jet p_T and location.
- $p_{\perp,i}$ and $p_{\perp,j}$ = the transverse momentum of particles i,j.
- d_{ij} = $anti{-}k_T$ algorithm calculated distance parameter between particles i,j.

Since we are using an "inclusive" formulation of the $anti - k_T$ algorithm, once the smallest d_{ij} value for the set of particles is found we perform one of two actions:

- If the smallest d_{ij} value is smaller than (or equal to) $p_{\perp,i}^{-2}$ then particle/"pseudojet" i is assumed to be a final "inclusive" jet and is removed from the list of particles/"pseudojets" and is saved.
- If the smallest d_{ij} is larger than $p_{\perp,i}^{-2}$ then particles i and j are combined using simple momentum-vector addition into a "pseudojet".

Because only the smallest of d_{ij} values are used in the recombination procedure the $anti{-}k_T$ algorithm is also infrared- and collinear-safe in terms of jet shape and direction; i.e. adding an arbitrary number of soft particles (radiation) to an event cannot change the jet direction or shape. The algorithm is considered "soft-resilient" since soft particles can change the final jet p_T unless a minimum particle p_T cut is used, which this analysis does. Once all particles in an event are clustered into jets the iterative procedure stops.

A sample event that has had the $anti-k_T$ algorithm performed on a sample of hard particles embedded in a soft particle background is shown in Figure 5.8. In Figure 5.8 the green colored area (upper-right) is an example of a jet formed from a hard particle and the soft background. The soft background has no influence on the jet boundary in this case. The purple colored area (to the left of the green area) is a jet formed from several mid-p_T particles and the soft background. One can see that the purple area's boundary is deformed due to the higher p_T (harder) green jet and does not influence the green jet itself. The area encompassed by each jet is roughly equal to πR^2 even if the boundary shape is deformed. The jets that the $anti-k_T$ algorithm gives us are not all useful or interpretable, a series of QA cuts are placed on these jets to reduce the number of fake or misreconstructed jets. These cuts are covered in Section 5.3.3.

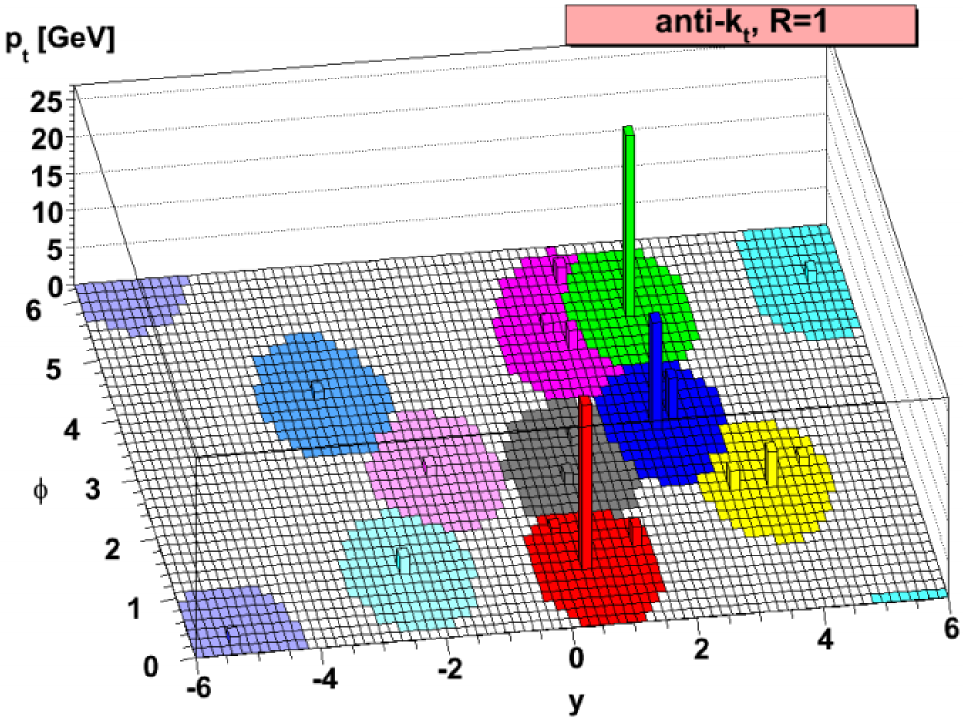

Figure 5.8 A sample parton-level event with added random soft particles. The $anti-k_T$ algorithm clustering was performed on the event. Differing colors represent the areas of various jets. [63]

5.3.3 Jet Cuts

All particles that are fed into the $anti{-}k_T$ algorithm for jet reconstruction have all of the QA checks and cuts covered in Chapter 4. The following jet-level cuts are applied to the final-state $anti{-}k_T$ reconstructed jets (each cut is explained in the subsequent sections):

- We require that Jet $p_T \geq 5.0\frac{GeV}{c}$.
- The number of constituent particles used to form the jet ($N_{constituents}$) is ≥ 3.
- Jet "charged fraction (CF)" where $CF = \sum_{i=chargedconstituents} \frac{\vec{p}_i \cdot \hat{p}_{jet}}{|\vec{p}_{jet}|}$ and the allowed jets meet the requirement that $CF < 0.8$.

5.3.4 Jet Reconstruction Results

The results of the track, cluster, event, and jet-level cuts are a clean jet sample that we can use for this analysis. Figures 5.9 to 5.11 show the effect of the jet charged fraction cut, which was crucial to this analysis. Figure 5.9 shows the effect of the charged fraction cut on the constituent contributions to the jet momentum. Figure 5.10 shows the high degree of contamination that is eliminated due to the 0.8 upper limit on the jet charged fraction. The final jet p_T distribution can be seen in Figure 5.11 in the green points matching "Jet CF $<$ 0.8".

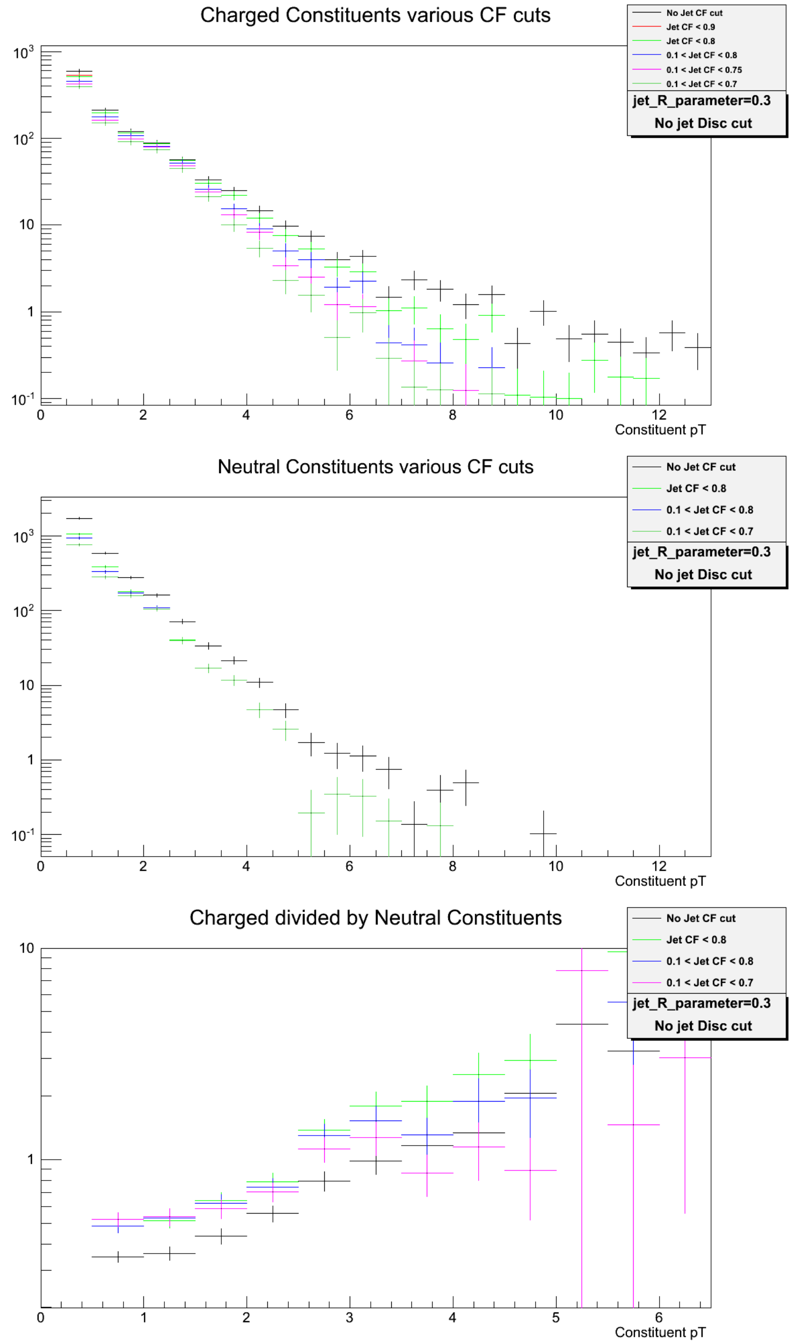

Figure 5.9 p_T distribution of charged constituents within a reconstructed jet.

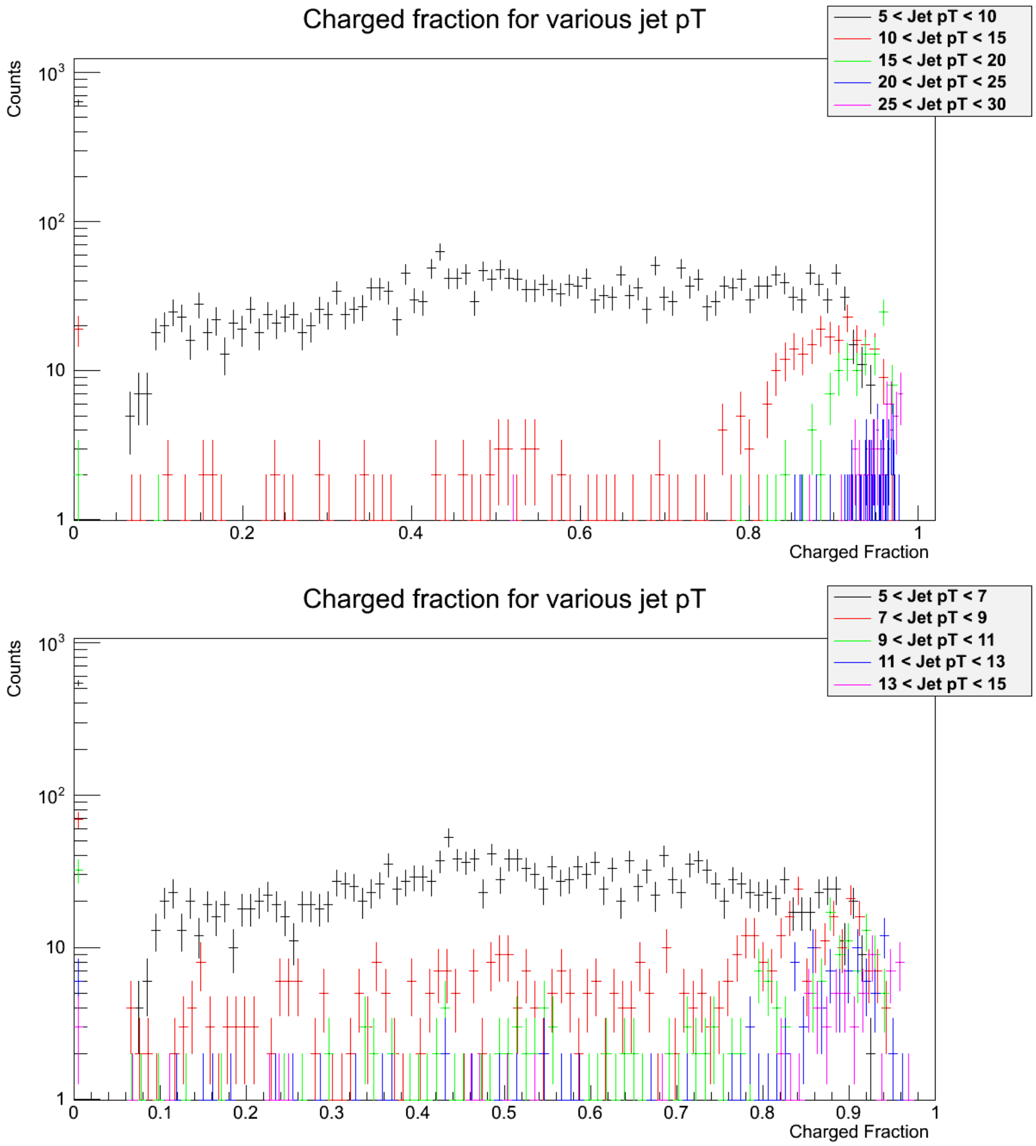

Figure 5.10 Jet charged fraction for different jet p_T regions.

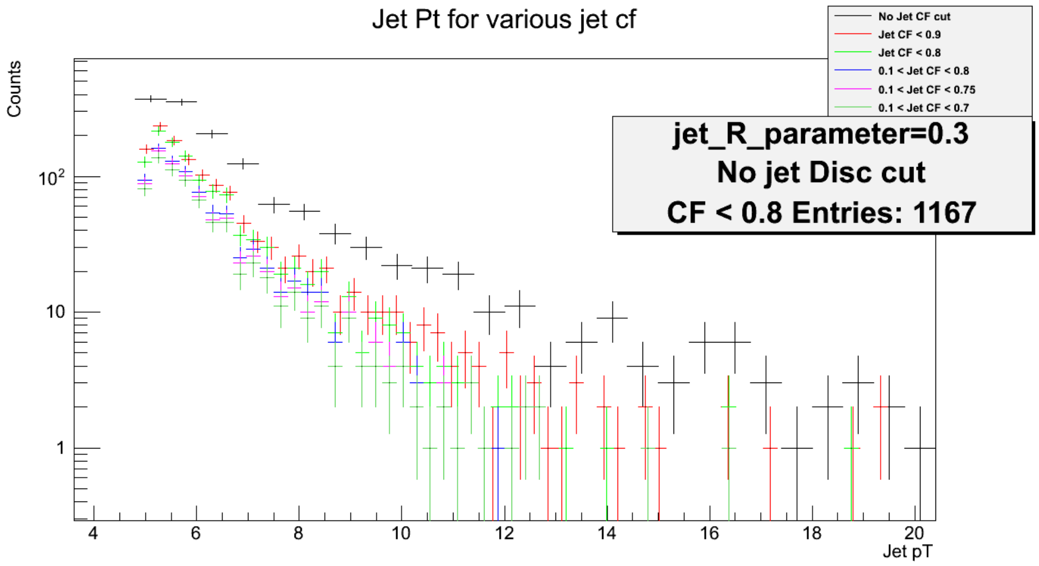

Figure 5.11 The bright green curve represents the final reconstructed jet p_T raw spectrum using our charged fraction upper limit of 0.8. The X-axis is reconstructed jet p_T.

5.4 North MPC π^0s

The set of cuts used on the MPC data is basically standardized over many analyses [64]. The cuts used are the following (specific definitions can be found in [64]):

- Maximum allowed χ^2 shape cut value: 2.0
- Maximum allowed value of the central tower energy divided by the total cluster energy ($\frac{E_{cent}}{E_9}$): 0.95
- Maximum allowed cluster dispersion value: 4.0
- Minimum allowed photon probability cut (shape cut): 0.01
- Minimum radius in the transverse plane for the cluster center: 11cm
- Maximum radius in the transverse plane for the cluster center: 19cm
- Minimum allowed ΔR between clusters in the transverse plane: 2.6cm

- Cluster p_T between 1.0 $\frac{GeV}{c}$ and 3.0 $\frac{GeV}{c}$ in the lab frame.

The final MPC π^0 (single-cluster) p_T distribution is shown in Figure 5.12. The sample shown also required a coincident central jet. The composition of said clusters as a function of p_T was studied by the MPC group, the results of which can be found in Figure 5.13 [64].

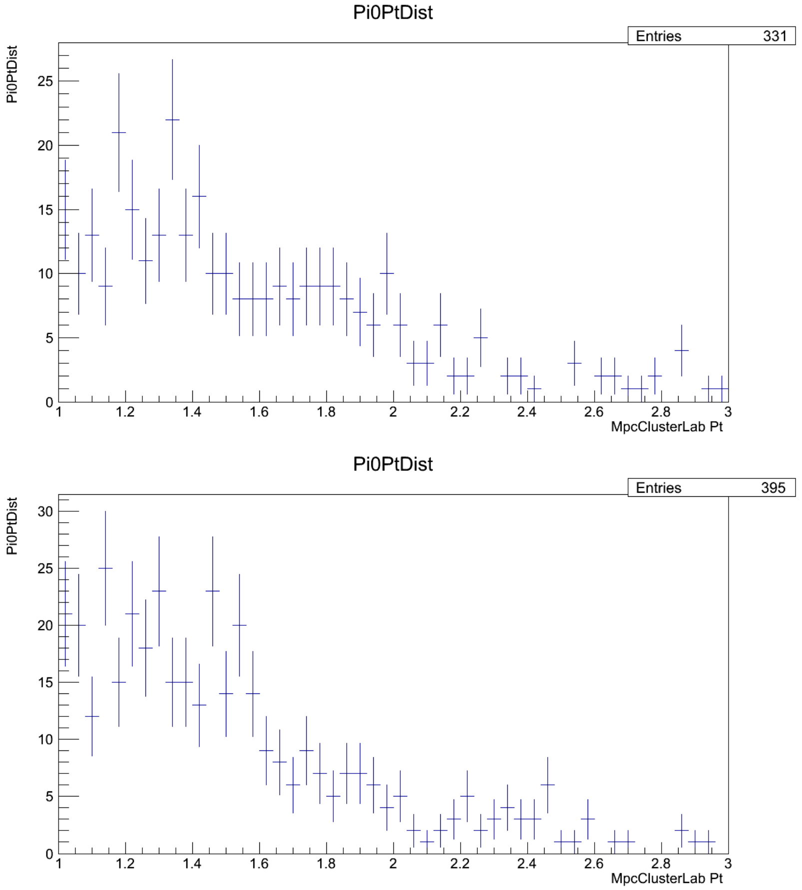

Figure 5.12 p_T distribution of real-data reconstructed MPC single-clusters (π^0s). Left: Jet in West arm, Right: Jet in East arm.

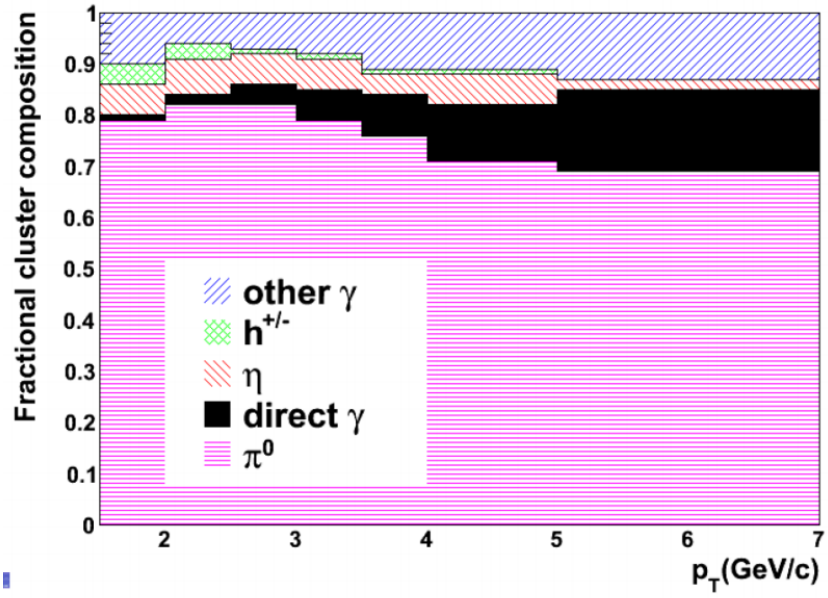

Figure 5.13 Simulation: The fractional composition of MPC reconstructed single-clusters [64].

5.5 Parton Kinematics

The requirement of a reconstructed jet in one of the central arms and a π^0 (electromagnetic cluster) in the North MPC detector biases the collision sub-process and both the initial-state and final-state parton kinematics. The sub-process fractions can be seen in Figure 5.14 (from the simulation described in Chapter 6). A clear bias toward $quark + gluon \rightarrow quark + gluon$ scattering can be seen.

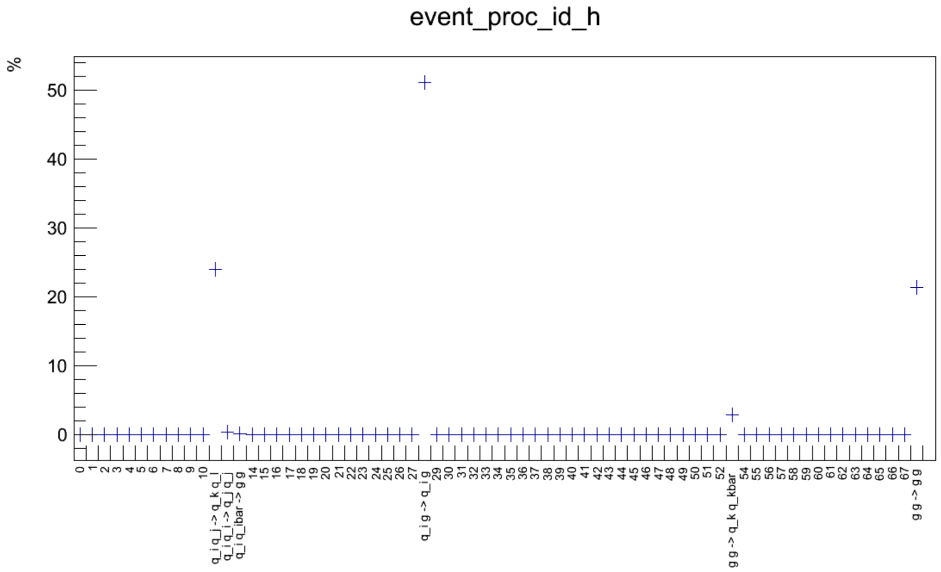

Figure 5.14 The fraction of 2→2 events from each subprocess. Notable contributions above the 2% level from left to right: *quark+quark→quark+quark*, *quark+gluon→quark+gluon*, *gluon+gluon→quark+anti−quark*, and *gluon+gluon→gluon+gluon*.

Since we require a 5 GeV reconstructed jet p_T in the lab-frame this preferentially biases the initial-state k_T such that the collision system has a net-k_T in the direction of the reconstructed jet. If there is zero initial-state partonic k_T (i.e. the transverse scattering frame and lab frame are equal) the momentum of the final-state gluon headed towards the central arm must be at least 5 GeV in p_T to fragment into an accepted reconstructed jet. However, if the net initial-state gluon's k_T is 1.0 GeV in the direction of the jet (i.e. the transverse scattering frame is moving relative to the lab frame) then only a 4.0 GeV p_T gluon (in the scattering frame) is required to produce a 5.0 GeV p_T gluon in the lab frame. This effect can be seen in Figure 5.15. It is important to note that the analysis method used here does not use initial-state partonic information directly, it only uses final-state information and avoids many of the ambiguities associated with modeling partonic initial states.

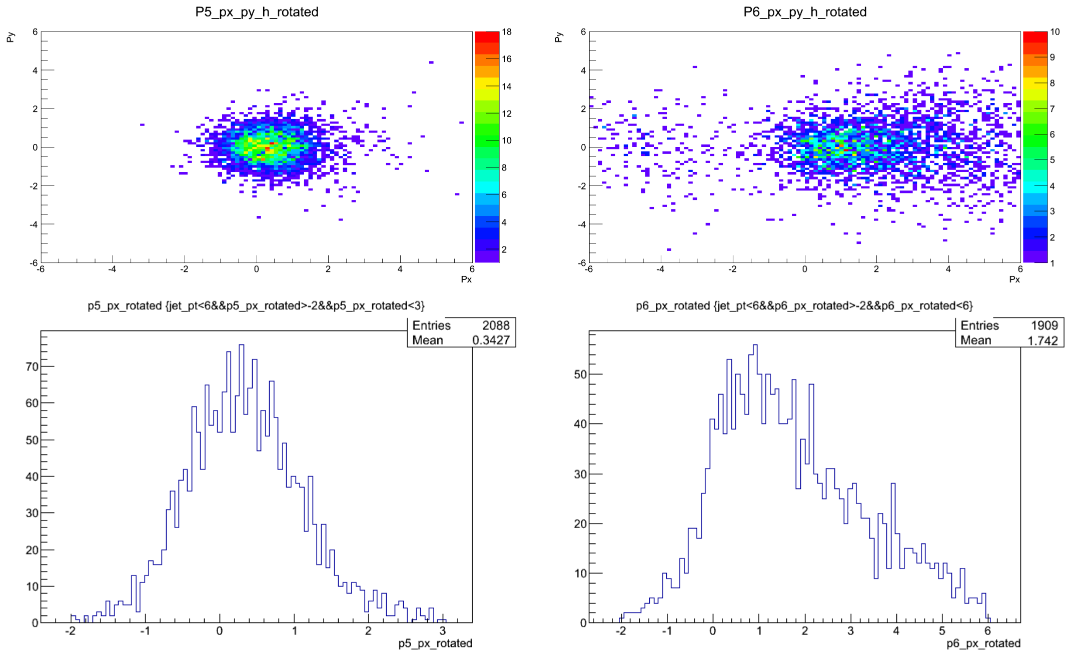

Figure 5.15 Plots showing the initial-state k_T biases due to final-state kinematic requirements. Left: final-state quark, Right: final-state gluon. The positive x-axis in each plot is momentum in the direction of the final-state reconstructed jet. Top: The y-axis is the spatial y-axis relative to the x-axis. Bottom: A projection of the top histogram onto its X-axis, note the x-axis scale and range changes. The means of the distributions are shown.

In the context of $quark{+}gluon{\rightarrow}quark{+}gluon$ subprocesses we can further analyze the final state parton kinematics. The requirement of a central jet coupled with a North MPC cluster of various minimum p_T biases the final-state gluon and quark kinematics. The final-state quark's pseudorapidity for different minimum MPC cluster p_T can be see in Figure 5.16. Our signal events occur when the quark momentum vector is pointed roughly toward the North MPC detector ($\eta > 2.5$). To increase the signal-to-background for these events we require a minimum MPC π^0 p_T of $1.0\frac{GeV}{c}$.

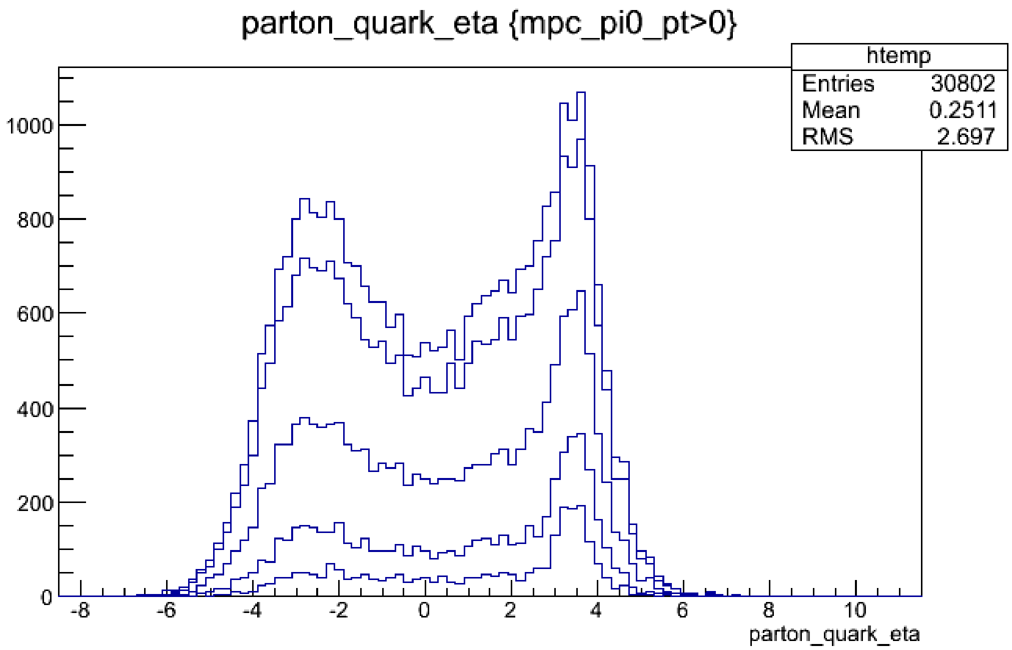

Figure 5.16 The distribution of final-state quark pseudorapidities in *quark* + *gluon* → *quark* + *gluon* subprocess events. The various curves each correspond to a different minimum MPC π^0 p_T. From top to bottom, the minimum $\pi^0 p_T$ cuts are: 0.0, 0.4, 0.6, 0.8, and 1.0 GeV.

CHAPTER 6. SIMULATIONS

Two main simulations were performed for this analysis. The Pythia [65] monte carlo program performed the entirety of sub-process interactions in each simulation performed. The PISA implimentation of the GEANT3 program performed the material interaction and detector response portions of the simulation.

6.1 Pythia

The Pythia monte carlo package performs event generation. Each piece of the simulation relies on either a comparison with experimental results (where possible) or reliance on QCD-based model results. The program is highly configurable. A set of tunes can then be performed to set various parameters to better match experimental observations in different energy regimes. A comparison of two leading tunes, “Tune A” [66] and “Perugia” [67], was performed at RHIC for the PHENIX FOCAL upgrade proposal [68]. The findings show that Tune A provides a better approximation of the reality seen at RHIC at forward rapidity. Further information on Tune A can be found in References [69] and [70].

The Pythia simulation provides both the initial state and final state event structure. Of which, of course, only the final state is verifiable at the moment. The initial state is, in part, adjusted such that it produces the correct (measurable) final state event kinematics and structure.

6.2 PISA

The PISA (PHENIX Integrated Simulation Application) package created by the PHENIX group provides a GEANT3 interface which performs the interactions between final-state Pythia particles and simulated materials and detectors. PISA itself has undergone rigorous tuning to best match the simulated and real detector responses. The output of the PISA package provides data in the same format as the real data itself, allowing for ease of comparison. The specific details of the implementation of GEANT3 can be found in Reference [49].

6.3 Event Selection and Generation

The selection of events from which our eventually needed parameterizations (Chapter 7) is derived are outlined here. Due to the extremely rare nature of the events required and the inability to heavily modify the initial and final-state partonic kinematics without biasing our result we require a set of final-state event kinematics to be met within each simulated event that is saved for analysis. Our set of signal events is defined such that we obtain a $quark + gluon \rightarrow quark + gluon$ scattering event where the final-state quark's momentum is roughly in the direction of the MPC detector (Section 3.3.8, $2.5 < \eta < 5.5$). Next, we require that a π^0 with a minimum p_T is found directed toward the MPC acceptance. Lastly, jet reconstruction is performed on the final-state particles that would have made it into the central arm acceptance and were able to be reconstructed by the central arm detectors. To that end, a fast-filter developed at Iowa State was used to quickly approximate the trajectory of charged particles through the magnetic field at PHENIX. A minimum $Anti{-}k_T$ reconstructed jet p_T of $5.0\ \frac{GeV}{c}$ and with a minimum of three constituent particles was required to save the event. A total of $3.2{*}10^{12}$ $quark + gluon \rightarrow quark + gluon$ sub-processes were generated from a total of roughly 3.2 million computing-hours (roughly three months using 1,500 CPUs concurrently and continuously). Of the generated events roughly one event per $7.5{*}10^{6}$ were saved for eventual analysis (a total of 424,221 events). After this stage the saved Pythia events were passed to the PISA simulation package with the Run-12 configuration. A final set of cuts requiring the reconstruction of an $Anti{-}k_T$ reconstructed jet as well as the π^0 kinematic cuts as placed on real data outlined in Chapters 4 and 5. This whittled the total simulated event sample down to 2,913 events.

CHAPTER 7. METHOD APPLIED

This chapter implicitly assumes that we have previously determined both the reconstructed jet momentum and the MPC π^0 momentum as discussed in Chapters 4 and 5. All figures in this chapter are from the simulation described in Chapter 6. The analysis method as described in previous sections relies heavily on using Lorentz transforms to boost into the transverse scattering frame (tSF) and center-of-momentum frame (CM). The three-dimensional lorentz transform can be see in Equation 7.1.

$$\begin{bmatrix} E' \\ p'_x \\ p'_y \\ p'_z \end{bmatrix} = \begin{bmatrix} \gamma & -\gamma\,\beta_x & -\gamma\,\beta_y & -\gamma\,\beta_z \\ -\gamma\,\beta_x & 1+(\gamma-1)\dfrac{\beta_x^2}{\beta^2} & (\gamma-1)\dfrac{\beta_x\beta_y}{\beta^2} & (\gamma-1)\dfrac{\beta_x\beta_z}{\beta^2} \\ -\gamma\,\beta_y & (\gamma-1)\dfrac{\beta_y\beta_x}{\beta^2} & 1+(\gamma-1)\dfrac{\beta_y^2}{\beta^2} & (\gamma-1)\dfrac{\beta_y\beta_z}{\beta^2} \\ -\gamma\,\beta_z & (\gamma-1)\dfrac{\beta_z\beta_x}{\beta^2} & (\gamma-1)\dfrac{\beta_z\beta_y}{\beta^2} & 1+(\gamma-1)\dfrac{\beta_z^2}{\beta^2} \end{bmatrix} \begin{bmatrix} E \\ p_x \\ p_y \\ p_z \end{bmatrix} \tag{7.1}$$

Where the variables used here are the following:

- $\overrightarrow{\beta} = \beta_x \cdot \hat{x} + \beta_y \cdot \hat{y} + \beta_z \cdot \hat{z}$
- $|\overrightarrow{\beta}| = \beta = \frac{v}{c}$
- v = velocity of one frame with respect to another
- $\gamma = \frac{1}{\sqrt{1-\beta^2}}$

It is important to note that the difference in pseudorapidity between two objects is invariant with respect to any Lorentz boost along the z-axis. For ease of explanation I will refer to the forward-going parton simply as the “quark” ($\overrightarrow{Q}$) and the central-going parton as the “gluon” ($\overrightarrow{G}$) throughout the next sections; a reasonable nomenclature as shown in Figure 5.14. Throughout these sections the statistical error on the mean of a distribution is defined as $\frac{1}{\sqrt{N}}$

unless specifically referenced to the "error of the mean" which is $\frac{\sigma}{\sqrt{N}}$ (where σ is the usual $\sqrt{variance}$ statistical property). This choice was made to avoid under-represented statistical errors due to low statistics in distributions which often have very small σ values (often due to the low statistics itself). Since many of the quantities here vary from plentiful statistics to low statistics, as a function of transverse momentum, a metric that could easily address both cases was chosen. This choice does not apply to the final result, the proper statistical error is calculated as shown in that section. Throughout the next sections I make heavy use of profile histograms. A profile histogram in our context displays the mean of the entries along the y-axis for each x-axis bin, the error bars on each bin are the aforementioned statistical errors.

7.1 Method Synopsis

This section is provided for reference when reading the next sections. A flow diagram of the analysis method is presented below for clarity (Figures 7.1 and 7.2). Each block represents an object (a 3-space vector), the lines and arrows represent information flow. The information can either be from a parameterization from simulation or from calculation. For example, going from $\overrightarrow{Jet}_{f,lab}$ to $\overrightarrow{G}_{f,lab}$ uses a parameterization ("P") that is obtained from simulation while $\overrightarrow{G}_{f,tSF}$ is obtained by an event-by-event calculation ("C") utilizing $\overrightarrow{G}_{f,lab}$ and $\overrightarrow{\beta}_{\perp}$. The nomenclature used here will be explain in subsequent sections.

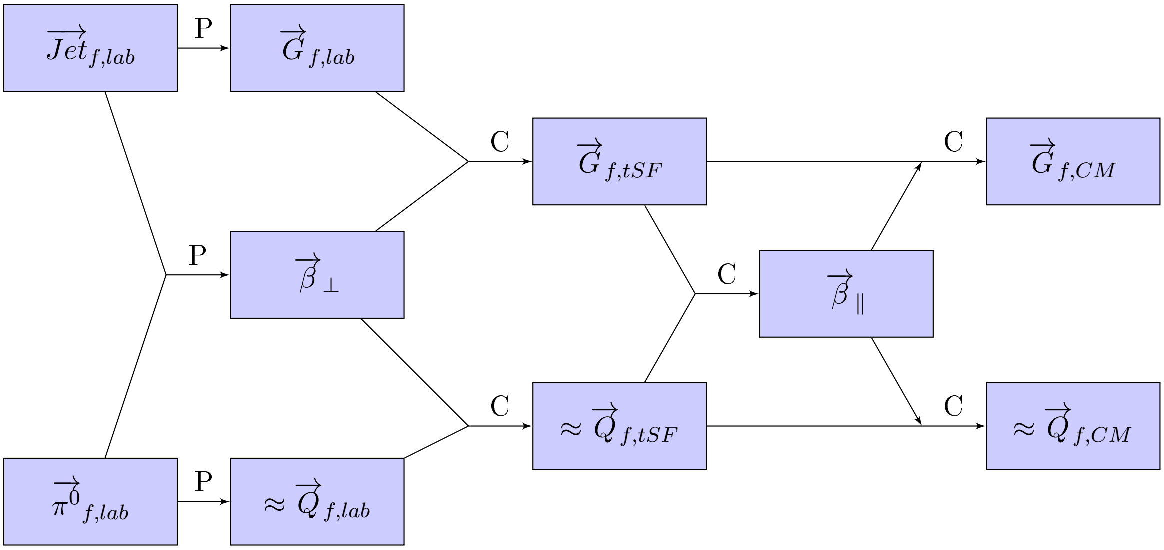

Figure 7.1 Flowchart of the analysis method. “C” = calculated step, “P” = simulation parameterized step.

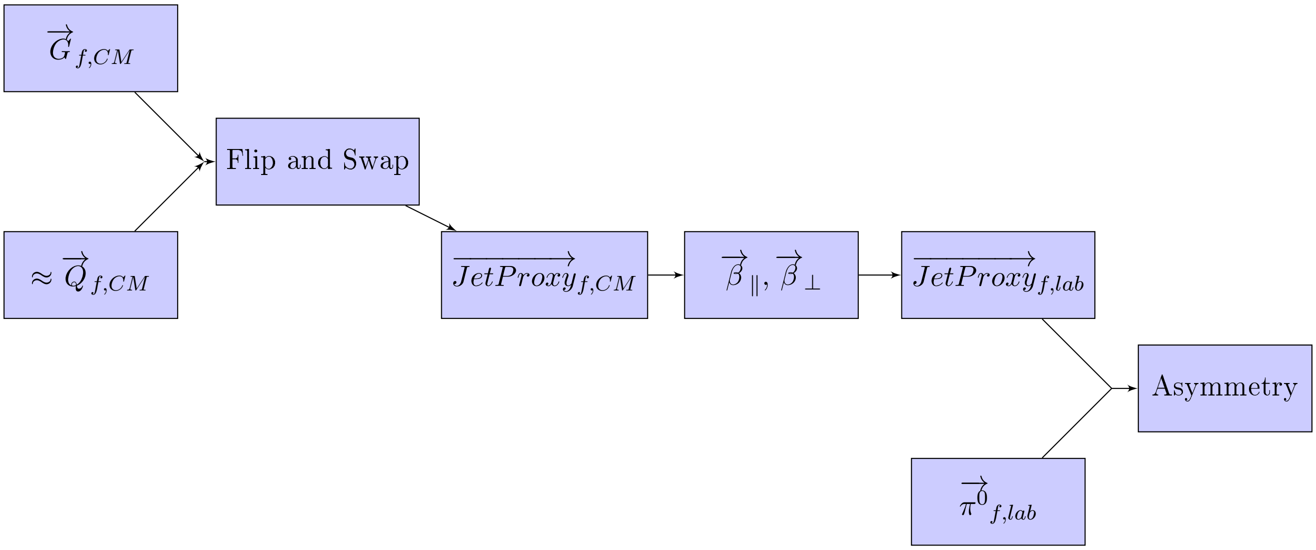

Figure 7.2 Flowchart of the analysis method. All steps are calculated steps (in reference to Figure 7.1 nomenclature).

A convenient coordinate system to work in is one where the reconstructed jet direction determines the transverse plane coordinates; to this end, each event is rotated in ϕ such that the $+\hat{x}$ direction is collinear with the transverse component of the reconstructed jet. For ease of reference, the equations which describe this coordinate system are shown below:

$$\hat{x} = \hat{Jet}_{f,lab}, \hat{z} = \hat{z}_{PHENIX} \tag{7.2}$$

where $\hat{z}_{PHENIX}$ is defined in Figure 4.1, but the system has been rotated in ϕ such that the $\hat{x}$ and $\hat{y}$ coordinate are no longer equal to the PHENIX coordinates. The $\hat{y}$ coordinate is, of course, still orthogonal to the x-z plane and satisfies $\hat{x} \times \hat{y} = \hat{z}$. Because of this choice of coordinate system the y-component of any vector is automatically perpendicular to the reconstructed lab frame jet momentum; this will be a useful tool in the next sections.

7.2 Lab Frame Final State Parton Approximation

The determination of $\overrightarrow{G}_{f,lab_\perp}$ is accomplished through the parameterization of $\overrightarrow{G}_{f,lab_x}$ (the y-component is necessarily zero, see Section 7.1 and Equation 7.2). Figure 7.3 shows the parameterization extracted from simulation. Similarly, $\overrightarrow{Q}_{f,lab_\perp}$ is obtained through parameterization of $\overrightarrow{Q}_{f,lab_x}$ and $\overrightarrow{Q}_{f,lab_y}$ in simulation (Figures 7.4 and 7.5). The parameterizations are used in the analysis according to Figure 7.1. Simply, for a measured $\overrightarrow{Jet}_{f,lab_x}$ ($\overrightarrow{\pi^0}_{f,lab_{x,y}}$) we determine $\overrightarrow{G}_{f,lab_\perp}$ ($\overrightarrow{Q}_{f,lab_{x,y}}$) through the parameterizations below. The ϕ-angle in the tranverse plane for the jet remains unchanged, however, the π^0 ϕ angle (relative to the central jet) is shifted due to the y-component of the parameterization, leading to an improved approximation of $\overrightarrow{Q}_{f,lab_\perp}$.

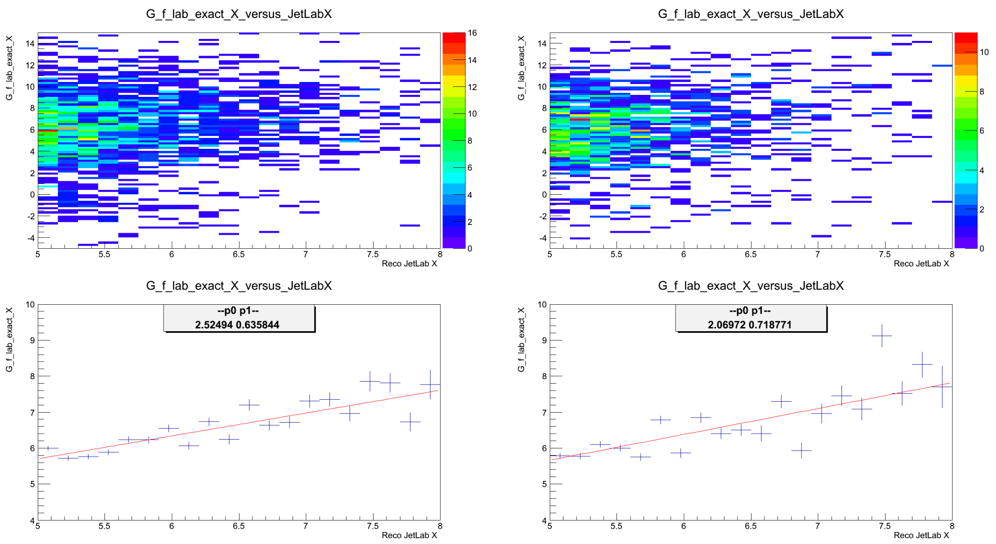

Figure 7.3 Top: Y-axis: $\overrightarrow{G}_{f,lab_x}$, X-axis: $\overrightarrow{Jet}_{f,lab_x}$. The bottom figures are profile histograms of top plots. The fit function takes the form: $p0 + p1 * x$, the extracted p0 and p1 parameters are shown on the plot. Left: Jet in West arm, Right: Jet in East arm.

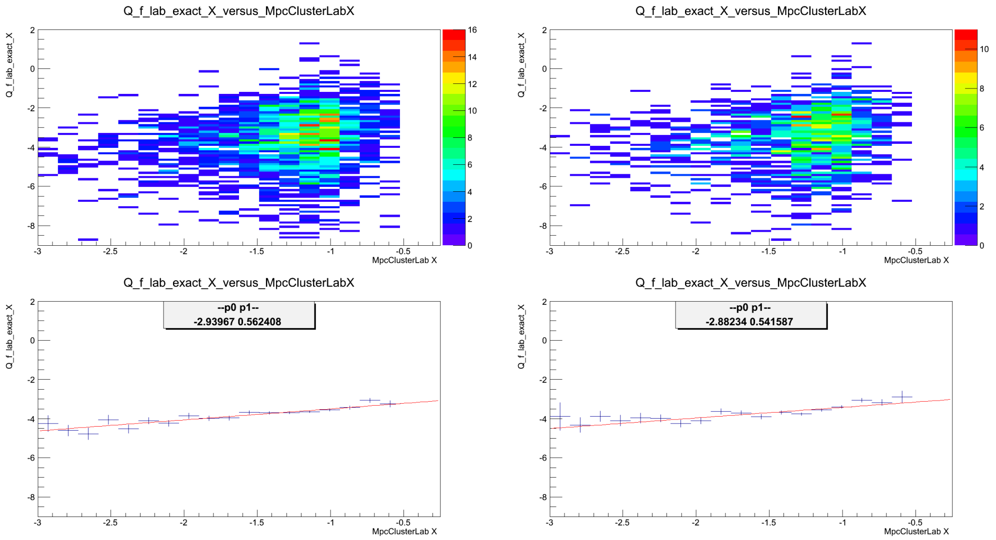

Figure 7.4 Top: Y-axis: $\overrightarrow{Q}_{f,lab_x}$, X-axis: $\overrightarrow{\pi^0}_{f,lab_x}$. The bottom figures are profile histograms of top plots. The fit function takes the form: $p0 + p1 * x$, the extracted p0 and p1 parameters are shown on the plot. Left: Jet in West arm, Right: Jet in East arm.

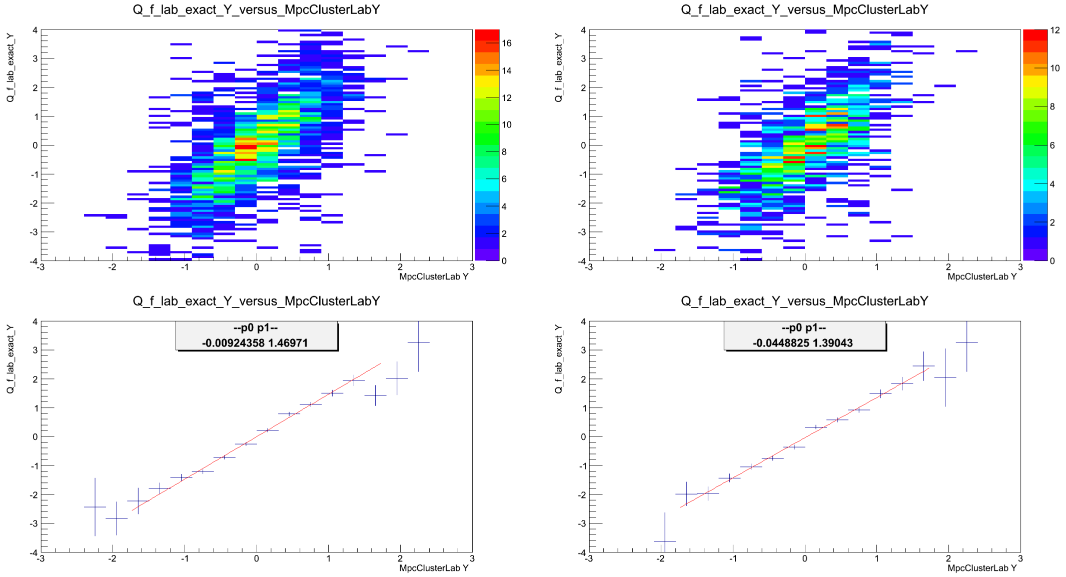

Figure 7.5 Top: Y-axis: $\overrightarrow{Q}_{f,lab_y}$, X-axis: $\overrightarrow{\pi^0}_{f,lab_y}$. The bottom figures are profile histograms of top plots. The fit function takes the form: $p0 + p1 * x$, the extracted p0 and p1 parameters are shown on the plot. Left: Jet in West arm, Right: Jet in East arm.

The direction of $\hat{G}_{f,lab}$ is simply set equal to $\hat{Jet}_{f,lab}$ (both in the transverse plane and the longitudinal), the distribution of $\Delta\eta$ values between our approximated $\hat{G}_{f,lab}$ and the true (simulation) value of $\hat{G}_{f,lab}$ is shown in Section 7.2.1. Due to the $\Delta\eta$ bias between $\overrightarrow{Q}_{f,lab}$ and $\overrightarrow{\pi^0}_{f,lab}$ shown in Figure 7.6 a p_T dependent correction is applied so that the η value of $\overrightarrow{Q}_{f,lab}$ is correct on an average basis (Section 7.2.1).

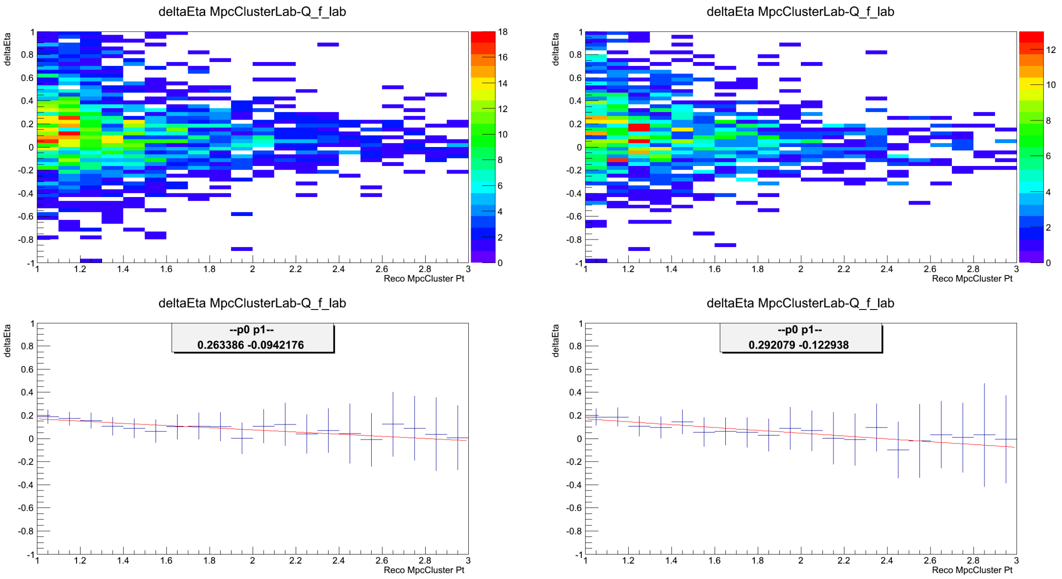

Figure 7.6 Simulation: The $\Delta\eta$ between the true $\overrightarrow{Q}_{f,lab}$ and the reconstructed $\overrightarrow{\pi^0}_{f,lab}$. X-axis is $|\overrightarrow{\pi^0}_{f,lab_\perp}|$, Y-axis is $\Delta\eta$. Left: Jet in West arm, Right: Jet in East arm. Top: 2D distribution, Bottom: Profile histogram of above.

7.2.1 Lab Frame Final State Parton Approximation - Quality Assurance

The parameterizations extracted from the simulation were then applied to the simulation data in the same manner in which they were applied to the real data. A series of checks were performed to determine if the method was able to reproduce the true $\overrightarrow{G}_{f,lab}$ and $\overrightarrow{Q}_{f,lab}$ using the parameterizations outlined in Section 7.2. The $\Delta\eta$ between the true parton and its approximation can be seen in Figures 7.7 and 7.8 for the gluon and quark respectively. Likewise, the $\Delta\phi$ between the true parton and its approximation can be seen in Figures 7.9 and 7.10 for the gluon and quark respectively. Of critical importance is the approximation of the average p_T of the central gluon and forward quark in the determination of the scattering frame (Section 7.3). The relative error ($\Delta p_T \equiv \frac{\overrightarrow{G,Q}_{f,lab_{approx}} - \overrightarrow{G,Q}_{f,lab_{true}}}{\overrightarrow{G,Q}_{f,lab_{true}}}$) in determining the p_T of our lab-frame partons is shown in Figures 7.11 and 7.12.

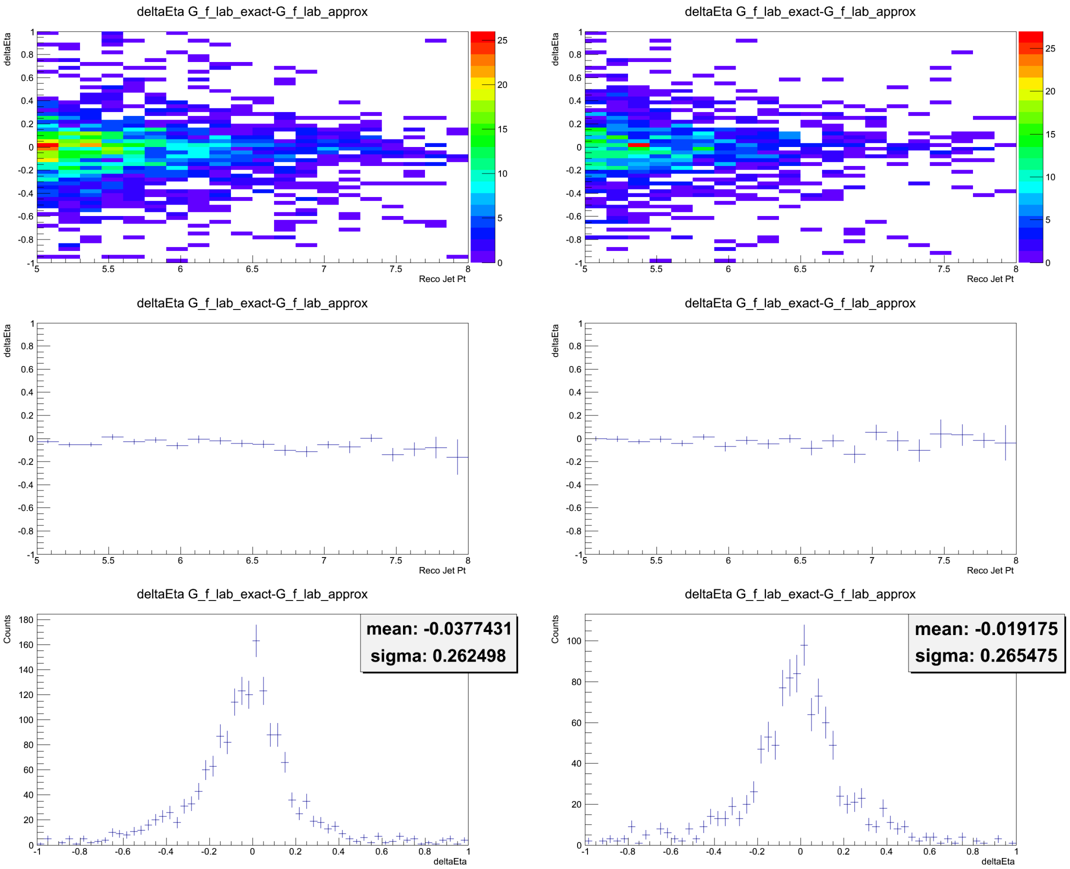

Figure 7.7 Top: The $\Delta\eta$ between the true $\overrightarrow{G}_{f,lab}$ and the approximated $\overrightarrow{G}_{f,lab}$. Middle: Profile histogram of above. Bottom: Projection onto the Y-axis of the top histograms. Left: Jet in West arm, Right: Jet in East arm.

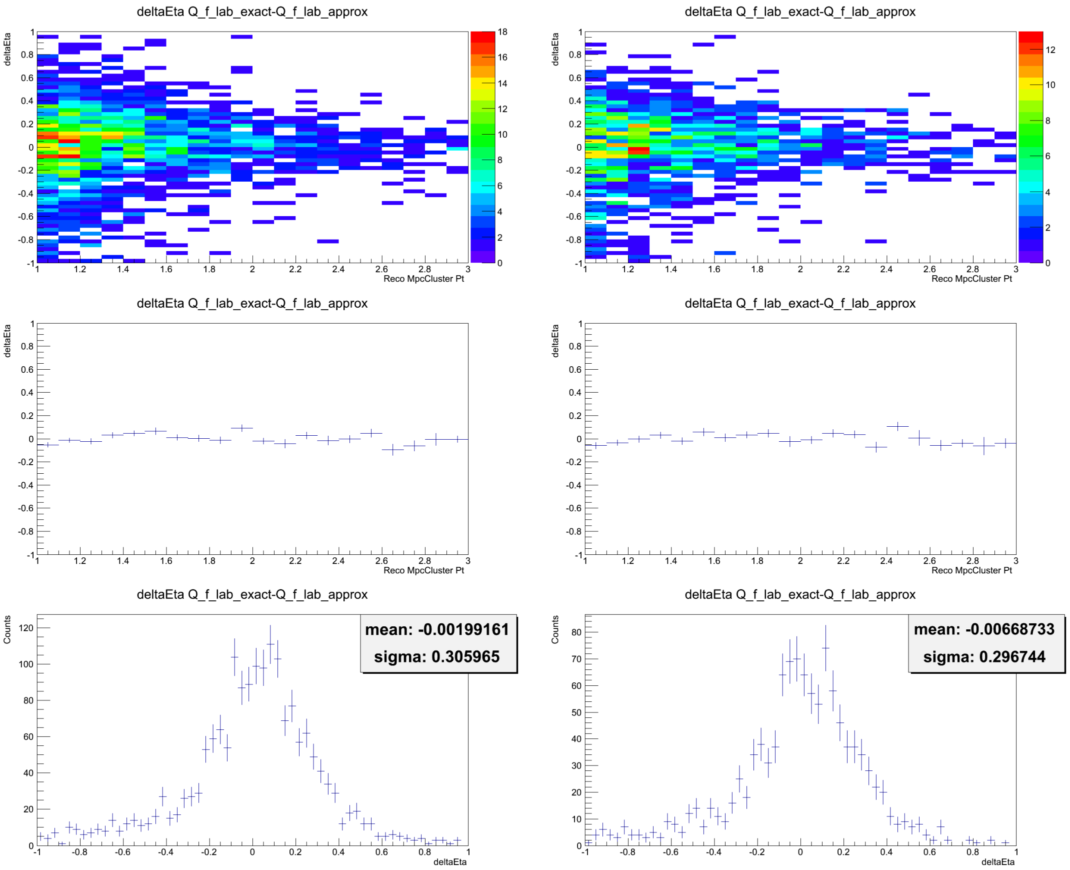

Figure 7.8 Top: The $\Delta\eta$ between the true $\overrightarrow{Q}_{f,lab}$ and the approximated $\overrightarrow{Q}_{f,lab}$. Middle: Profile histogram of above. Bottom: Projection onto the Y-axis of the top histograms. Left: Jet in West arm, Right: Jet in East arm.

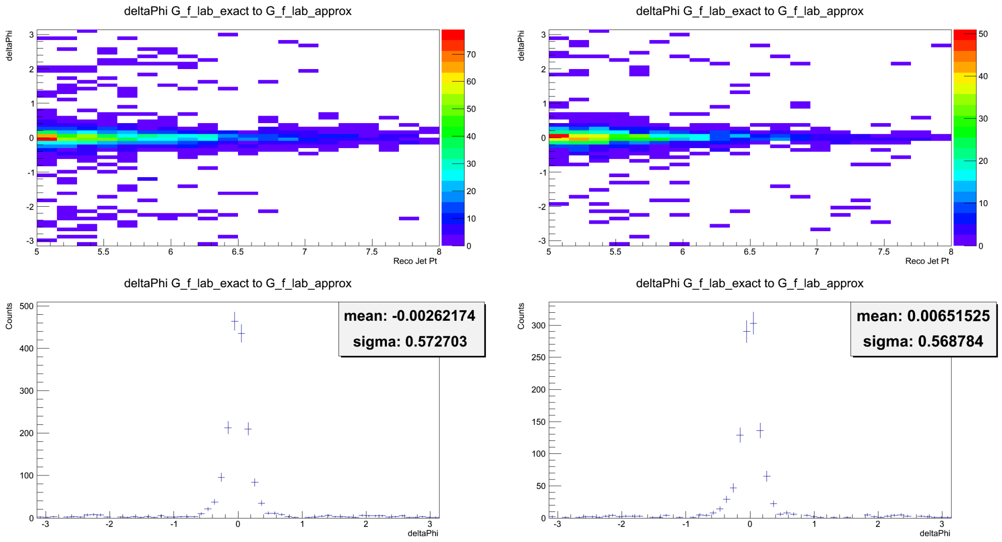

Figure 7.9 Top: The $\Delta\phi$ between the true and approximated $\overrightarrow{G}_{f,lab}$. Bottom: Projection onto the Y-axis. Left: Jet in West arm, Right: Jet in East arm.

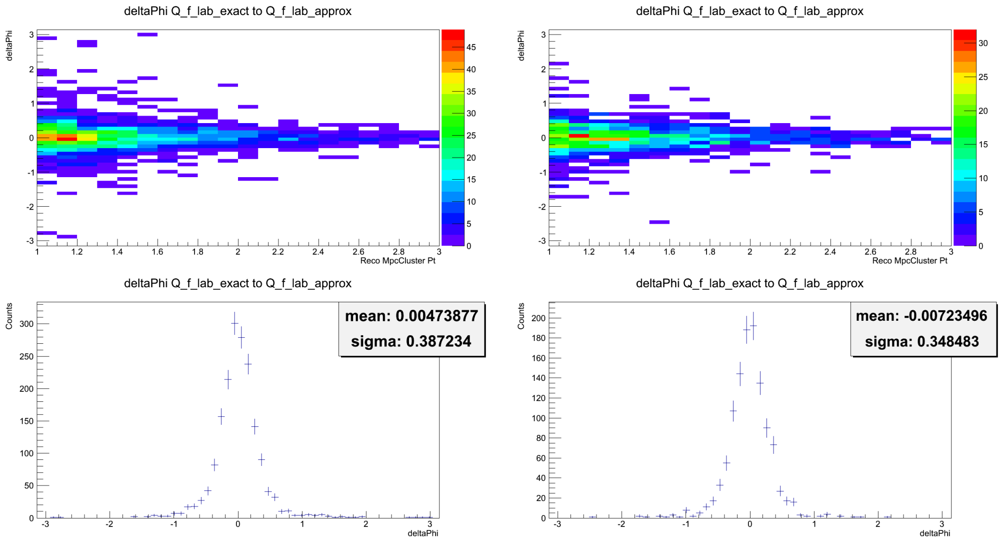

Figure 7.10 Top: The $\Delta\phi$ between the true and approximated $\overrightarrow{Q}_{f,lab}$. Bottom: Projection onto the Y-axis. Left: Jet in West arm, Right: Jet in East arm.

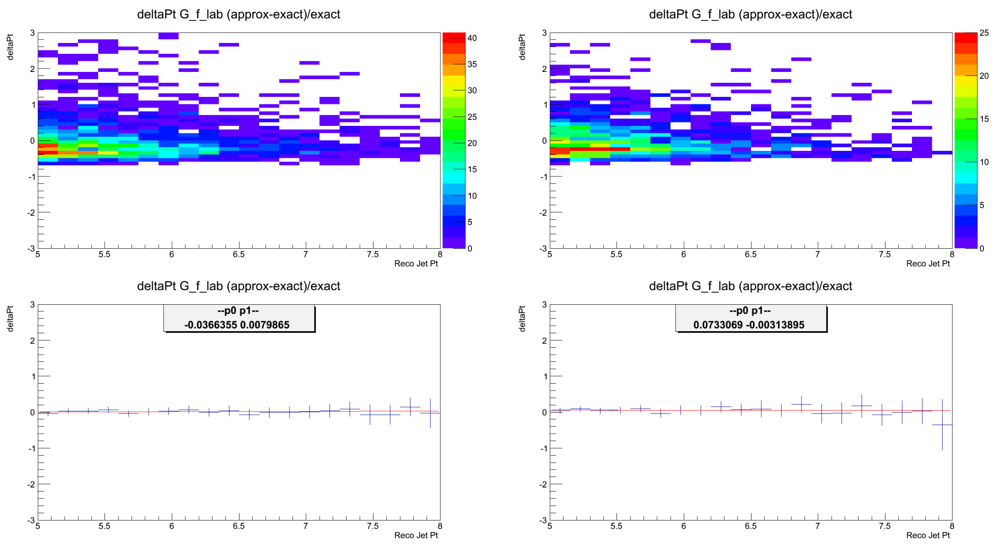

Figure 7.11 Top: The relative error in p_T between the true and approximated $\overrightarrow{G}_{f,lab}$. Y-axis: Δp_T, X-axis: $\overrightarrow{Jet}_{f,lab_{\perp}}$. Fit function: $p0 + p1 * x$. Bottom: Profile histogram of above. Left: Jet in West arm, Right: Jet in East arm.

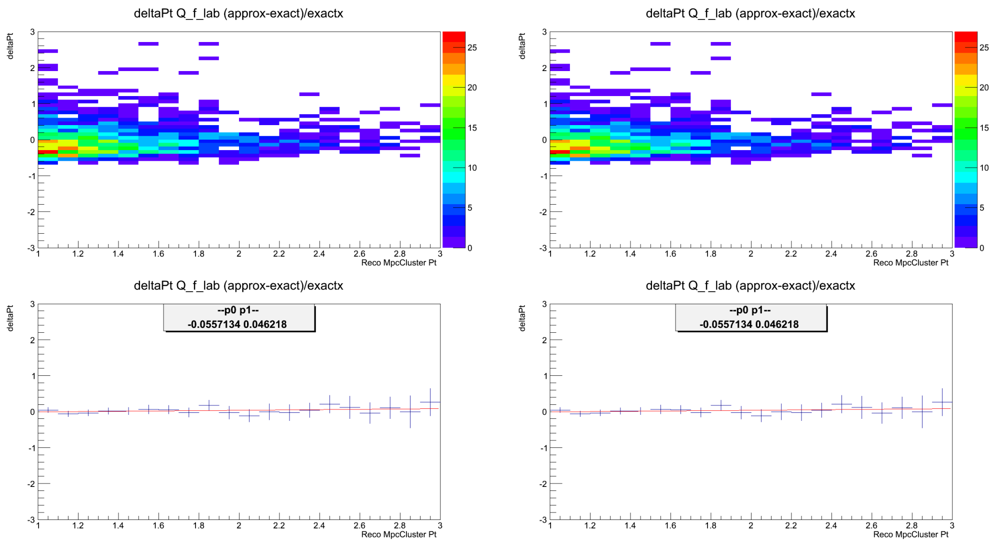

Figure 7.12 Top: The relative error in p_T between the true and approximated $\overrightarrow{Q}_{f,lab}$. Y-axis: Δp_T, X-axis: $\overrightarrow{\pi^0}_{f,lab_{\perp}}$. Bottom: Profile histogram of above. Fit function: $p0 + p1 * x$. Left: Jet in West arm, Right: Jet in East arm.

7.3 Transverse Scattering Frame

The transverse scattering frame (tSF) is defined such that $\overrightarrow{G}_{f,tSF_\perp} = -\overrightarrow{Q}_{f,tSF_\perp}$. A Lorentz boost is performed to translate from the lab frame into the tSF using the regular formulation of the Lorentz transform equation (Equation 7.1) with $\beta_z = 0$ which gives us Equation 7.3. The Lorentz boost into the tSF is thus defined by the $\overrightarrow{\beta}_\perp$ magnitude and direction (Equation 7.4). Our requirement that $\overrightarrow{G}_{f,tSF_\perp} = -\overrightarrow{Q}_{f,tSF_\perp}$ implies that the individual x and y components are also equal: $\overrightarrow{G}_{f,tSF_x} = -\overrightarrow{Q}_{f,tSF_x}$ and $\overrightarrow{G}_{f,tSF_y} = -\overrightarrow{Q}_{f,tSF_y}$. The usual high-energy approximation is made here such that $E \approx |\overrightarrow{p}|$. Using these requirements coupled with Equation 7.3 gives us the Equation 7.5.

$$\begin{bmatrix} E' \\ p'_x \\ p'_y \\ p'_z \end{bmatrix} = \begin{bmatrix} \gamma & -\gamma\beta_x & -\gamma\beta_y & 0 \\ -\gamma\beta_x & 1+(\gamma-1)\frac{\beta_x^2}{\beta^2} & (\gamma-1)\frac{\beta_x\beta_y}{\beta^2} & 0 \\ -\gamma\beta_y & (\gamma-1)\frac{\beta_y\beta_x}{\beta^2} & 1+(\gamma-1)\frac{\beta_y^2}{\beta^2} & 0 \\ 0 & 0 & 0 & 1 \end{bmatrix} \begin{bmatrix} E \\ p_x \\ p_y \\ p_z \end{bmatrix} \tag{7.3}$$

$$\overrightarrow{\beta}_\perp = \beta_x \cdot \hat{x} + \beta_y \cdot \hat{y} \tag{7.4}$$

$$\beta_x = \frac{\overrightarrow{G}_{f,lab_x} + \overrightarrow{Q}_{f,lab_x}}{|\overrightarrow{G}_{f,lab_\perp}| + |\overrightarrow{Q}_{f,lab_\perp}|}, \beta_y = \frac{\overrightarrow{G}_{f,lab_y} + \overrightarrow{Q}_{f,lab_y}}{|\overrightarrow{G}_{f,lab_\perp}| + |\overrightarrow{Q}_{f,lab_\perp}|} \tag{7.5}$$

The individual β_x and β_y components are each extracted from the simulation. The central jet momentum as well as the x-component of the MPC π^0 both contribute to the determination of the β_x component. Specifically, β_x is parameterized versus $\overrightarrow{Jet}_{f,lab_x} + \overrightarrow{\pi^0}_{f,lab_x}$ as shown in Figure 7.13. The MPC π^0 alone determines the β_y component (Figure 7.14), since the central jet has no y-component in our coordinate system, as explained in Section 7.1 and Equation 7.2. The parameterization here is seen in the method flowchart in Figure 7.1.

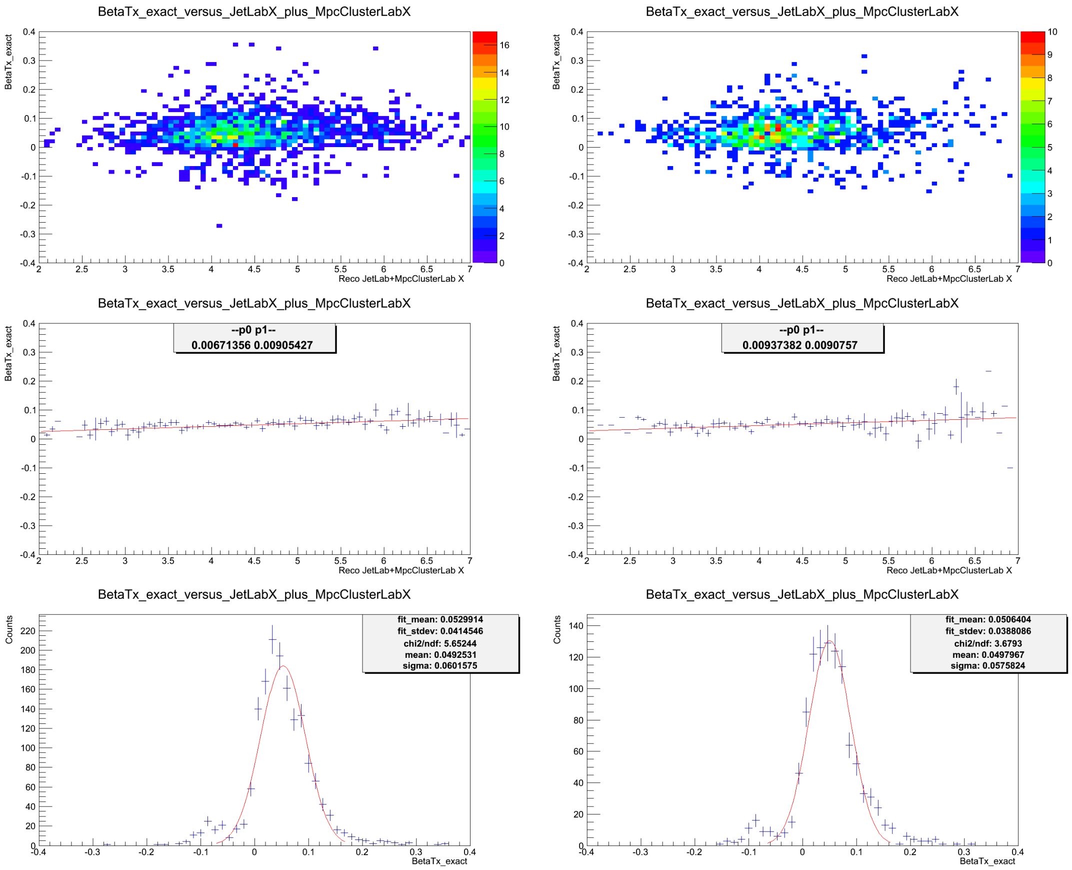

Figure 7.13 β_x as a function of $\overrightarrow{Jet}_{f,lab_x} + \overrightarrow{\pi^0}_{f,lab_x}$. Top: Two dimensional distribution. Middle: Profile of the above using "error of the mean" statistical errors ($\frac{\sigma}{\sqrt{N}}$). Bottom: Projection onto the Y-axis showing the mean is larger than zero. The fit function takes the form: $p0 + p1 * x$, the extracted p0 and p1 parameters are shown on the plot. Left: Jet in West arm, Right: Jet in East arm.

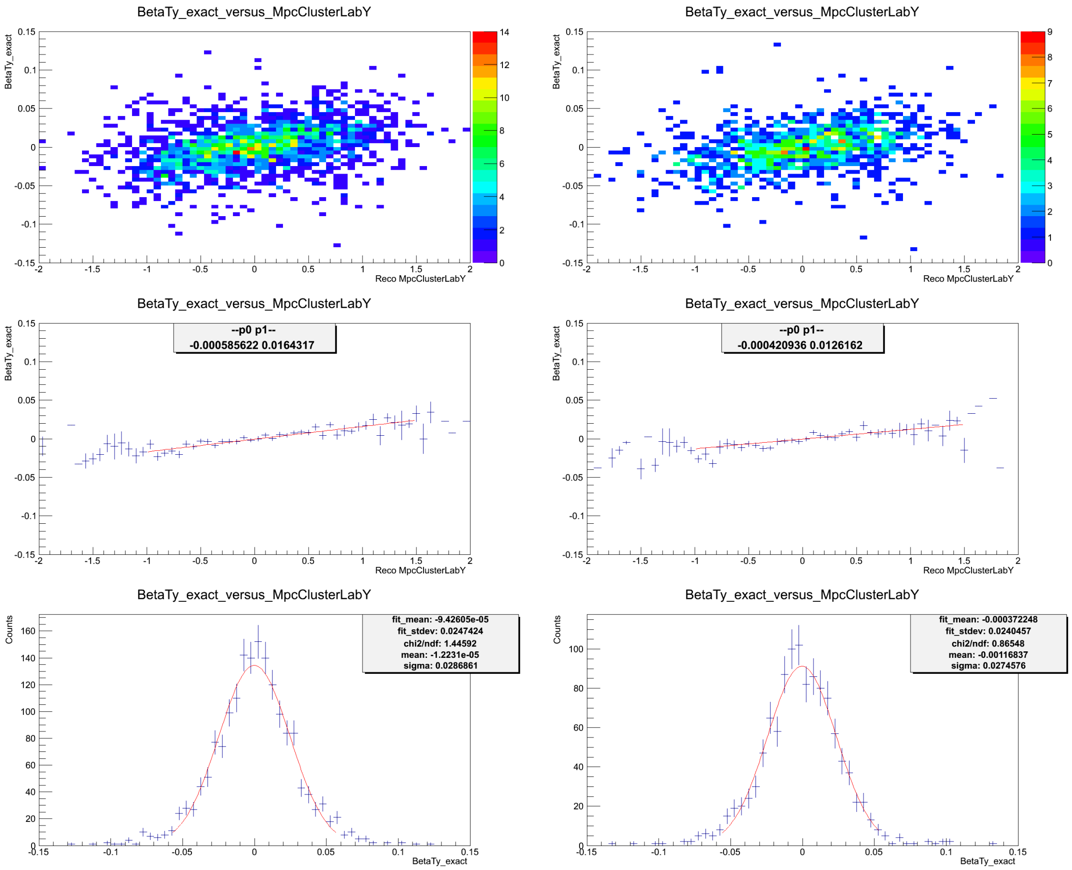

Figure 7.14 β_y as a function of $\vec{\pi^0}_{f,lab_y}$. Top: Two dimensional distribution. Middle: Profile of the above using "error of the mean" statistical errors ($\frac{\sigma}{\sqrt{N}}$). Bottom: Projection onto the Y-axis showing the mean is zero. The fit function takes the form: $p0 + p1 * x$, the extracted p0 and p1 parameters are shown on the plot. Left: Jet in West arm, Right: Jet in East arm.

The final-state quark ($\vec{Q}_{f,tSF_\perp}$) and gluon ($\vec{G}_{f,tSF_\perp}$) momentum vectors in the transverse scattering frame (tSF) need to be known or approximated for application in the "Boost, Flip, and Swap" procedure as described in Chapter 5. To obtain approximations for these vectors we turn to the $\vec{G}_{f,lab_\perp}$ and $\vec{Q}_{f,lab_\perp}$ obtained via the method in described in Section 7.2. Using the boost obtained from Section 7.3 on our $\vec{Q}_{f,lab}$ and $\vec{Q}_{f,lab}$ vectors via Equation 7.3 we obtain $\vec{Q}_{f,tSF}$ and $\vec{G}_{f,tSF}$.

7.3.1 Transverse Scattering Frame - Quality Assurance

Once again, checks were performed to determine the efficacy of the procedure in determining the tSF and the objects within the tSF. The checks are similar to the ones performed in Section 7.2.1. The $\Delta\eta$, $\Delta\phi$, and Δp_T between the approximate parton in the tSF and the true (simulation) parton in the tSF were all investigated. The $\Delta\eta$ checks can be seen in Figures 7.15 and 7.16, $\Delta\phi$ checks can be seen in Figures 7.17 and 7.18, and the Δp_T checks can be seen in Figures 7.19 and 7.20.

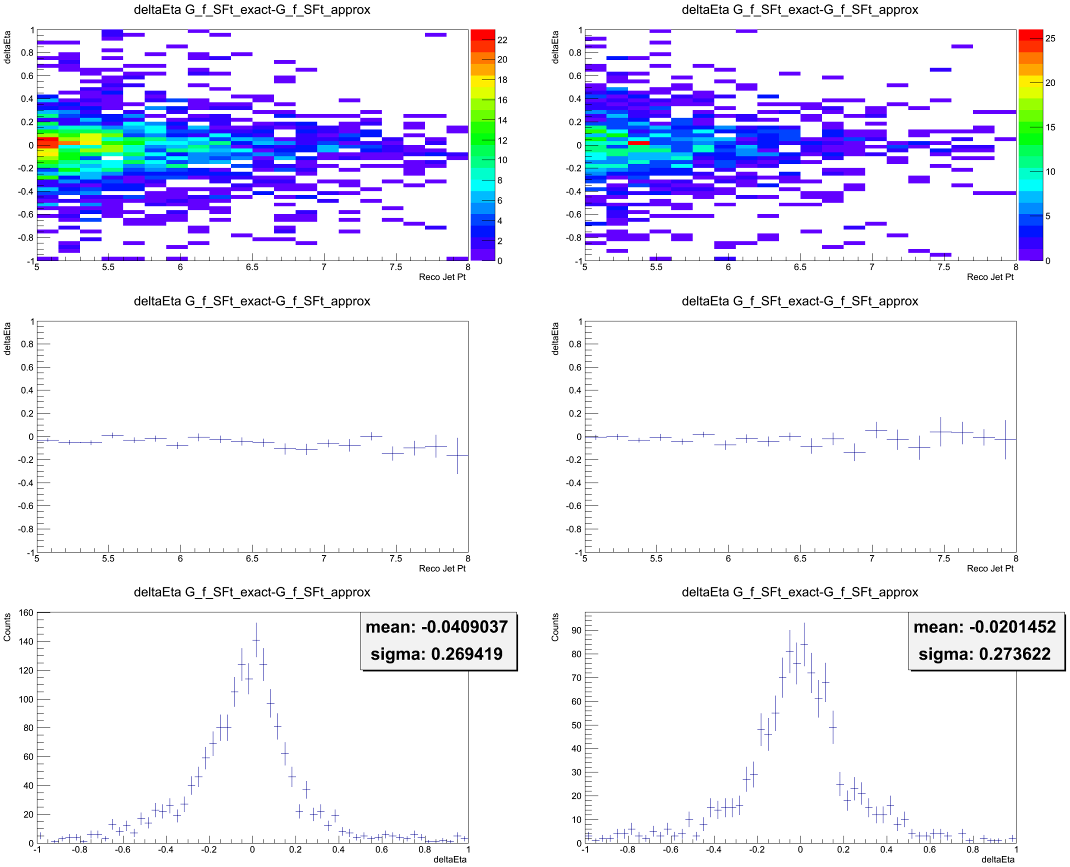

Figure 7.15 Top: The $\Delta\eta$ between the true $\overrightarrow{G}_{f,tSF}$ and the approximated $\overrightarrow{G}_{f,tSF}$. Middle: Profile histogram of above. Bottom: Projection onto the Y-axis of the top histograms. Left: Jet in West arm, Right: Jet in East arm.

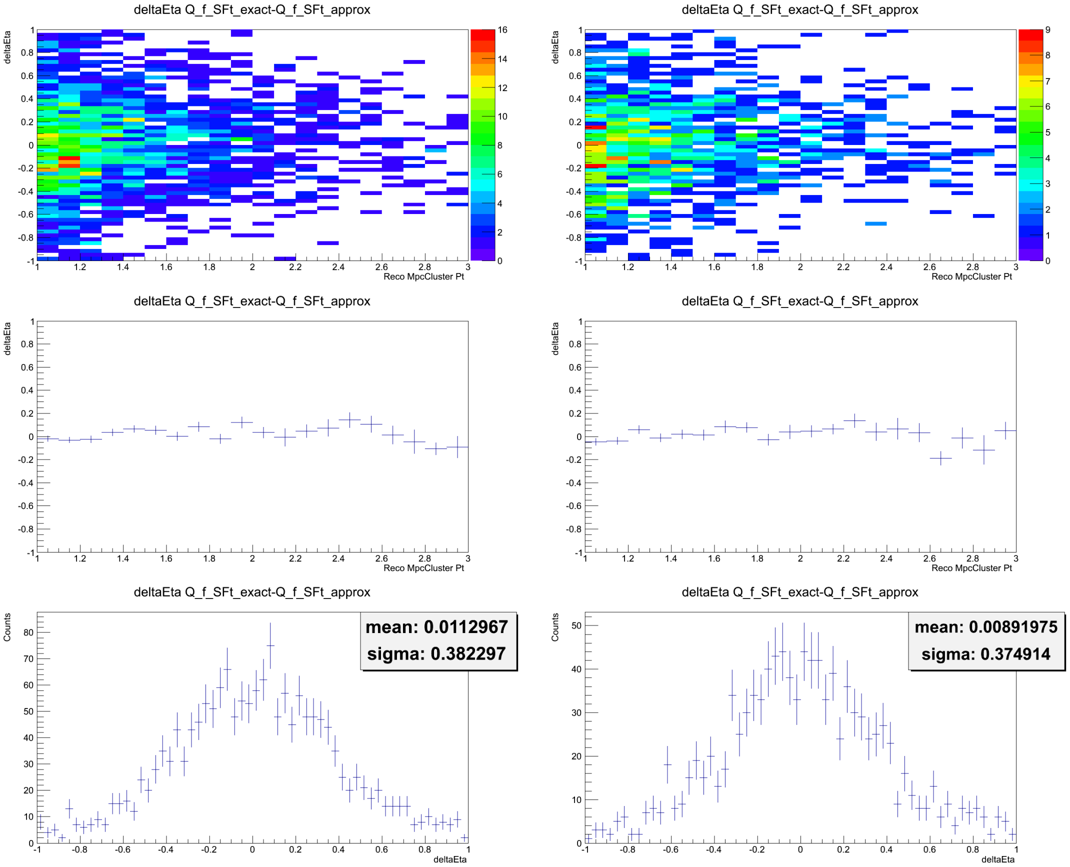

Figure 7.16 Top: The $\Delta\eta$ between the true $\overrightarrow{Q}_{f,tSF}$ and the approximated $\overrightarrow{Q}_{f,tSF}$. Middle: Profile histogram of above. Bottom: Projection onto the Y-axis of the top histograms. Left: Jet in West arm, Right: Jet in East arm.

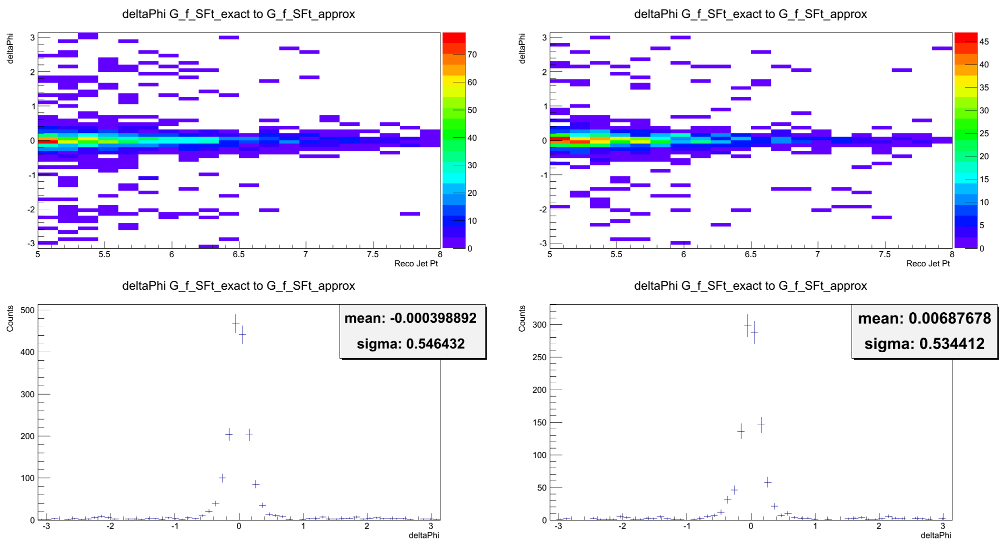

Figure 7.17 Top: The $\Delta\phi$ between the true $\overrightarrow{G}_{f,tSF}$ and the approximated $\overrightarrow{G}_{f,tSF}$. Bottom: Projection onto the Y-axis of the top histograms. Left: Jet in West arm, Right: Jet in East arm.

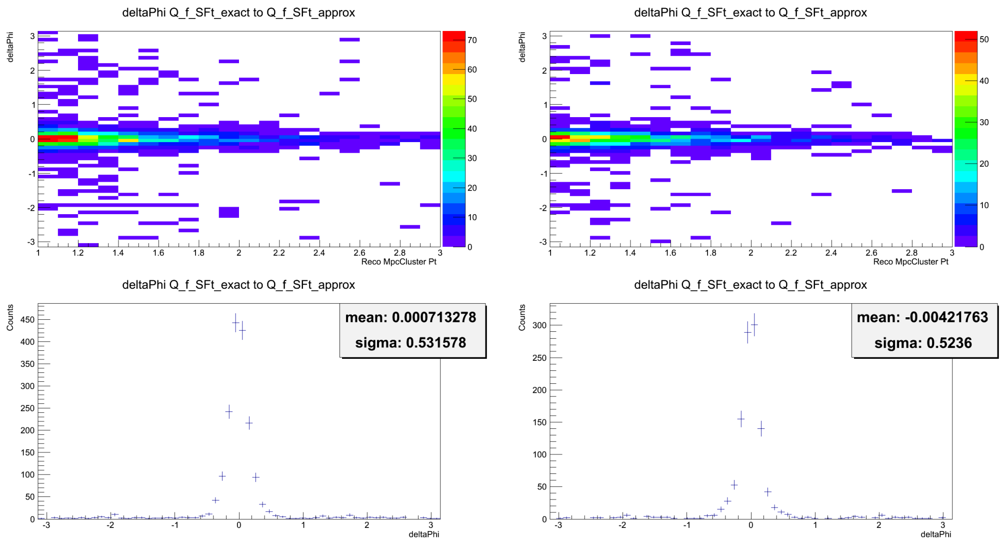

Figure 7.18 Top: The $\Delta\phi$ between the true $\overrightarrow{Q}_{f,tSF}$ and the approximated $\overrightarrow{Q}_{f,tSF}$. Bottom: Projection onto the Y-axis of the top histograms. Left: Jet in West arm, Right: Jet in East arm.

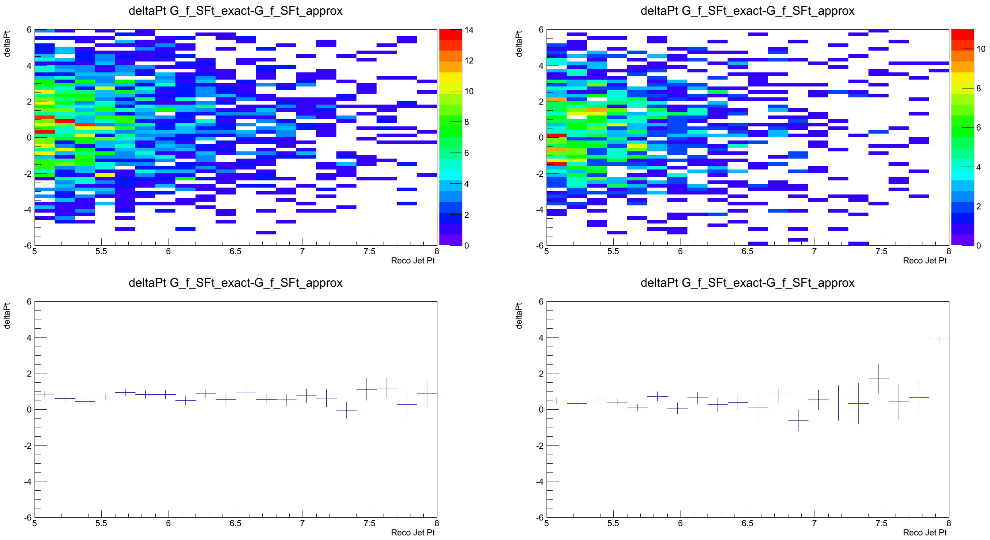

Figure 7.19 Top: The absolute Δp_T between the true and approximated $\overrightarrow{G}_{f,tSF}$. Y-axis: $\Delta p_T \equiv \overrightarrow{G}_{f,tSF_{true}} - \overrightarrow{G}_{f,tSF_{approx}}$, X-axis: $\overrightarrow{Jet}_{f,lab_\perp}$. Bottom: Profile histogram of above. Left: Jet in West arm, Right: Jet in East arm.

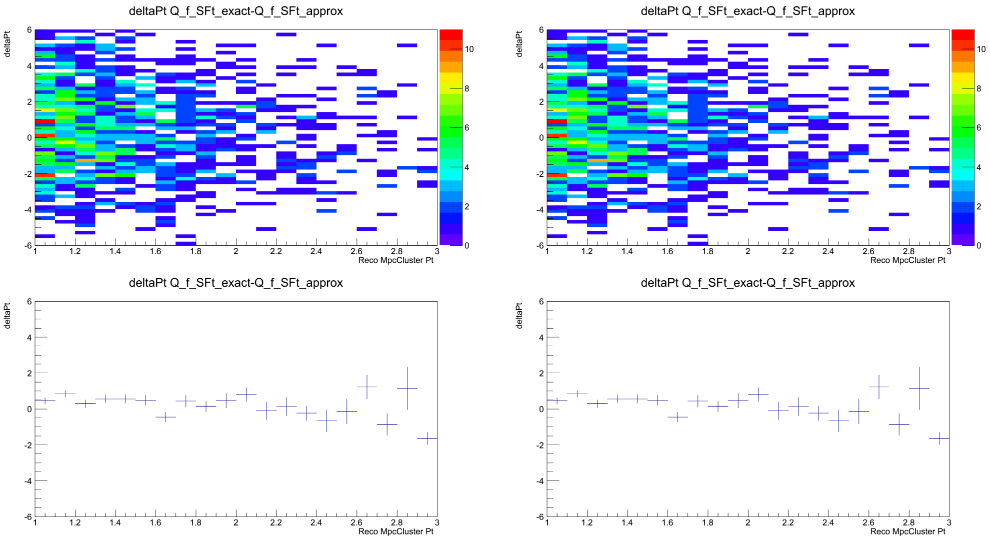

Figure 7.20 Top: The absolute Δp_T between the true and approximated $\overrightarrow{Q}_{f,tSF}$. Y-axis: $\Delta p_T \equiv \overrightarrow{Q}_{f,tSF_{true}} - \overrightarrow{Q}_{f,tSF_{approx}}$, X-axis: $\overrightarrow{\pi^0}_{f,lab_\perp}$. Bottom: Profile histogram of above. Left: Jet in West arm, Right: Jet in East arm.

7.3.2 Transverse Scattering Frame - Momentum Conservation

As discussed in Sections 5.1 and 7.3, we take it as a precept that there exists a transverse scattering frame such that the quark and gluon momentum in the transverse plane are equal and opposite. Since we have now obtained (approximated) our $\overrightarrow{G}_{f,tSF}$ and $\overrightarrow{Q}_{f,tSF}$ objects we can determine if this precept still holds given our approximations and method. If the transverse scattering frame as been found we should be able to assert that $\overrightarrow{G}_{f,tSF_x} + \overrightarrow{Q}_{f,tSF_x} = 0$ and $\overrightarrow{G}_{f,tSF_y} + \overrightarrow{Q}_{f,tSF_y} = 0$. To that end, first we explore the quantities $\overrightarrow{G}_{f,tSF_x} + \overrightarrow{Q}_{f,tSF_x}$ and $\overrightarrow{G}_{f,tSF_y} + \overrightarrow{Q}_{f,tSF_y}$ using the true (simulation) values for $\overrightarrow{G}_{f,lab}$, $\overrightarrow{Q}_{f,lab}$, β_{T_x}, and β_{T_y} to obtain our objects in the tSF. Two-dimensional distributions are shown in Figure 7.21. Next, the same quantities are shown using our approximate quantities exactly as would be performed with real data (Figure 7.22).

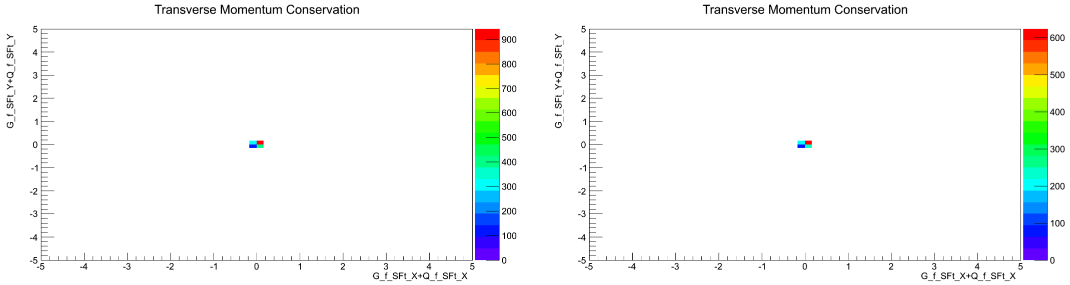

Figure 7.21 Distribution of momentum conservation quantities in the tSF using true (simulation) values for $\overrightarrow{G}_{f,lab}$, $\overrightarrow{Q}_{f,lab}$, β_{T_x}, and β_{T_y}. Y-axis: $\overrightarrow{G}_{f,tSF_y} + \overrightarrow{Q}_{f,tSF_y}$, X-axis: $\overrightarrow{G}_{f,tSF_x} + \overrightarrow{Q}_{f,tSF_x}$. Left: Jet in West arm, Right: Jet in East arm.

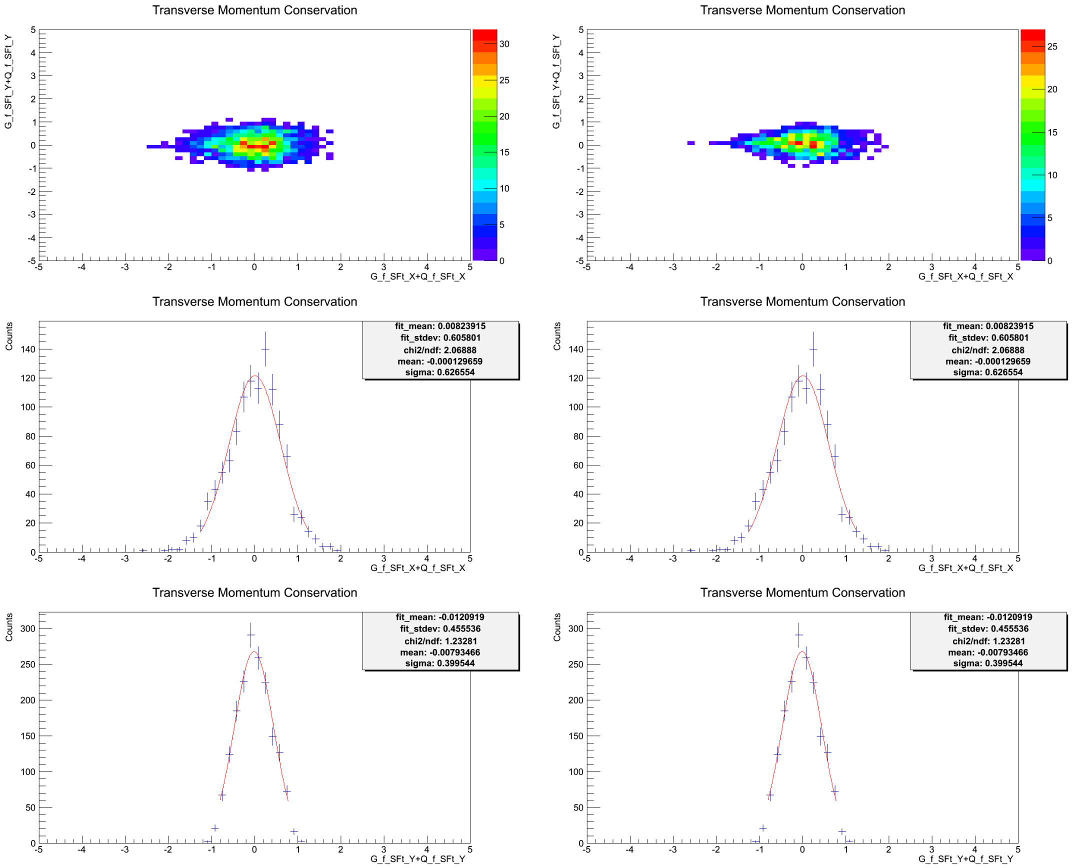

Figure 7.22 Top: Distribution of momentum conservation quantities in the tSF using our approximated $\overrightarrow{G}_{f,lab}$, $\overrightarrow{Q}_{f,lab}$, β_{Tx}, and β_{Ty}. Y-axis: $\overrightarrow{G}_{f,tSF_y} + \overrightarrow{Q}_{f,tSF_y}$, X-axis: $\overrightarrow{G}_{f,tSF_x} + \overrightarrow{Q}_{f,tSF_x}$. Middle: Projection of the top plots onto the x-axis. Bottom: Projection of the top plots onto the y-axis. Left: Jet in West arm, Right: Jet in East arm.

7.4 Boost, Flip, and Swap Applied

Throughout this section it is helpful for the reader to reference and follow along with the flow chart in Figure 7.2. Building off of our now known approximate $\overrightarrow{Q}_{f,tSF}$ and $\overrightarrow{G}_{f,tSF}$ momentum vectors we can perform the boost, flip, and swap procedure described in Chapter 5. Specifically, a Lorentz boost parallel to the z-direction (in the tSF frame) is performed to move from the transverse scattering frame into the center-of-momentum frame where $\overrightarrow{Q}_{f,CM} = -\overrightarrow{G}_{f,CM}$ in our 2→2 scattering model. Since the tSF has already satisfied the condition that the tranverse components of the quark and gluon momentum vectors are equal and opposite we only require a boost along the z-direction to make the 3-space vectors equal. The β_z value of the Lorentz boost is determined by Equation 7.6 which is derived from our $\overrightarrow{Q}_{f,CM} = -\overrightarrow{G}_{f,CM}$ constraint coupled with $\beta_x = 0$ and $\beta_y = 0$ in Equation 7.1.

$$\beta_z = \frac{\overrightarrow{G}_{f,tSF_z} + \overrightarrow{Q}_{f,tSF_z}}{|\overrightarrow{G}_{f,tSF}| + |\overrightarrow{Q}_{f,tSF}|} \tag{7.6}$$

An approximate β_z value is not derived from simulation, the β_z value used is always determined from our approximated $\overrightarrow{G}_{f,lab}$ and $\overrightarrow{Q}_{f,lab}$ momentum vectors on an event-by-event basis.

Once in the CM frame the “flip” portion of this analysis method is performed. Specifically, we create a new momentum vector called the “jet proxy” ($\overrightarrow{JProxy}_{f,CM}$) and set it equal to a “flipped” $\overrightarrow{G}_{f,CM}$ which can be seen in Equation 7.7.

$$\overrightarrow{JProxy}_{f,CM} = -\overrightarrow{G}_{f,CM} \tag{7.7}$$

Once the jet proxy is determined in the CM frame we reverse our previous boost from the tSF frame to the CM frame by setting $\beta_z \to -\beta_z$ which effectively undoes the boost, allowing us to obtain $\overrightarrow{JProxy}_{f,tSF}$. From there, the β_T boost is undone, allowing us to obtain $\overrightarrow{JProxy}_{f,lab}$.

Once the jet proxy vector is known in the lab frame we have all of the required information to approximate the final-state quark momentum vector direction. We now apply the “swap” portion of the analysis method, which is to swap the unknown $\overrightarrow{Q}_{f,lab}$ for our $\overrightarrow{JProxy}_{f,lab}$ that was determined from the previous sections.

To determine if our $\overrightarrow{JProxy}_{f,lab}$ is a good approximation of $\overrightarrow{Q}_{f,lab}$ we show the $\Delta\eta$ between our true $\overrightarrow{Q}_{f,lab}$ in simulation with our $\overrightarrow{JProxy}_{f,lab}$ derived from the analysis method. Figures 7.23 and 7.24 show the $\Delta\eta$ between $\overrightarrow{Q}_{f,lab}$ and $\overrightarrow{JProxy}_{f,lab}$ in the simulation if we do not use any approximations for $\overrightarrow{G}_{f,lab}$ or $\overrightarrow{Q}_{f,lab}$; basically, we assume we know the final-state parton kinematics and apply the method. One can see that the method produces a near-perfect jet proxy if all information is known. Using our approximately derived $\overrightarrow{JProxy}_{f,lab}$ we compare it to our known $\overrightarrow{Q}_{f,lab}$ in simulation and show the $\Delta\eta$ distribution in Figures 7.25 and 7.26. Finally, our approximate $\overrightarrow{JProxy}_{f,lab}$ is compared to the true $\overrightarrow{Q}_{f,lab}$ in ϕ (Figures 7.27 and 7.28), giving us a full 3-dimensional picture of the resolution of the method in simulation.

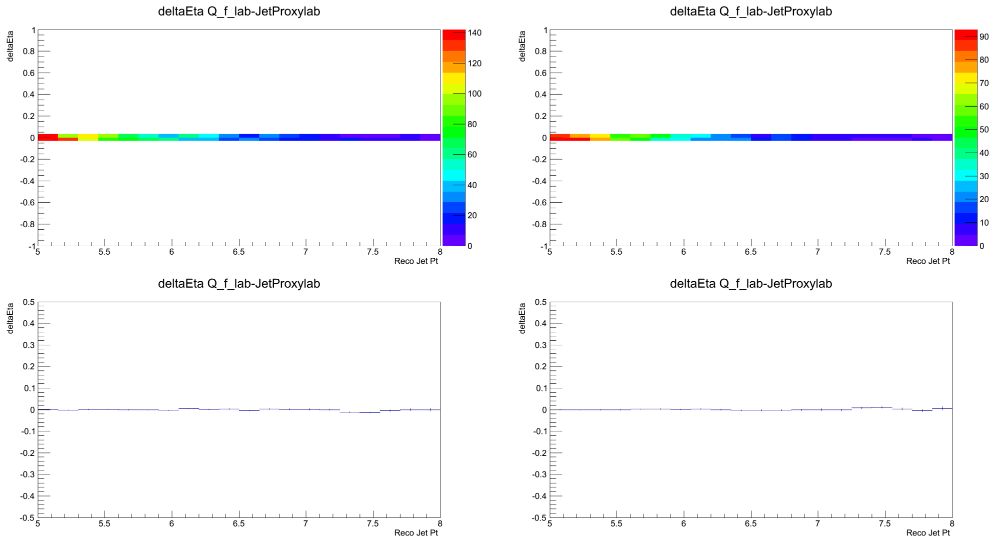

Figure 7.23 Using exact $\overrightarrow{JProxy}_{f,lab}$ and $\overrightarrow{Q}_{f,lab}$ vectors in simulation. Top: Y-axis: $\Delta\eta$ between the true $\overrightarrow{Q}_{f,lab}$ and $\overrightarrow{JProxy}_{f,lab}$. X-axis: $|\overrightarrow{Jet}_{f,lab_\perp}|$. The bottom figures are profile histograms of top plots. Left: Jet in West arm, Right: Jet in East arm.

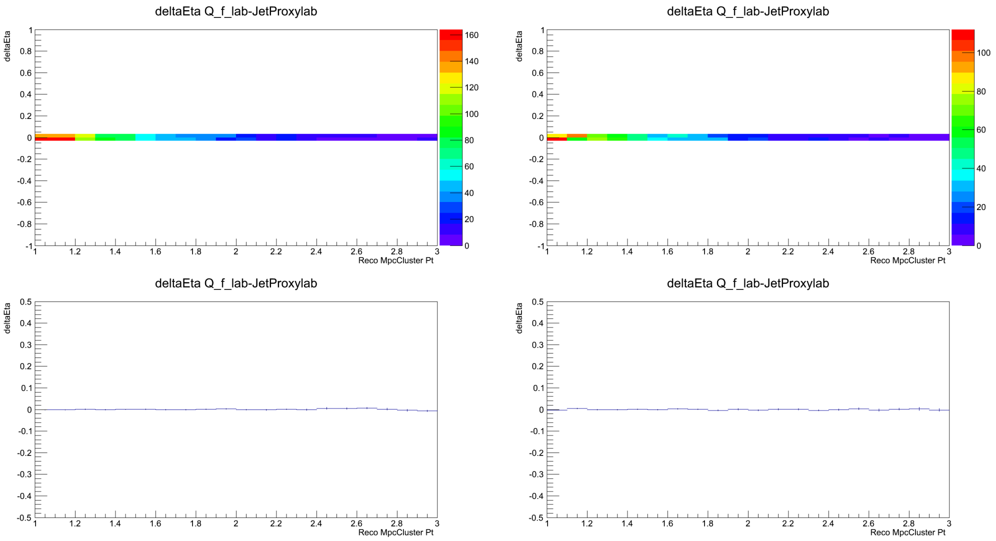

Figure 7.24 Using exact $\overrightarrow{JProxy}_{f,lab}$ and $\overrightarrow{Q}_{f,lab}$ vectors in simulation. Top: Y-axis: $\Delta\eta$ between the true $\overrightarrow{Q}_{f,lab}$ and $\overrightarrow{JProxy}_{f,lab}$. X-axis: $|\overrightarrow{\pi^0}_{f,lab_\perp}|$. The bottom figures are profile histograms of top plots. Left: Jet in West arm, Right: Jet in East arm.

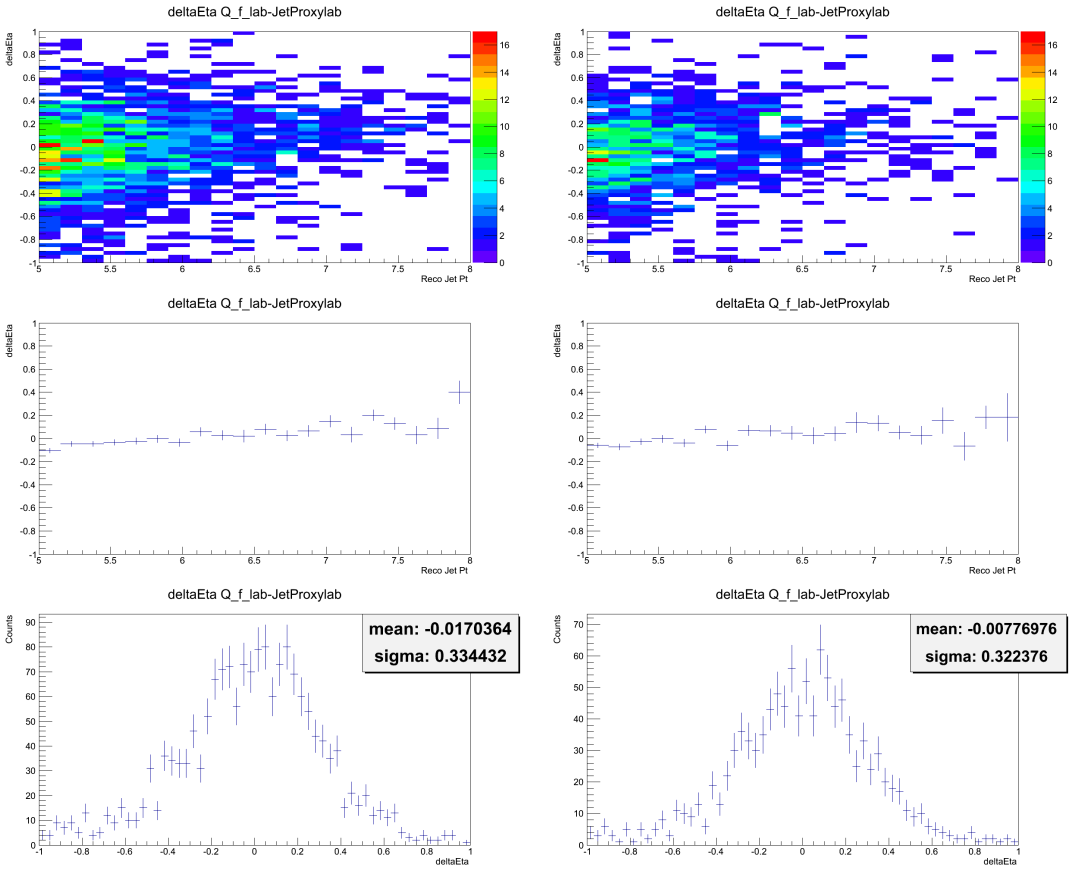

Figure 7.25 The $\Delta\eta$ between the approximated $\overrightarrow{JProxy}_{f,lab}$ and the true $\overrightarrow{Q}_{f,lab}$ vectors in simulation. Top: Y-axis: $\Delta\eta$. X-axis: $|\overrightarrow{Jet}_{f,lab_{\perp}}|$. Middle: Profile histogram of the top plots. Bottom: Projections of the top plots onto the Y-axis. Left: Jet in West arm, Right: Jet in East arm.

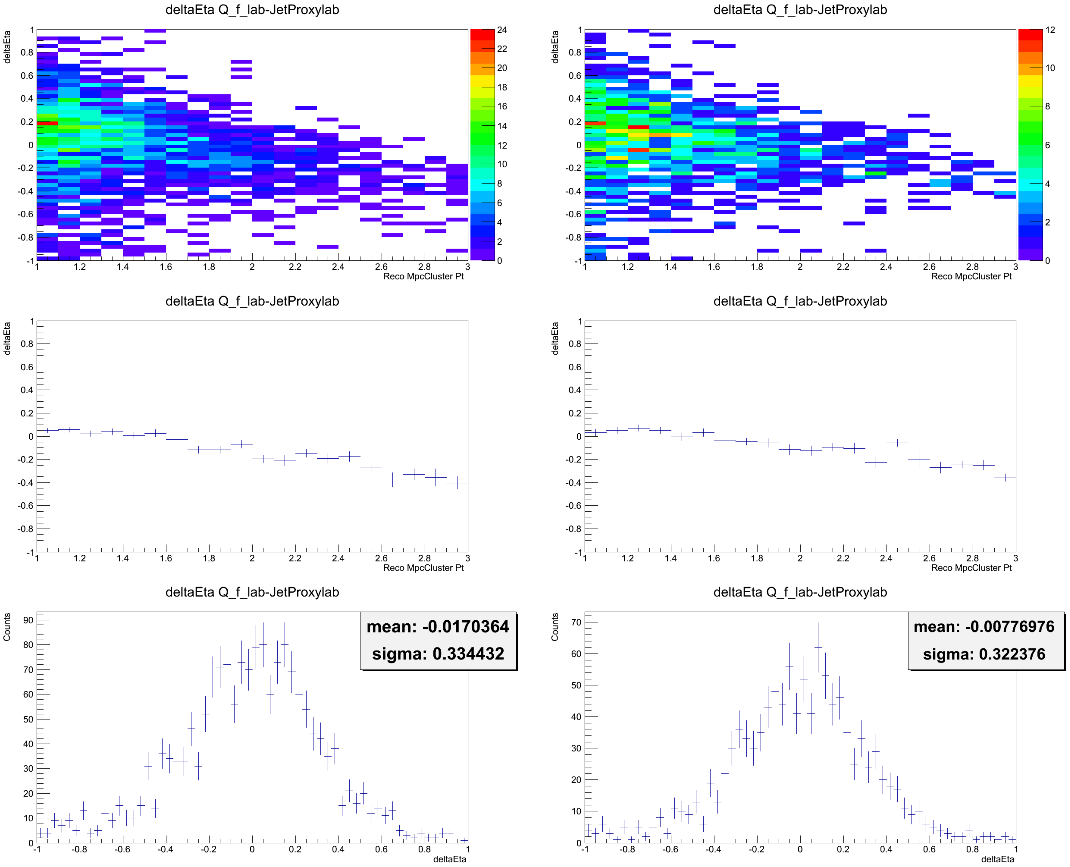

Figure 7.26 The $\Delta\eta$ between the approximated $\overrightarrow{JProxy}_{f,lab}$ and the true $\overrightarrow{Q}_{f,lab}$ vectors in simulation. Top: Y-axis: $\Delta\eta$. X-axis: $|\overrightarrow{\pi^0}_{f,lab_\perp}|$. Middle: Profile histogram of the top plots. Bottom: Projections of the top plots onto the Y-axis. Left: Jet in West arm, Right: Jet in East arm.

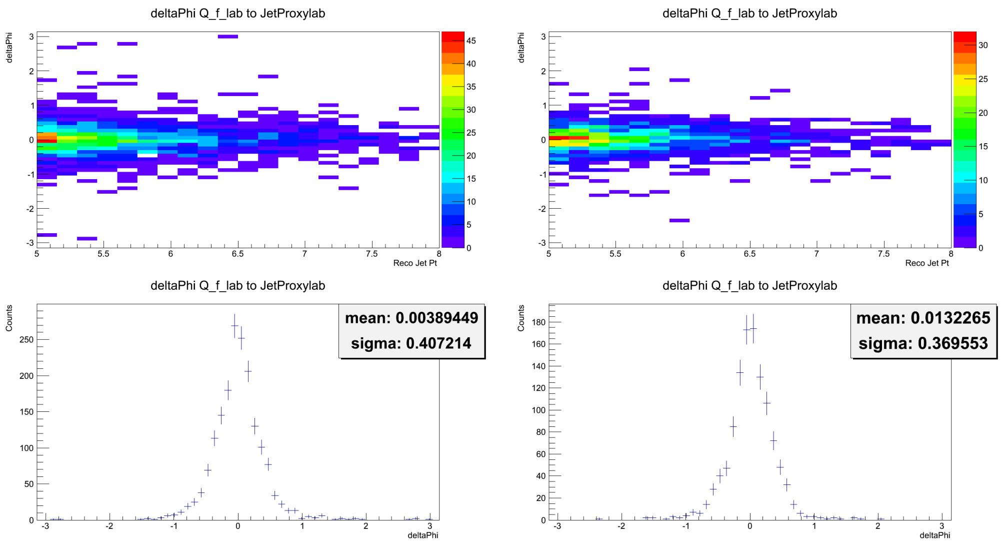

Figure 7.27 The $\Delta\phi$ between the approximated $\overrightarrow{JProxy}_{f,lab}$ and the true $\overrightarrow{Q}_{f,lab}$ vectors in simulation. Top: Y-axis: $\Delta\eta$. X-axis: $|\overrightarrow{Jet}_{f,lab_{\perp}}|$. Bottom: Projections of the top plots onto the Y-axis. Left: Jet in West arm, Right: Jet in East arm.

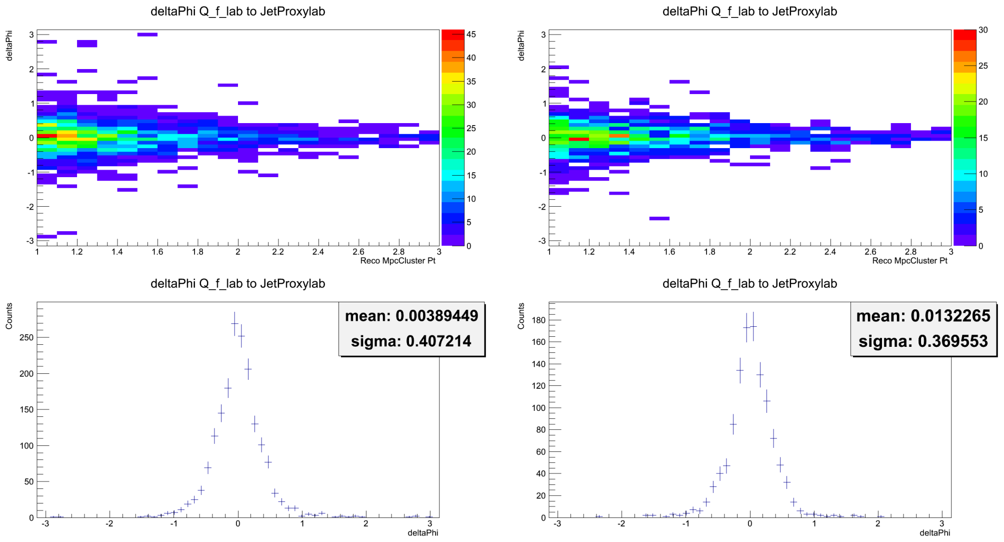

Figure 7.28 The $\Delta\phi$ between the approximated $\overrightarrow{JProxy}_{f,lab}$ and the true $\overrightarrow{Q}_{f,lab}$ vectors in simulation. Top: Y-axis: $\Delta\eta$. X-axis: $|\overrightarrow{\pi}^{0}{}_{f,lab_{\perp}}|$. Bottom: Projections of the top plots onto the Y-axis. Left: Jet in West arm, Right: Jet in East arm.

CHAPTER 8. RESULTS

We have now determined, from simulation, our needed parameterized corrections to perform the analysis on our real data. Namely, we required knowledge of the following:

- The average $\overrightarrow{\beta}_{\perp}$ as a function of our $\overrightarrow{Jet}_{f,lab_{\perp}}$ and $\overrightarrow{\pi^0}_{f,lab_{\perp}}$ momentum vectors.
- The average $\overrightarrow{G}_{f,lab}$ as a function of our $\overrightarrow{Jet}_{f,lab}$ properties.
- The average $\overrightarrow{Q}_{f,lab}$ as a function of our $\overrightarrow{\pi^0}_{f,lab}$ properties.

Each of these parameterized correction factors were explained in Chapter 7. Along with the parameterized corrections we also require events with well reconstructed jets and π^0s, the procedure to obtain these was explained in Chapters 4 and 5.

8.1 Final State Parton Approximations

The first step in applying the simulation parameterizations to the data is to approximate our $\overrightarrow{G}_{f,lab}$ and $\overrightarrow{Q}_{f,lab}$ vectors using the procedure discussed in Section 7.2. The p_T distributions of our approximate $\overrightarrow{G}_{f,lab}$ and approximate $\overrightarrow{Q}_{f,lab}$ can be seen in Figures 8.1 and 8.2 respectively. The counts in simulation are not normalized to the data's available statistics.

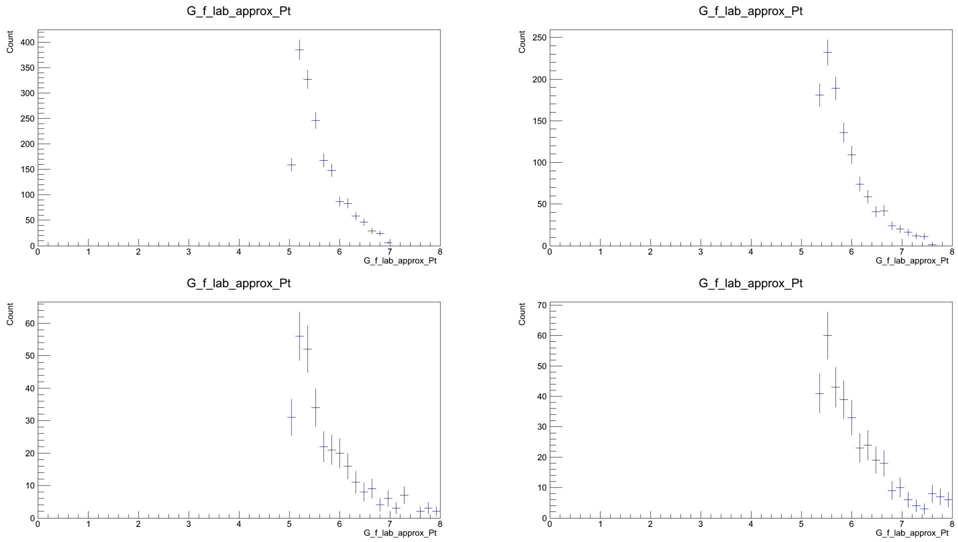

Figure 8.1 Comparison between simulation and real data approximated final-state lab-frame gluons. Y-axis: Counts, X-axis: $|\overrightarrow{G}_{f,lab_\perp}|$. Top: Simulated data, Bottom: Real data. Left: Jet in West arm, Right: Jet in East arm.

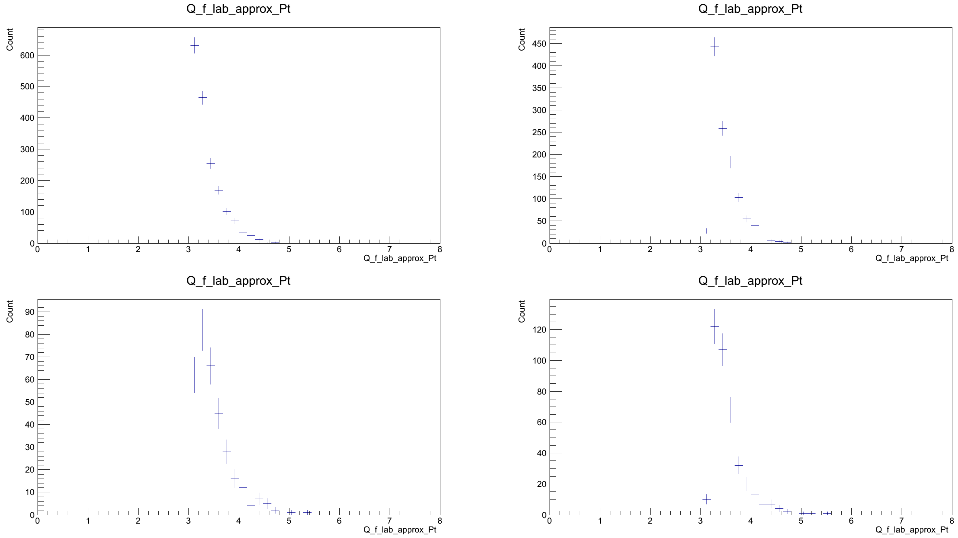

Figure 8.2 Comparison between simulation and real data approximated final-state lab-frame quarks. Y-axis: Counts, X-axis: $|\overrightarrow{Q}_{f,lab_\perp}|$. Top: Simulated data, Bottom: Real data. Left: Jet in West arm, Right: Jet in East arm.

8.1.1 Transverse Boost Parameter

The transverse boost parameter ($\overrightarrow{\beta}_{\perp}$) extracted from the simulation can be compared to the value in the real data calculated from our approximate $\overrightarrow{G}_{f,lab}$ and $\overrightarrow{Q}_{f,lab}$ obtained in the previous subsection. This procedure cannot be used on an event-by-event basis to circumvent the need for the $\overrightarrow{\beta}_{\perp}$ parameterization from the simulation as this would nullify any spin-dependence in the Δp_T between the $\overrightarrow{G}_{f,lab}$ and $\overrightarrow{Q}_{f,lab}$ objects (which ultimately contributes greatly to our asymmetry measurement). One could theoretically create a parameterization of $\overrightarrow{\beta}_{\perp}$ from the (spin-independent) real data and apply it to the data itself. The main reason this was not done is due to the low statistics of our real data sample the autocorrelation that would occur is very large, i.e. we do not have enough data to have a reasonable mix of both "up" and "down" spin components (relative luminosity normalized) to obtain a set of spin-independent parameters. The comparison between the $\overrightarrow{\beta}_{\perp}$ simulation and real-data parameters is shown in Figures 8.3 to 8.5.

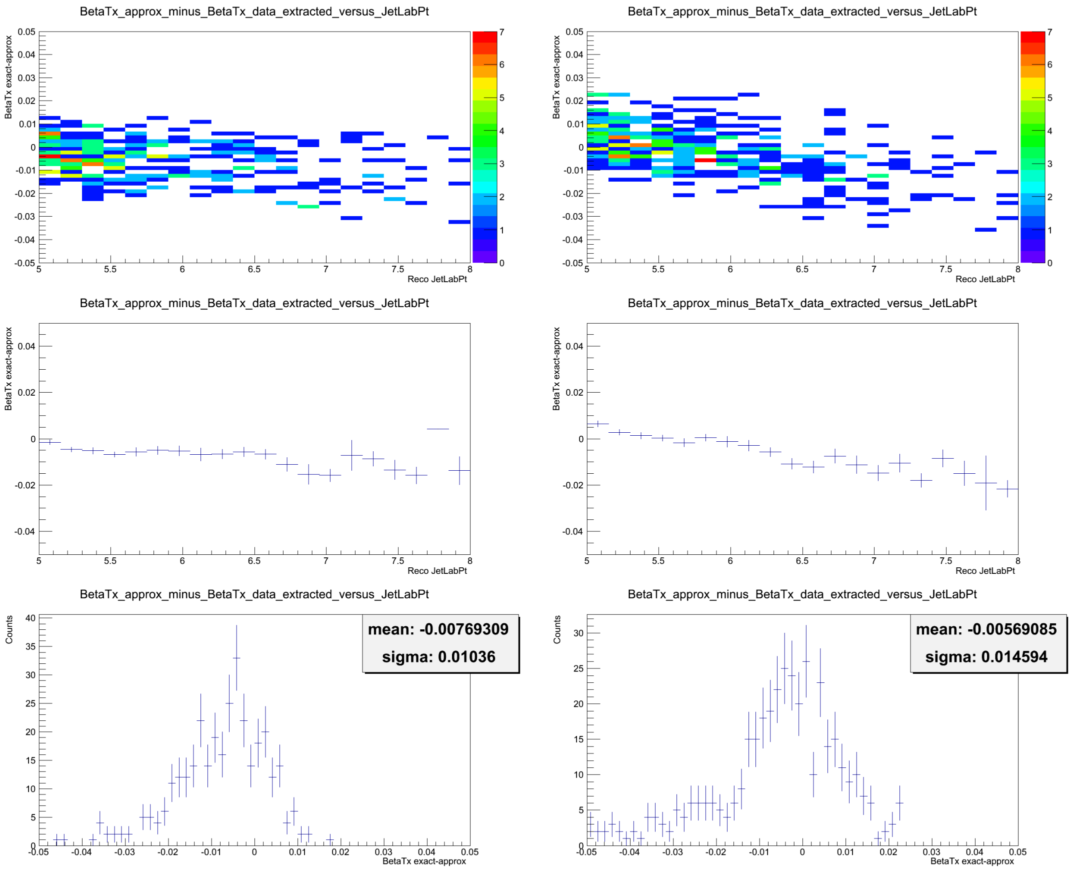

Figure 8.3 Comparison between simulation approximated and real data extracted $\beta_{\perp x}$ parameter. Top: Y-axis: $\beta_{\perp x sim}$-$\beta_{\perp x real}$, X-axis: Reconstructed $|\overrightarrow{Jet}_{f,lab_{\perp}}|$. Middle: Profile histogram of above. Bottom: Projection onto the Y-axis of the top histograms. Left: Jet in West arm, Right: Jet in East arm.

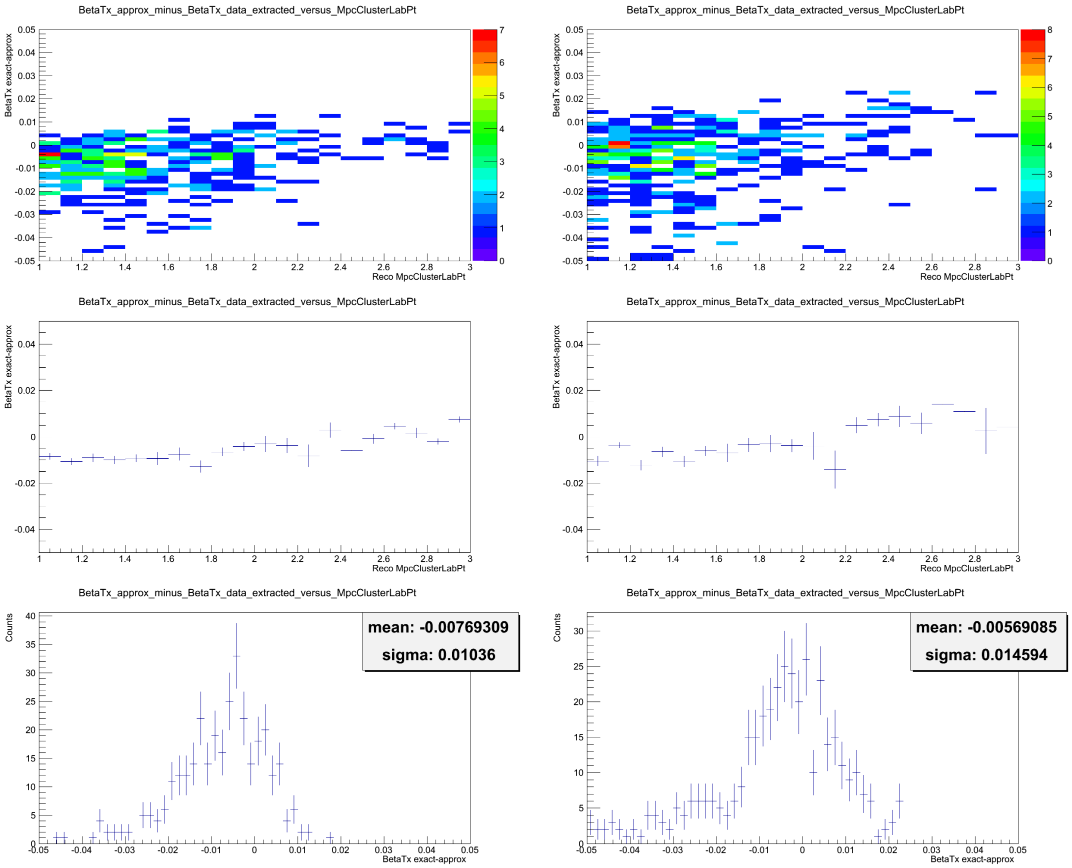

Figure 8.4 Comparison between simulation approximated and real data extracted $\beta_{\perp x}$ parameter. Top: Y-axis: $\beta_{\perp x sim}$-$\beta_{\perp x real}$, X-axis: Reconstructed $|\overrightarrow{\pi^0}_{f,lab_\perp}|$. Middle: Profile histogram of above. Bottom: Projection onto the Y-axis of the top histograms. Left: Jet in West arm, Right: Jet in East arm.

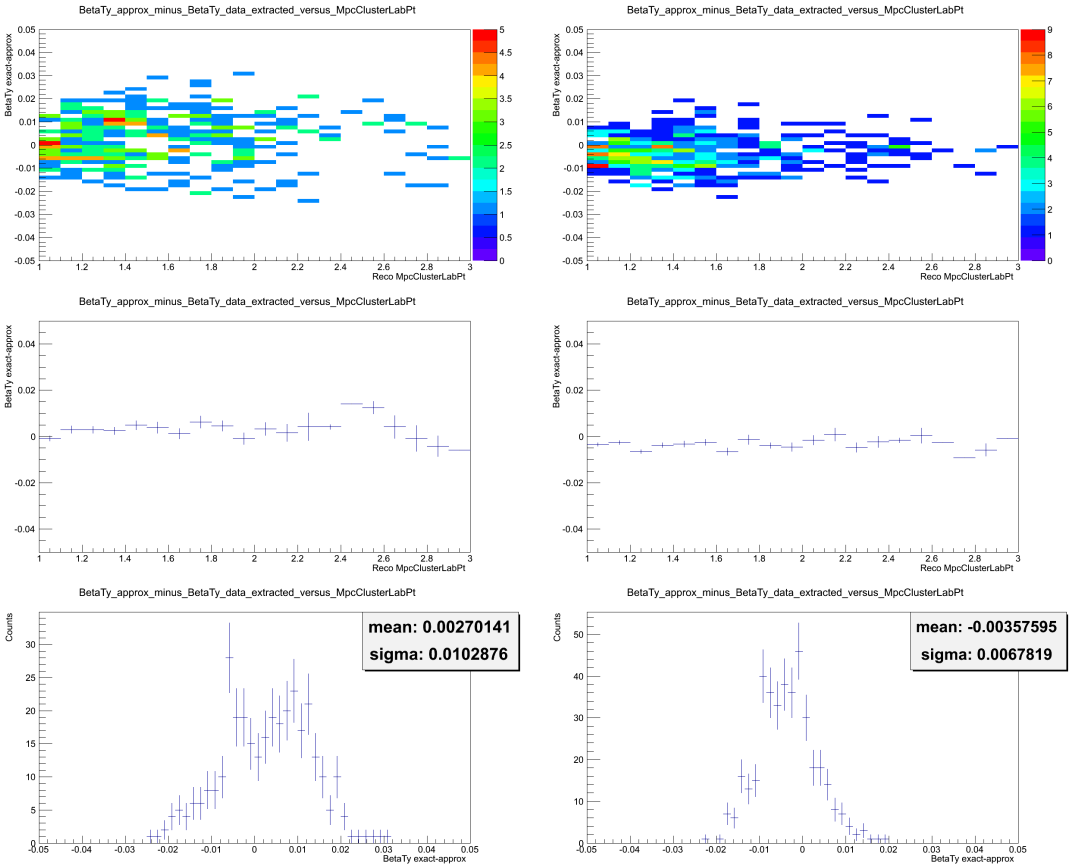

Figure 8.5 Comparison between simulation approximated and real data extracted $\beta_{\perp y}$ parameter. Top: Y-axis: $\beta_{\perp y_{sim}}$-$\beta_{\perp y_{real}}$, X-axis: Reconstructed $|\overrightarrow{\pi^0}_{f,lab_\perp}|$. Middle: Profile histogram of above. Bottom: Projection onto the Y-axis of the top histograms. Left: Jet in West arm, Right: Jet in East arm.

8.1.2 Final State Parton Approximations - Transverse Scattering Frame

Using both $\overrightarrow{G}_{f,lab}$ and $\overrightarrow{\beta}_\perp$ we can now obtain $\overrightarrow{G}_{f,tSF}$. The p_T distribution of which is shown in Figure 8.6 for both simulation and real data. Similarly, $\overrightarrow{Q}_{f,tSF}$ is obtained from the Lorentz transform of $\overrightarrow{Q}_{f,lab}$ using our $\overrightarrow{\beta}_\perp$ parameterization. The p_T distribution is shown in Figure 8.7, both simulation and real data are shown for comparison.

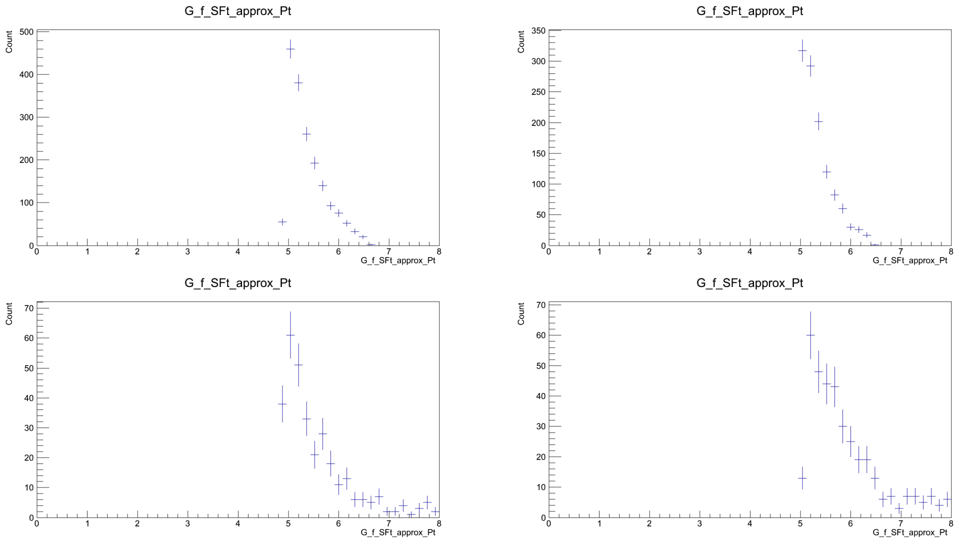

Figure 8.6 Comparison between simulation and real data approximated final-state transverse scattering frame gluons. Y-axis: Counts, X-axis: $|\overrightarrow{G}_{f,tSF_{\perp}}|$. Top: Simulated data, Bottom: Real data. Left: Jet in West arm, Right: Jet in East arm.

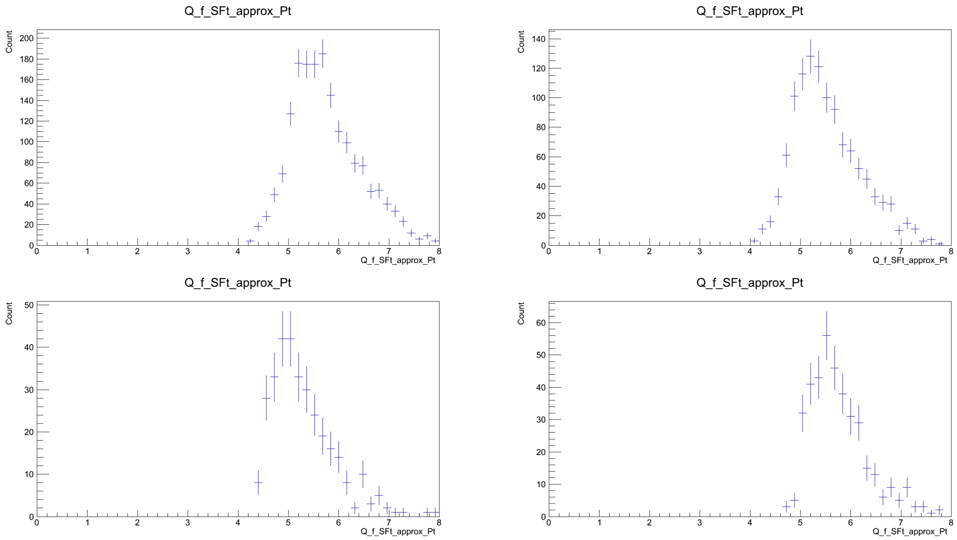

Figure 8.7 Comparison between simulation and real data approximated final-state transverse scattering frame quarks. Y-axis: Counts, X-axis: $|\overrightarrow{Q}_{f,tSF_{\perp}}|$. Top: Simulated data, Bottom: Real data. Left: Jet in West arm, Right: Jet in East arm.

8.2 Boost, Flip, and Swap

We have now determined the approximated vectors that we require to perform the boost, flip, and swap procedure as discussed in Chapter 5, Section 7.4, and outlined in Figure 7.2. Namely, we now have our approximated $\overrightarrow{\beta}_{\perp}$, $\overrightarrow{G}_{f,tSF}$, and $\overrightarrow{Q}_{f,tSF}$ objects. The boost, flip, and swap procedure is performed and we obtain our $\overrightarrow{JProxy}_{f,lab}$ momentum vector. Now the comparison between the jet proxy and the π^0 can be performed.

8.2.1 Jet Proxy Frame

In order to study the azimuthal asymmetry of π^0 production about the jet proxy axis we must define the jet proxy axis on an event-by-event basis. To that end, once the jet proxy is known we transform our system into what is called the "jet proxy frame". In this frame the jet proxy points along the $+\hat{z}$ direction and the ϕ angle is measured in the plane transverse to the jet proxy momentum direction. Both the lab-frame North-going proton polarization vector ($\overrightarrow{S}_{f,lab}$) and the π^0 ($\overrightarrow{\pi^0}_{f,lab}$) are translated into this jet proxy frame. For convenience, the jet proxy frame is labeled as "JP" and the $\overrightarrow{S}_{f,lab}$ and $\overrightarrow{\pi^0}_{f,lab}$ objects become $\overrightarrow{S}_{f,JP}$ and $\overrightarrow{\pi^0}_{f,JP}$ respectively. As a convenient choice of y-axis in the jet proxy frame is when the transverse plane is rotated in ϕ such that the y-axis lies along the $\overrightarrow{S}_{f,JP}$ direction. It is then a simple matter to measure, in the JP transverse plane, the angle from the $\overrightarrow{S}_{f,JP}$ vector to the $\overrightarrow{\pi^0}_{f,JP}$. This angle measure is labeled ϕ in the next sections and is measured in the clockwise direction when looking parallel to the jet proxy momentum vector direction. Since a known and quantified spin-independent $\Delta\eta$ between $\overrightarrow{Q}_{f,lab}$ and $\overrightarrow{\pi^0}_{f,lab}$ exists in simulation (Figure 7.6), it is subtracted from $\overrightarrow{\pi^0}_{f,lab}$ before translation into the jet proxy frame.

Figure 8.8 shows the ϕ measurement scheme as described above.

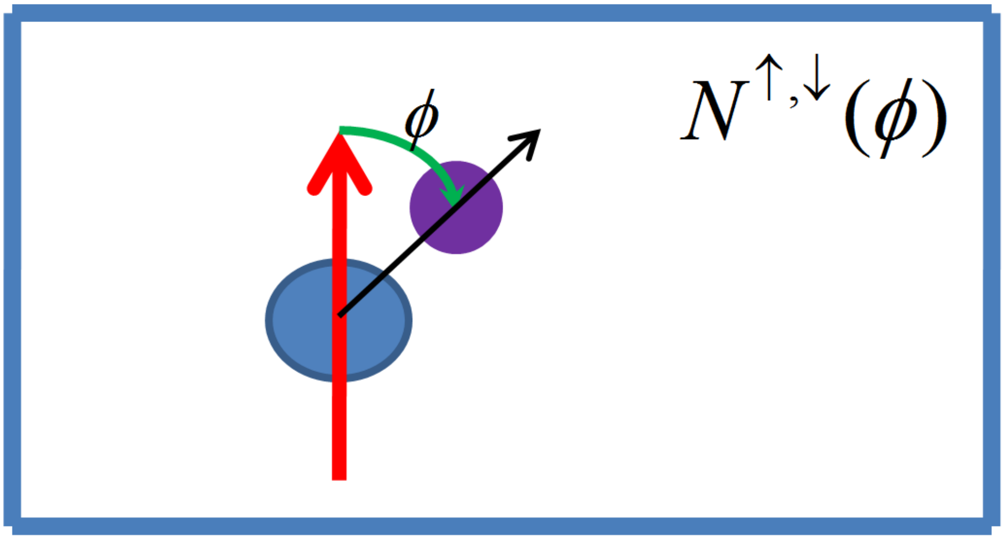

Figure 8.8 The definition of our ϕ measure. Blue circle: jet proxy momentum vector, pointed into the page. Purple circle: π^0 momentum vector, pointed into the page ($\overrightarrow{\pi^0}_{f,JP}$). Red arrow: Proton polarization vector translated into the jet proxy frame ($\overrightarrow{S}_{f,JP}$). Green arrow: ϕ measurement direction from the spin vector to the π^0. Nomenclature is explained in Section 8.3

8.3 Asymmetry Calculation

There are several well-established methods for the calculation of an asymmetry and the error associated with that calculation. Several of these are covered in great detail in Reference [38]. The asymmetry, at its core, is an asymmetry in the accepted event cross-section. Without spin-dependence, the cross-section per steradian is:

$$\frac{d\sigma}{d\Omega} = \frac{N}{\mathcal{L}} \tag{8.1}$$

Where:

- σ: The cross-section
- Ω: Solid angle in space

- N: Number of accepted events
- $\mathcal{L}$: Beam luminosity

If the cross-section has a ϕ angle (relative to the spin-vector) dependence due to a spin effect the cross-section becomes:

$$\frac{d\sigma}{d\Omega}(\phi) = (\frac{d\sigma}{d\Omega})_0 = \frac{N(\phi)}{\mathcal{L}} \tag{8.2}$$

Where $(\frac{d\sigma}{d\Omega})_0$ is the spin-independent cross-section from Equation 8.1. Finally, the asymmetry factor (A_N, the analyzing power) can be extracted from:

$$N(\phi) = \mathcal{L}a(\phi)(\frac{d\sigma}{d\Omega})_0(1 + A_N P_y cos(\phi)) \tag{8.3}$$

Where P_y is the beam polarization, $a(\phi)$ is an acceptance and efficiency correction, and A_N is the analyzing power. In this analysis, the ϕ angle is measured in the jet proxy frame which changes on an event-by-event basis (though, on average it is consistent), the luminosity is no longer the beam luminosity and is instead the luminosity of central-jet and forward-π^0 events, and finally the acceptance factor ($a(\phi)$) changes with every event. The luminosity factor and the acceptance factor must be circumvented to extract the A_N in this analysis.

8.3.1 Asymmetry Calculation - Naive Formulation

In the naive formulation, the asymmetry calculation is just a comparison between counts to the “right” and “left” of the spin vector. To that end, we can formulate the raw asymmetry as:

$$\epsilon_N(\phi) = \frac{N^{\uparrow}(right) - N^{\uparrow}(left)}{N^{\uparrow}(right) + N^{\uparrow}(left)} = \frac{N^{\uparrow}(\phi) - N^{\uparrow}(\phi + \pi)}{N^{\uparrow}(\phi) + N^{\uparrow}(\phi + \pi)} \tag{8.4}$$

which allows us to calculate the A_N by taking into account the beam polarization:

$$A_N(\phi) = \frac{\epsilon_N(\phi)}{P_y} \tag{8.5}$$

Following John Koster’s lead [38] I insert Equation 8.3 into Equation 8.4 to obtain:

$$\epsilon_N(\phi) = \frac{\mathcal{L}a(\phi)(\frac{d\sigma}{d\Omega})_0(1 + A_N P_y cos(\phi)) - \mathcal{L}a(\phi+\pi)(\frac{d\sigma}{d\Omega})_0(1 + A_N P_y cos(\phi+\pi))}{\mathcal{L}a(\phi)(\frac{d\sigma}{d\Omega})_0(1 + A_N P_y cos(\phi)) + \mathcal{L}a(\phi+\pi)(\frac{d\sigma}{d\Omega})_0(1 + A_N P_y cos(\phi+\pi))} \tag{8.6}$$

which reduces to:

$$\epsilon_N(\phi) = \frac{a(\phi)(1 + A_N P_y cos(\phi)) - a(\phi+\pi)(1 + A_N P_y cos(\phi+\pi))}{a(\phi)(1 + A_N P_y cos(\phi)) + a(\phi+\pi)(1 + A_N P_y cos(\phi+\pi))} \tag{8.7}$$

As can be seen, this formulation does not eliminate the acceptance and efficiency factor, an intractable factor which changes on an event-by-event basis in this analysis. Luckily, there are better (more complex) options.

8.3.2 Asymmetry Calculation - Square Root Formula

The choice of asymmetry calculation made here is the square-root formula:

$$\epsilon^{sqrt}(\phi) = \frac{\sqrt{N^{\uparrow}(\phi)N^{\downarrow}(\phi)} - \sqrt{N^{\uparrow}(\phi+\pi)N^{\downarrow}(\phi+\pi)}}{\sqrt{N^{\uparrow}(\phi)N^{\downarrow}(\phi)} + \sqrt{N^{\uparrow}(\phi+\pi)N^{\downarrow}(\phi+\pi)}} \tag{8.8}$$

Where:

- $\epsilon^{sqrt}(\phi)$ = The raw asymmetry as measured
- ϕ = Angle as defined in Section 8.2.1. The angle is measured from the proton polarization vector in the JP frame ($\overrightarrow{S}_{f,JP}$) to $\overrightarrow{\pi^0}_{f,JP}$ in a clockwise manner in the plane transverse to the jet proxy momentum direction. This angle measure is between zero and 2π: $[0,2\pi)$.
- $N^{\uparrow}(\phi)$ = Number of events where the π^0 is found within some angular inverval ϕ when the proton polarization vector in the lab frame was "up" ($+\hat{y}$ direction).
- $N^{\downarrow}(\phi)$ = Number of events where the π^0 is found within some angular inverval ϕ when the proton polarization vector in the lab frame was "down" ($-\hat{y}$ direction).
- $N^{\uparrow}(\phi)$ = Number of events where the π^0 is found within some angular inverval $\phi+\pi$ when the proton polarization vector in the lab frame was "up" ($+\hat{y}$ direction).
- $N^{\downarrow}(\phi)$ = Number of events where the π^0 is found within some angular inverval $\phi+\pi$ when the proton polarization vector in the lab frame was "down" ($-\hat{y}$ direction).

The associated statistical error (variance) is:

$$\sigma^2(\epsilon^{sqrt}(\phi)) = \frac{1}{16}(1-\epsilon^2)^2[\frac{1}{N^{\uparrow}(\phi)} + \frac{1}{N^{\downarrow}(\phi)} + \frac{1}{N^{\uparrow}(\phi+\pi)} + \frac{1}{N^{\downarrow}(\phi+\pi)}] \tag{8.9}$$

As a simple example, where only two ϕ intervals are defined, $[0,\pi)$ and $[\pi,2\pi)$, the square-root formula is a comparison between the number of π^0s found to the "right" and "left" of the spin vector in the JP frame ($\overrightarrow{S}_{f,JP}$). The elimination of $a(\phi)$ can be seen in the subtraction of the geometric mean of the counts ($\sqrt{N^{\uparrow}(\phi)N^{\downarrow}(\phi)}$) in the numerator of Equation 8.8. Remembering that ϕ when the spin polarization is "up" is equal to $\phi+\pi$ when the spin polarization is "down" ($a^{\uparrow}(\phi) = a^{\downarrow}(\phi+\pi)$, on average). Inserting Equation 8.3 into the first term of Equation 8.8 yields:

$$\begin{aligned}\sqrt{N^{\uparrow}(\phi)N^{\downarrow}(\phi)} = &\sqrt{(\mathcal{L}^{\uparrow}a^{\uparrow}(\phi)(\frac{d\sigma}{d\Omega})_0(1+A_NP_ycos(\phi)))(\mathcal{L}^{\downarrow}a^{\downarrow}(\phi)(\frac{d\sigma}{d\Omega})_0(1+A_NP_ycos(\phi)))}\\ &-\sqrt{(\mathcal{L}^{\uparrow}a^{\uparrow}(\phi+\pi)(\frac{d\sigma}{d\Omega})_0(1+A_NP_ycos(\phi+\pi)))(\mathcal{L}^{\downarrow}a^{\downarrow}(\phi+\pi)(\frac{d\sigma}{d\Omega})_0(1+A_NP_ycos(\phi+\pi)))}\end{aligned} \tag{8.10}$$

which reduces to:

$$\begin{aligned}\sqrt{N^{\uparrow}(\phi)N^{\downarrow}(\phi)} = &\sqrt{\mathcal{L}^{\uparrow}\mathcal{L}^{\downarrow}a^{\uparrow}(\phi)a^{\downarrow}(\phi)(\frac{d\sigma}{d\Omega})_0}\sqrt{(1+A_NP_ycos(\phi))(1+A_NP_ycos(\phi))}\\ &-\sqrt{\mathcal{L}^{\uparrow}\mathcal{L}^{\downarrow}a^{\uparrow}(\phi+\pi)a^{\downarrow}(\phi+\pi)(\frac{d\sigma}{d\Omega})_0}\sqrt{(1+A_NP_ycos(\phi+\pi))(1+A_NP_ycos(\phi+\pi))}\end{aligned} \tag{8.11}$$

Using the fact that $a^{\uparrow}(\phi) = a^{\downarrow}(\phi+\pi)$ we obtain:

$$\begin{aligned}\sqrt{N^{\uparrow}(\phi)N^{\downarrow}(\phi)} = \sqrt{\mathcal{L}^{\uparrow}\mathcal{L}^{\downarrow}a^{\downarrow}(\phi+\pi)a^{\downarrow}(\phi)(\frac{d\sigma}{d\Omega})_0}&(\sqrt{(1+A_NP_ycos(\phi))(1+A_NP_ycos(\phi))}\\ &-\sqrt{(1+A_NP_ycos(\phi+\pi))(1+A_NP_ycos(\phi+\pi))})\end{aligned} \tag{8.12}$$

Incorporating the denominator of Equation 8.8 eliminates the common $\sqrt{\mathcal{L}^{\uparrow}\mathcal{L}^{\downarrow}a^{\downarrow}(\phi+\pi)a^{\downarrow}(\phi)(\frac{d\sigma}{d\Omega})_0}$ term and recognizing that $cos(\phi) = -cos(\phi+\pi)$ leaves us with:

$$\epsilon^{sqrt}(\phi) = \frac{\sqrt{(1+A_NP_ycos(\phi))(1+A_NP_ycos(\phi))} - \sqrt{(1-A_NP_ycos(\phi))(1-A_NP_ycos(\phi))}}{\sqrt{(1+A_NP_ycos(\phi))(1+A_NP_ycos(\phi))} + \sqrt{(1-A_NP_ycos(\phi))(1-A_NP_ycos(\phi))}} \tag{8.13}$$

and finally:

$$\epsilon^{sqrt}(\phi) = A_N P_y cos(\phi) \tag{8.14}$$

Which is independent of acceptance, efficiency, and luminosity effects. We measure ϵ in the data via Equation 8.8 and use the known P_y to extract A_N.

8.4 Neutral Pions in the Jet Proxy Frame

Since we have our $\overrightarrow{S}_{f,JP}$ and $\overrightarrow{\pi^0}_{f,JP}$ vectors in the jet proxy frame (Section 8.2.1) and our method for extracting the raw asymmetry (Section 8.3.2) we can now perform the extraction.

The two-dimensional distribution of $\overrightarrow{\pi^0}_{f,JP}$ momentum in the x-y plane (in the jet proxy frame) is shown in Figure 8.9. As stated, the $+\hat{y}$ direction is always the direction of $\overrightarrow{S}_{f,JP}$ in the x-y plane. A portion of the bias seen here can be understood from the $\Delta\eta$ distributions between the π^0 and jet proxy as shown in Figures 8.10 and 8.11 which show a net-positive $\Delta\eta$.

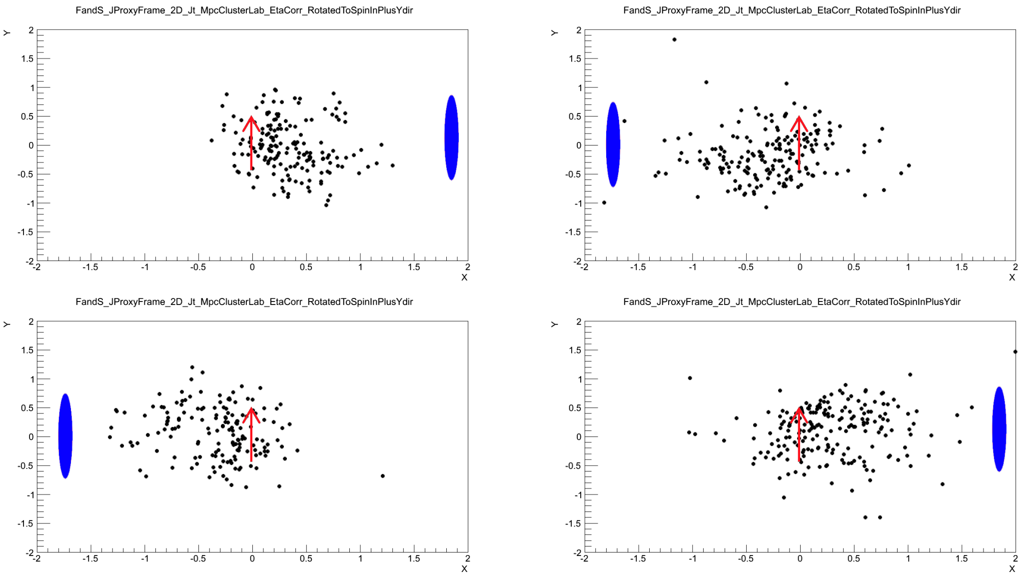

Figure 8.9 Distribution of $\overrightarrow{\pi^0}_{f,JP}$ momentum in the x-y plane in the jet proxy frame. The y-axis corresponds to the $\overrightarrow{S}_{f,JP}$ direction in the x-y plane (also displayed as a black arrow). The blue ellipse corresponds to the rough (relative) location of the North-going beam pipe. The x and y axis are $\overrightarrow{\pi^0}_{f,JP_x}$ and $\overrightarrow{\pi^0}_{f,JP_y}$ respectively. Top: Lab-frame proton events with "up" polarization, Bottom: Lab-frame proton events with "down" polarization. Left: Jet in West arm, Right: Jet in East arm.

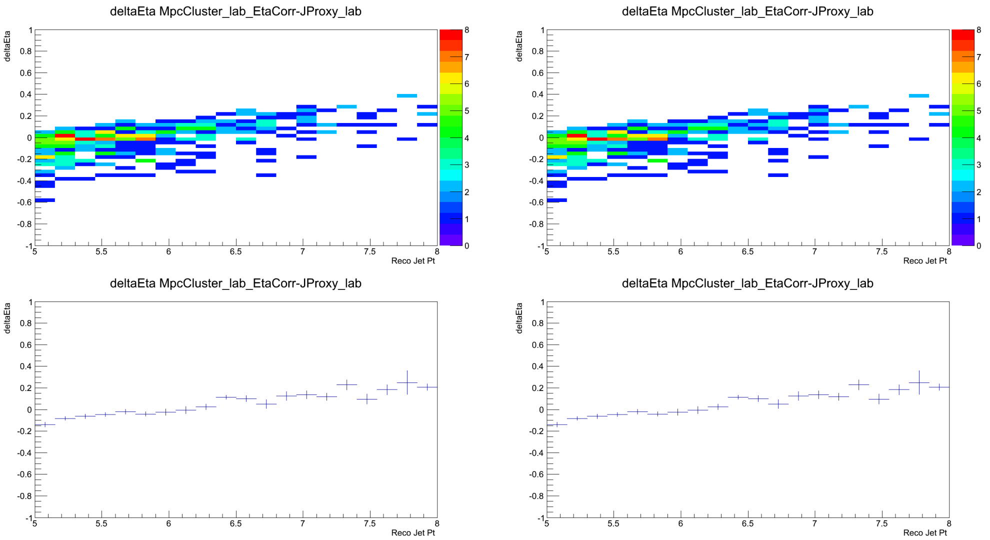

Figure 8.10 Top: The distribution of $\Delta\eta$ between the π^0 and the jet proxy in the lab frame. Y-axis: $\Delta\eta$, X-axis: $\overrightarrow{Jet}_{f,lab_\perp}$. Bottom: Profile histogram of the above plot. Left: Jet in West arm, Right: Jet in East arm.

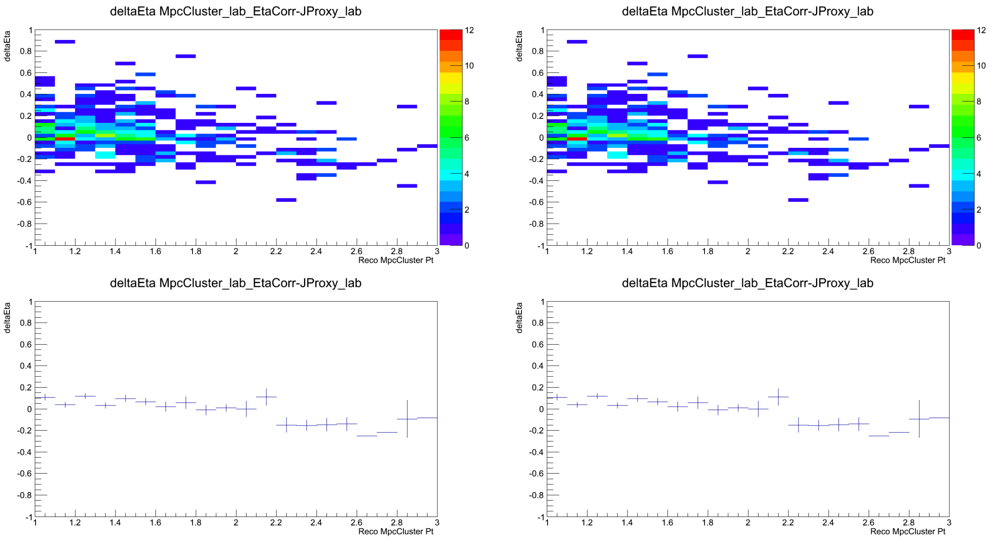

Figure 8.11 Top: The distribution of $\Delta\eta$ between the π^0 and the jet proxy in the lab frame. Y-axis: $\Delta\eta$, X-axis: $|\overrightarrow{Jet}_{f,lab_\perp}|$. Bottom: Profile histogram of the above plot. Left: Jet in West arm, Right: Jet in East arm.

8.5 $\Delta\phi$ from Spin Vector to π^0 in Jet Proxy Frame

Two-dimensional distributions of $\Delta\phi$ measured from $\overrightarrow{S}_{f,JP}$ to $\overrightarrow{\pi^0}_{f,JP}$ in the manner described in Section 8.2.1 are shown in Figures 8.12 and 8.13.

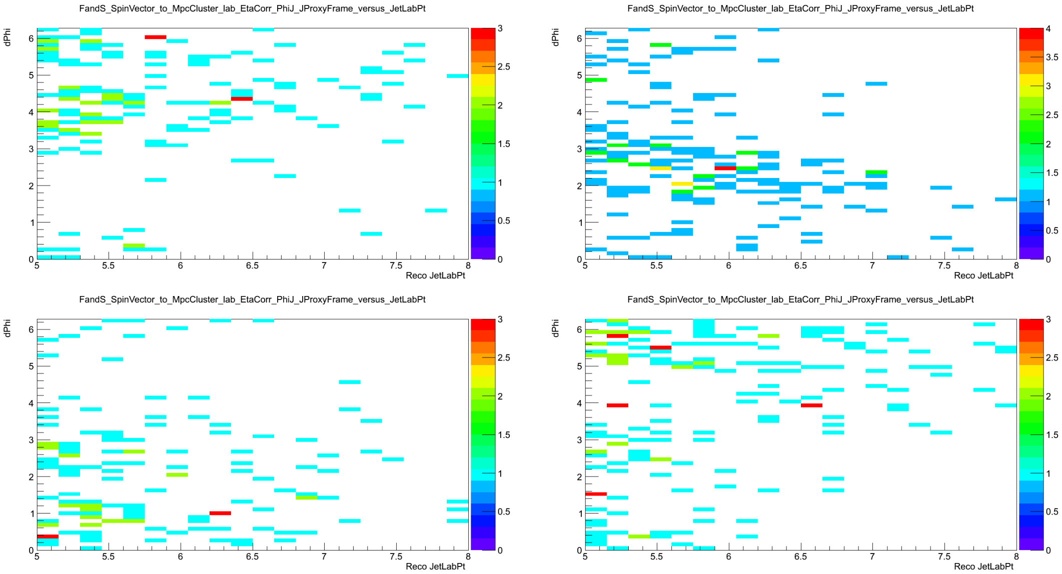

Figure 8.12 Distribution of $\Delta\phi$ measured from $\overrightarrow{S}_{f,JP}$ to $\overrightarrow{\pi^0}_{f,JP}$. Y-axis: $\Delta\phi$, X-axis: $|\overrightarrow{Jet}_{f,lab_\perp}|$. Top: Proton polarization vector “up”, Bottom: proton polarization “down”. Left: Jet in West arm, Right: Jet in East arm.

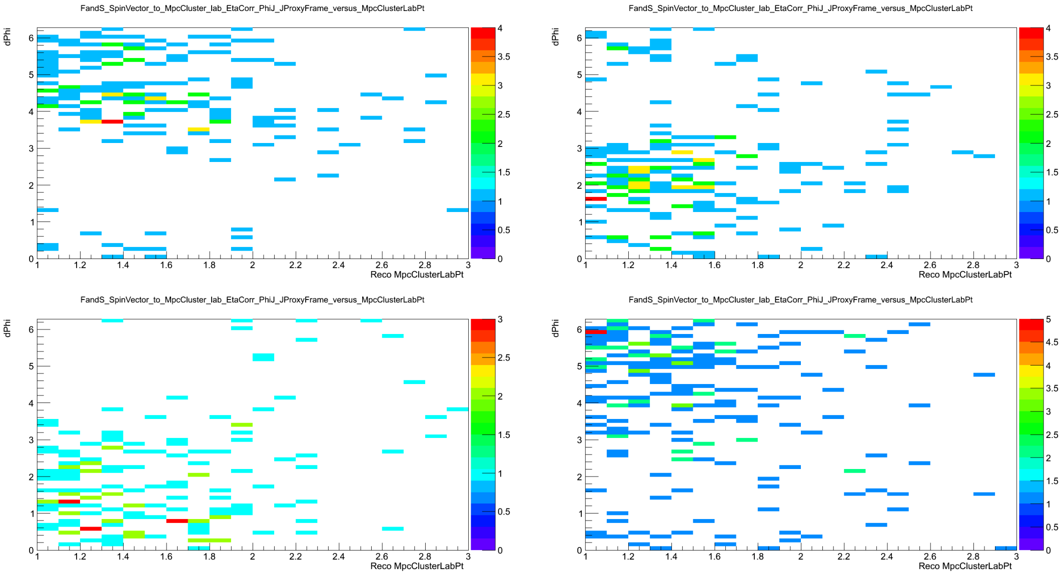

Figure 8.13 Distribution of $\Delta\phi$ measured from $\overrightarrow{S}_{f,JP}$ to $\overrightarrow{\pi^0}_{f,JP}$. Y-axis: $\Delta\phi$, X-axis: $|\overrightarrow{\pi^0}_{f,lab_\perp}|$. Top: Proton polarization vector "up", Bottom: proton polarization "down". Left: Jet in West arm, Right: Jet in East arm.

The analysis is then broken up into three distinct p_T regions for both $|\overrightarrow{Jet}_{f,lab_\perp}|$ and $|\overrightarrow{\pi^0}_{f,lab_\perp}|$. The $|\overrightarrow{Jet}_{f,lab_\perp}|$ regions are defined as (in units of $\frac{GeV}{c}$): $[5, 5.45)$, $[5.45, 6.5)$, and $[6.5, 8.0]$while the $|\overrightarrow{\pi^0}_{f,lab_\perp}|$ regions are: $[1.0, 1.2)$, $[1.2, 2.0)$, and $[2.0, 3.0]$. Figures 8.14 to 8.17 show the ϕ distributions using two ϕ bins (effectively "right" and "left").

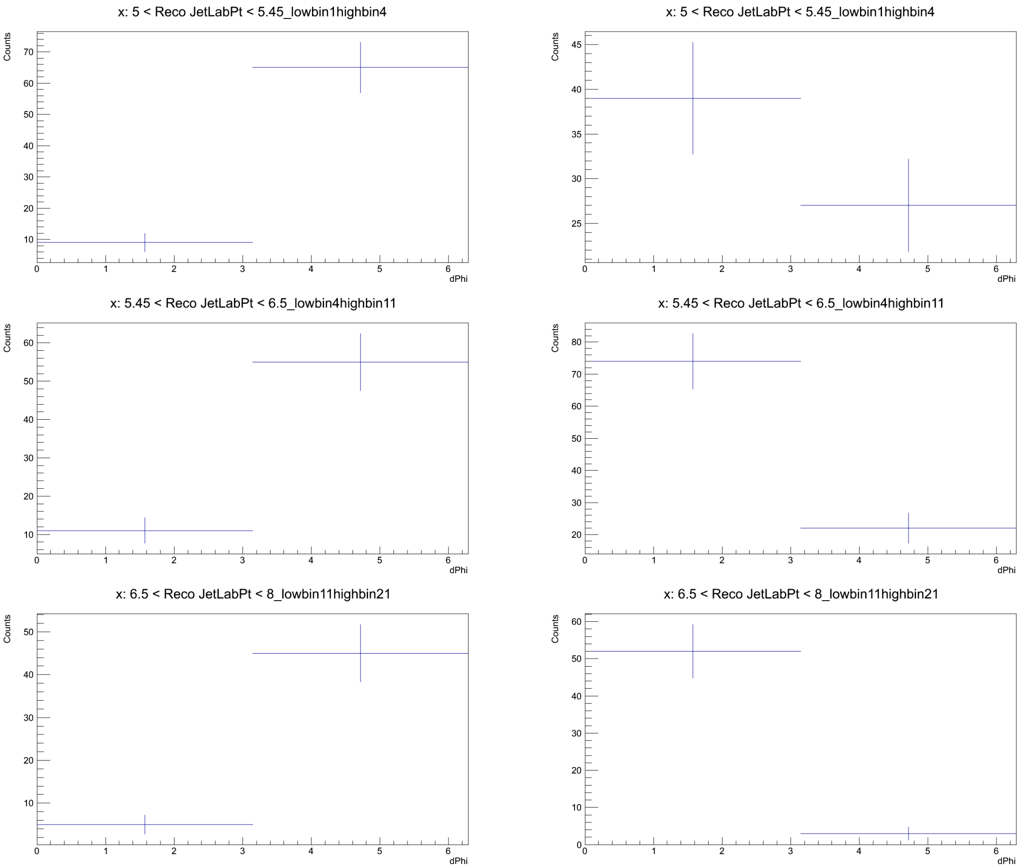

x: 5 < Reco JetLabPt < 5.45_lowbin1highbin4

x: 5 < Reco JetLabPt < 5.45_lowbin1highbin4

x: 5.45 < Reco JetLabPt < 6.5_lowbin4highbin11

x: 5.45 < Reco JetLabPt < 6.5_lowbin4highbin11

x: 6.5 < Reco JetLabPt < 8_lowbin11highbin21

x: 6.5 < Reco JetLabPt < 8_lowbin11highbin21

Figure 8.14 Distribution of $\Delta\phi$ measured from $\overrightarrow{S}_{f,JP}$ to $\overrightarrow{\pi^0}_{f,JP}$ with proton polarization "up". Y-axis: Counts, X-axis: $\Delta\phi$. Top to bottom $|\overrightarrow{Jet}_{f,lab_\perp}|$ regions $(\frac{GeV}{c})$: $[5, 5.45)$, $[5.45, 6.5)$, and $[6.5, 8.0]$. Left: Jet in West arm, Right: Jet in East arm.

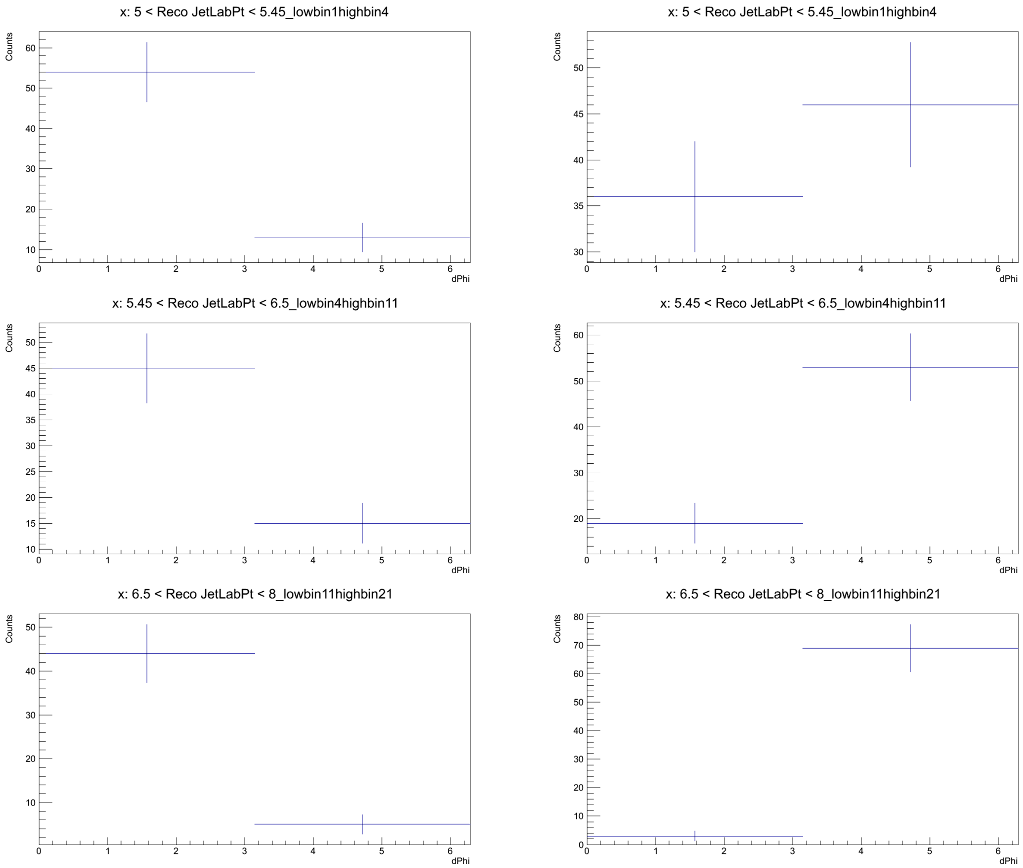

Figure 8.15 Distribution of $\Delta\phi$ measured from $\overrightarrow{S}_{f,JP}$ to $\overrightarrow{\pi^0}_{f,JP}$ with proton polarization "down". Y-axis: Counts, X-axis: $\Delta\phi$. Top to bottom $|\overrightarrow{Jet}_{f,lab_\perp}|$ regions ($\frac{GeV}{c}$): $[5, 5.45)$, $[5.45, 6.5)$, and $[6.5, 8.0]$. Left: Jet in West arm, Right: Jet in East arm.

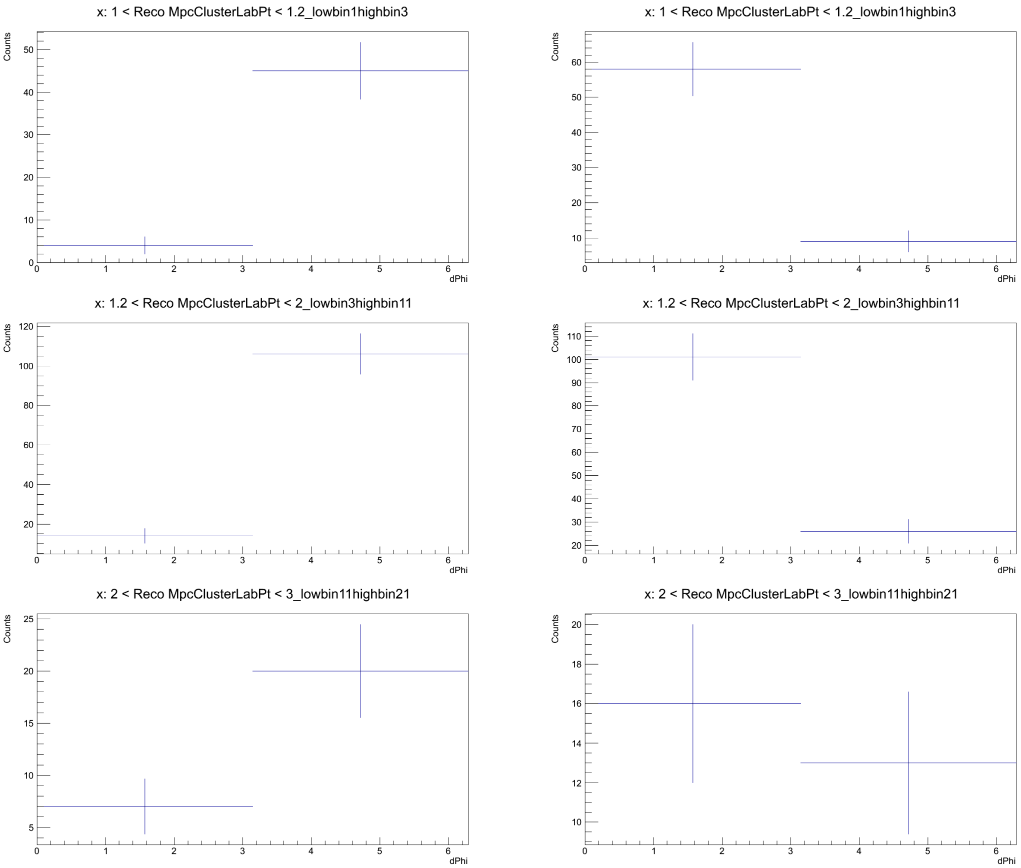

Figure 8.16 Distribution of $\Delta\phi$ measured from $\overrightarrow{S}_{f,JP}$ to $\overrightarrow{\pi^0}_{f,JP}$ with proton polarization "up". Y-axis: Counts, X-axis: $\Delta\phi$. Top to bottom $|\overrightarrow{\pi^0}_{f,lab_\perp}|$ regions $(\frac{GeV}{c})$: $[1.0, 1.2)$, $[1.2, 2.0)$, and $[2.0, 3.0]$. Left: Jet in West arm, Right: Jet in East arm.

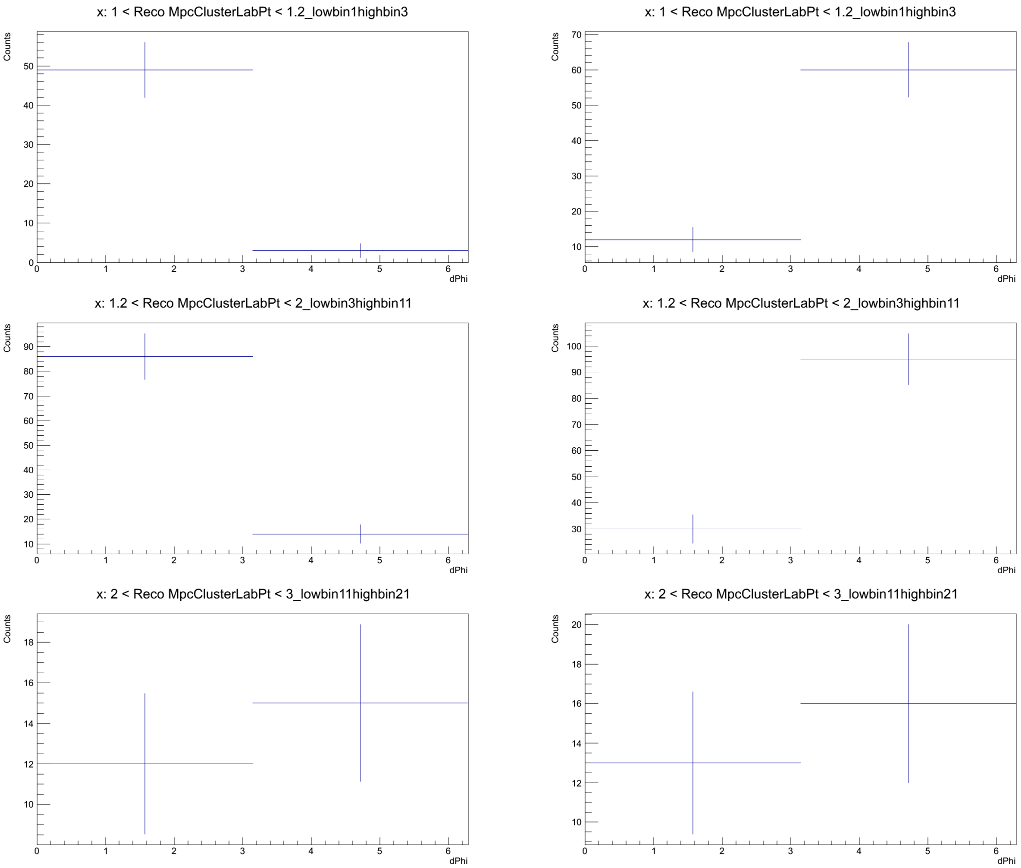

Figure 8.17 Distribution of $\Delta\phi$ measured from $\overrightarrow{S}_{f,JP}$ to $\overrightarrow{\pi^0}_{f,JP}$ with proton polarization "down". Y-axis: Counts, X-axis: $\Delta\phi$. Top to bottom $|\overrightarrow{\pi^0}_{f,lab_\perp}|$ regions ($\frac{GeV}{c}$): $[1.0, 1.2)$, $[1.2, 2.0)$, and $[2.0, 3.0]$, and $[2.0, 3.0]$. Left: Jet in West arm, Right: Jet in East arm.

8.6 Final Raw Asymmetry Calculation

Now that the yields are known and sorted by proton polarization, $\Delta\phi$ in the JP frame, jet arm, jet p_T, and π^0 p_T the calculation of the square-root asymmetry and its associated statistical error (Section 8.3.2) term can occur. Figure 8.18 summarizes the results of the square-root asymmetry calculations. The error bars are purely statistical.

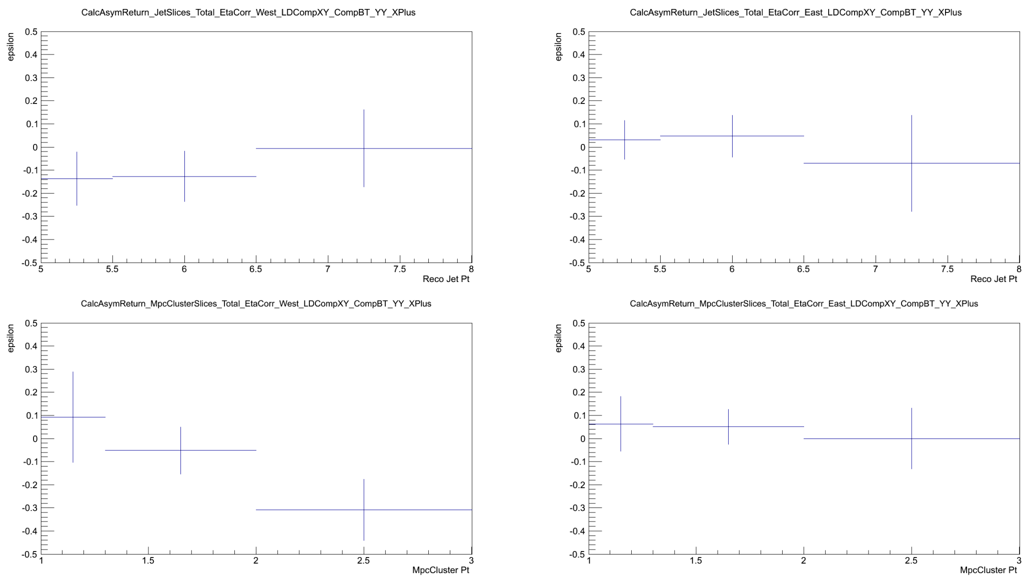

Figure 8.18 Final raw asymmetry. Y-axis: Square-root asymmetry values. Top: X-axis: $|\overrightarrow{Jet}_{f,lab_{\perp}}|$. Bottom: X-axis: $|\overrightarrow{\pi^0}_{f,lab_{\perp}}|$. Left: Jet in West arm, Right: Jet in East arm.

8.7 Estimation of Systematic Error

To provide an estimation of the systematic error induced by the Boost, Flip, and Swap method a final state event weighting is applied to the simulated data. The weighting used is $A \cdot Sin[\phi]$ where A =0.0, 0.2, 0.4 and ϕ is the azimuthal angle between the Pythia truth quark momentum and the Pythia truth MPC π^0 momentum as described in Figure 8.8. Shown below in Figures 8.19 to 8.30 are the square-root asymmetry method (Section 8.3.2) outputs for each central arm jet p_T range, MPC π^0 p_T range, central arm jet arm, and input asymmetry value; for each output the final asymmetry is shown using the Pythia truth information when performing the Boost, Flip, and Swap as well as using our approximated parameterizations (which is what is applied to the real data). The square-root asymmetry method is applied to pairs of bins in ϕ such that each bin at angle ϕ is compared to the bin at angle $\phi + \pi$ (Section 8.3.2, Equation 8.8 uses identical notation). Each figure also includes an $A \cdot Sin[\phi]$ fit curve and the extracted amplitude and amplitude error (due to fitting). The relative difference between the input and output asymmetries leads to a dilution factor imposed by the method. The systematic uncertainty on the measured spin asymmetry induced by the method itself (extraction and application of parameterizations as discussed in Chapter 7) would be represented by a combination of the comparison between the input and output asymmetry as well as the error on the $A \cdot Sin[\phi]$ extractions in Figures 8.19 to 8.30.

One can see that the use of the Pythia truth information to perform the Boost, Flip, and Swap procedure (left-hand side of the aforementioned figures) allows for an accurate reproduction of the input asymmetry in most p_T ranges with sufficient statistics (below 6.5 GeV/c in jet p_T and below 2.0 GeV/c in MPC π^0 p_T). The left-hand sides of Figures 8.19 to 8.30 and Tables 8.1 to 8.4 show that the method itself is valid assuming that the parameterizations in Section 7.2 can be extracted with little error. Due to exceedingly low simulation statistics a parameterization extract with little error is not possible; the results of which are the asymmetry extractions shown on the right-hand sides of Figures 8.19 to 8.30 and in Tables 8.5 to 8.8. Because the systematic error is exceedingly large an exact extraction is not warranted. Conclusions about the validity of the method itself can be seen in Section 8.8.

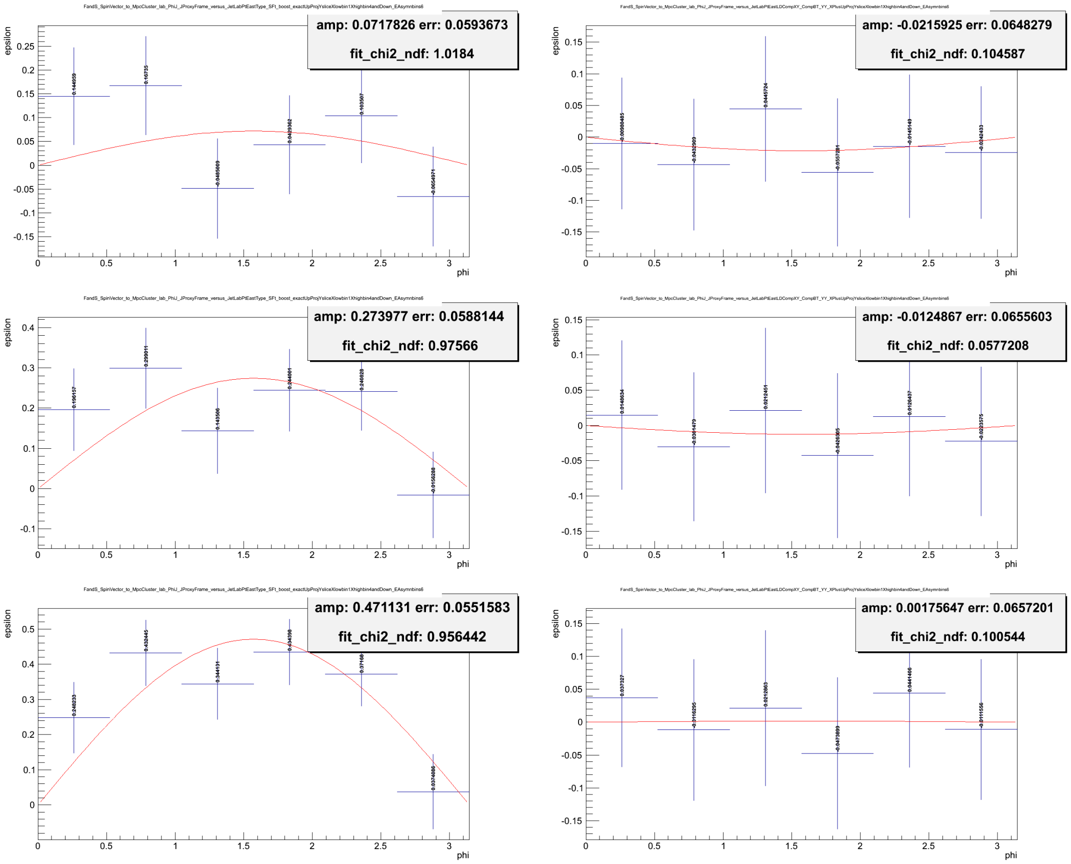

Figure 8.19 Final simulation asymmetry values. Jet in East arm with a pT between 5 GeV and 5.5 GeV. Y-axis: Square-root asymmetry values. X-axis: ϕ. Top: 0% input asymmetry. Middle: 20% input asymmetry. Bottom: 40% input asymmetry. Left: Using Pythia truth values of partonic kinematics, Right: Using approximated values for partonic kinematics.

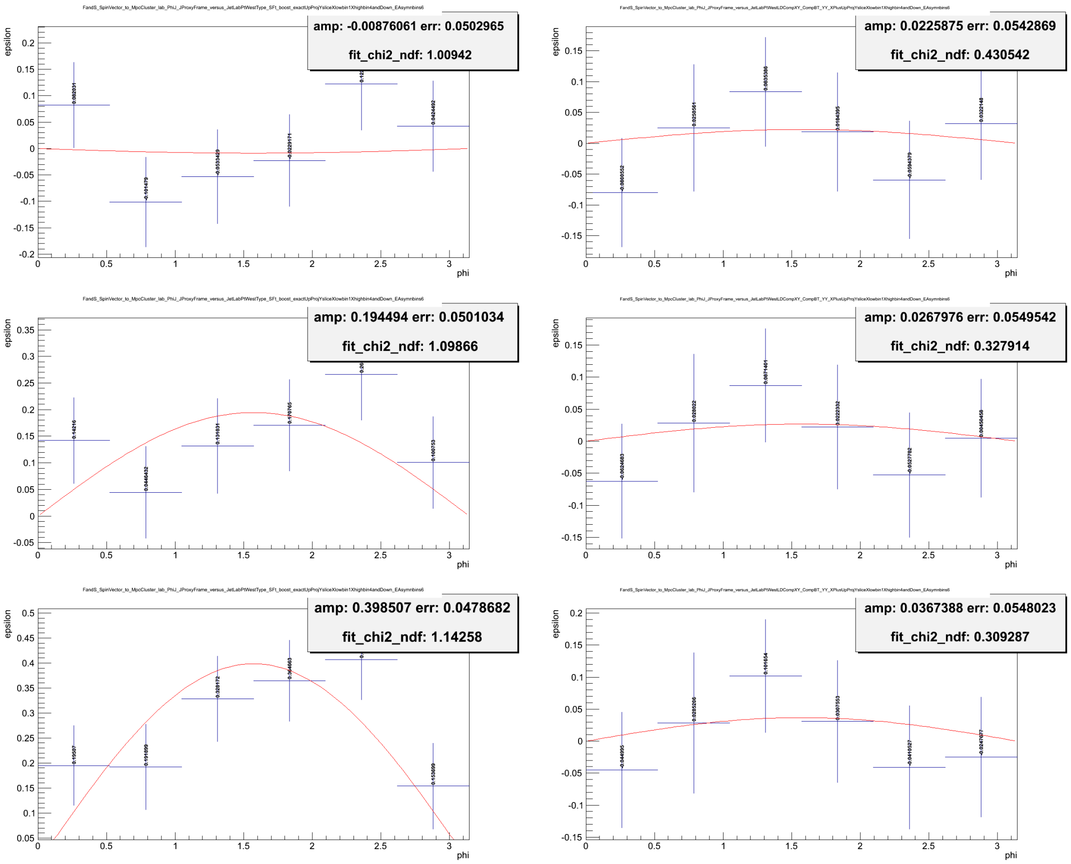

Figure 8.20 Final simulation asymmetry values. Jet in West arm with a pT between 5 GeV and 5.5 GeV. Y-axis: Square-root asymmetry values. X-axis: ϕ. Top: 0% input asymmetry. Middle: 20% input asymmetry. Bottom: 40% input asymmetry. Left: Using Pythia truth values of partonic kinematics, Right: Using approximated values for partonic kinematics.

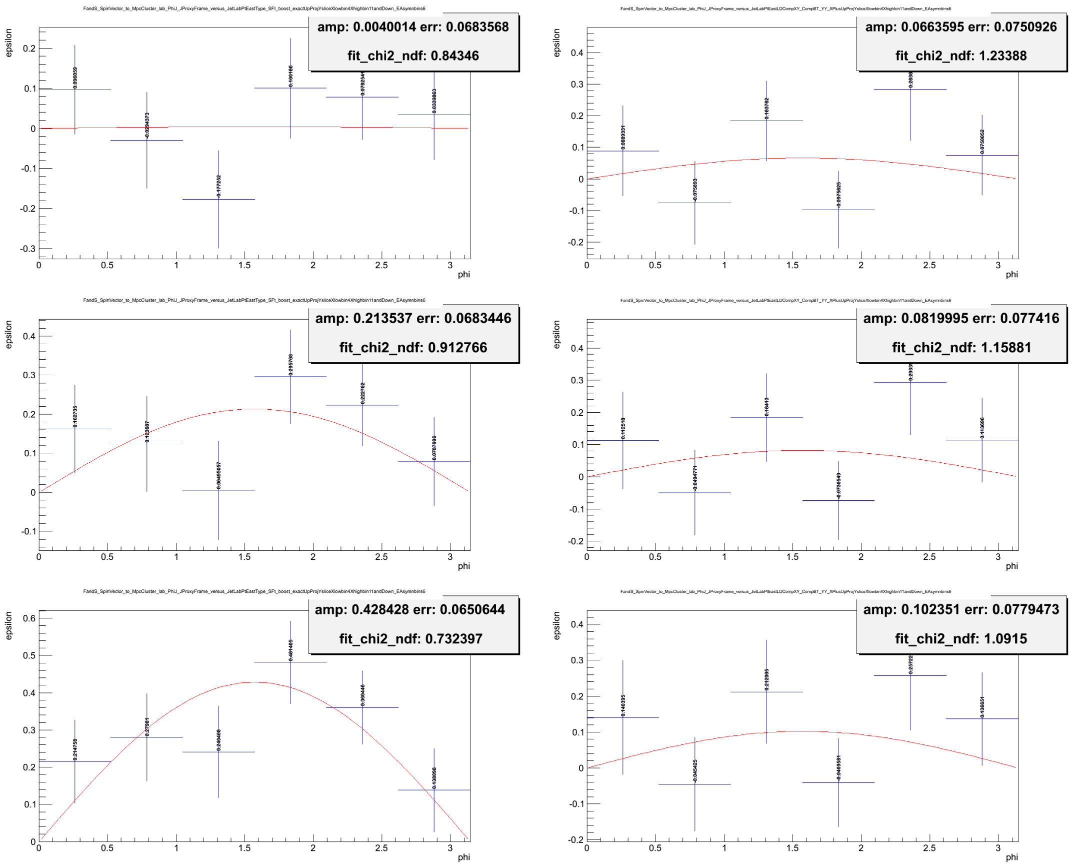

Figure 8.21 Final simulation asymmetry values. Jet in East arm with a pT between 5.5 GeV and 6.5 GeV. Y-axis: Square-root asymmetry values. X-axis: ϕ. Top: 0% input asymmetry. Middle: 20% input asymmetry. Bottom: 40% input asymmetry. Left: Using Pythia truth values of partonic kinematics, Right: Using approximated values for partonic kinematics.

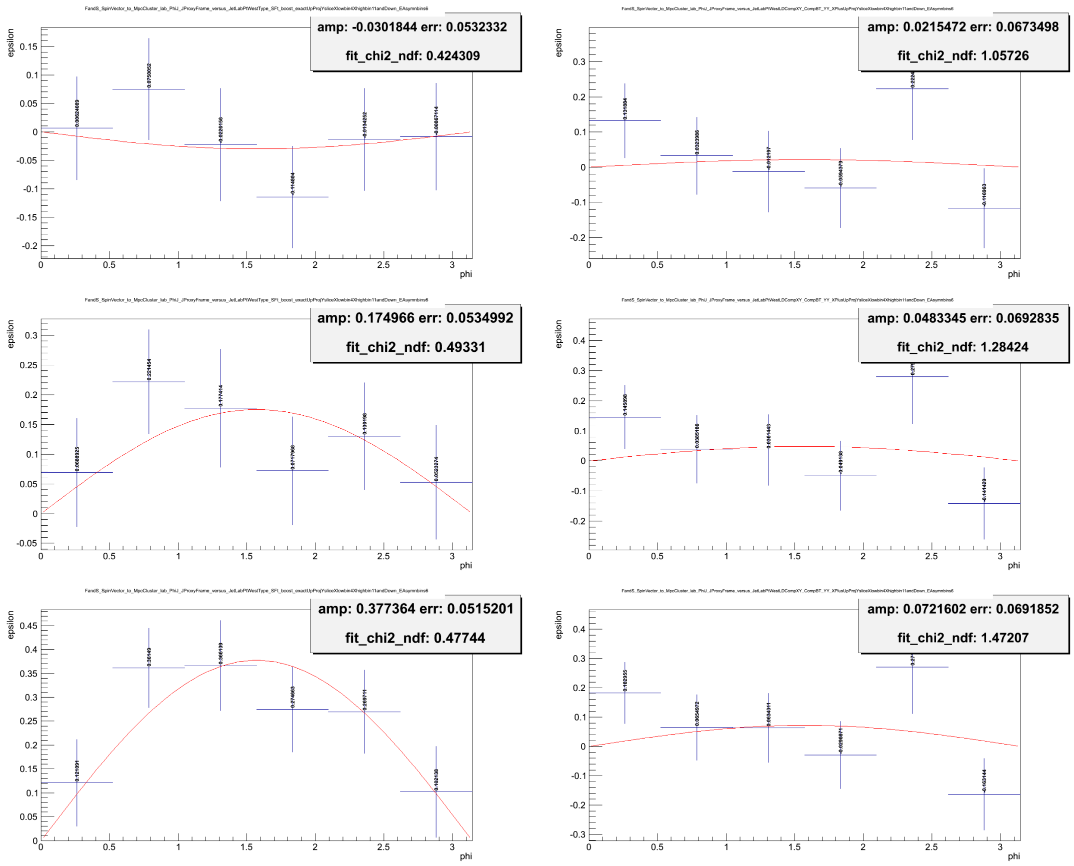

Figure 8.22 Final simulation asymmetry values. Jet in West arm with a pT between 5.5 GeV and 6.5 GeV. Y-axis: Square-root asymmetry values. X-axis: ϕ. Top: 0% input asymmetry. Middle: 20% input asymmetry. Bottom: 40% input asymmetry. Left: Using Pythia truth values of partonic kinematics, Right: Using approximated values for partonic kinematics.

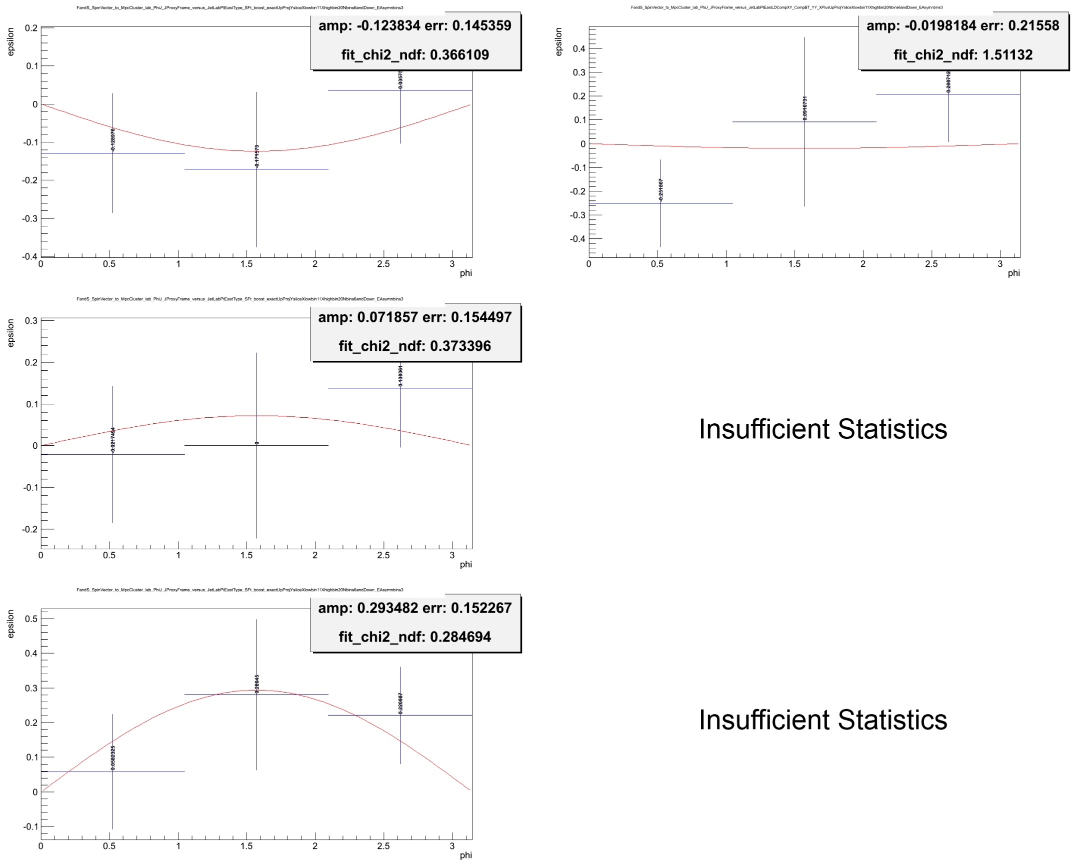

Figure 8.23 Final simulation asymmetry values. Jet in East arm with a pT between 6.5 GeV and 8.0 GeV. Y-axis: Square-root asymmetry values. X-axis: ϕ. Top: 0% input asymmetry. Middle: 20% input asymmetry. Bottom: 40% input asymmetry. Left: Using Pythia truth values of partonic kinematics, Right: Using approximated values for partonic kinematics.

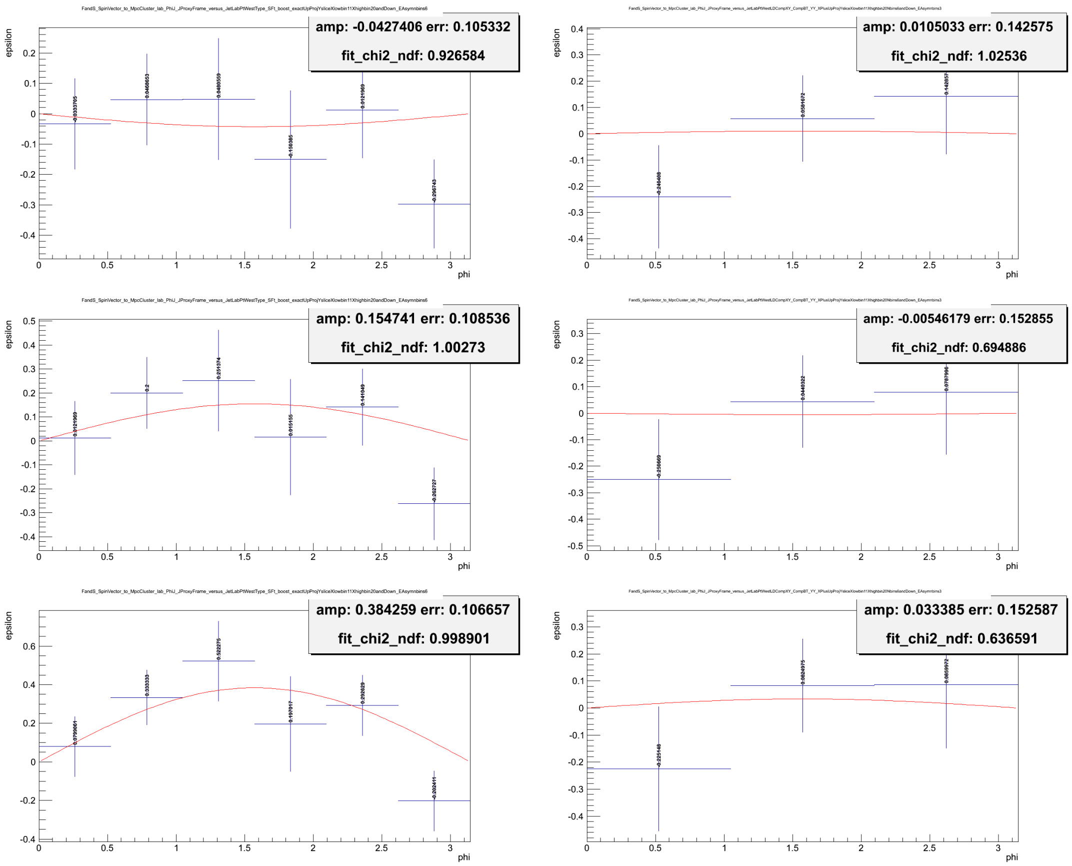

Figure 8.24 Final simulation asymmetry values. Jet in West arm with a pT between 6.5 GeV and 8.0 GeV. Y-axis: Square-root asymmetry values. X-axis: ϕ. Top: 0% input asymmetry. Middle: 20% input asymmetry. Bottom: 40% input asymmetry. Left: Using Pythia truth values of partonic kinematics, Right: Using approximated values for partonic kinematics.

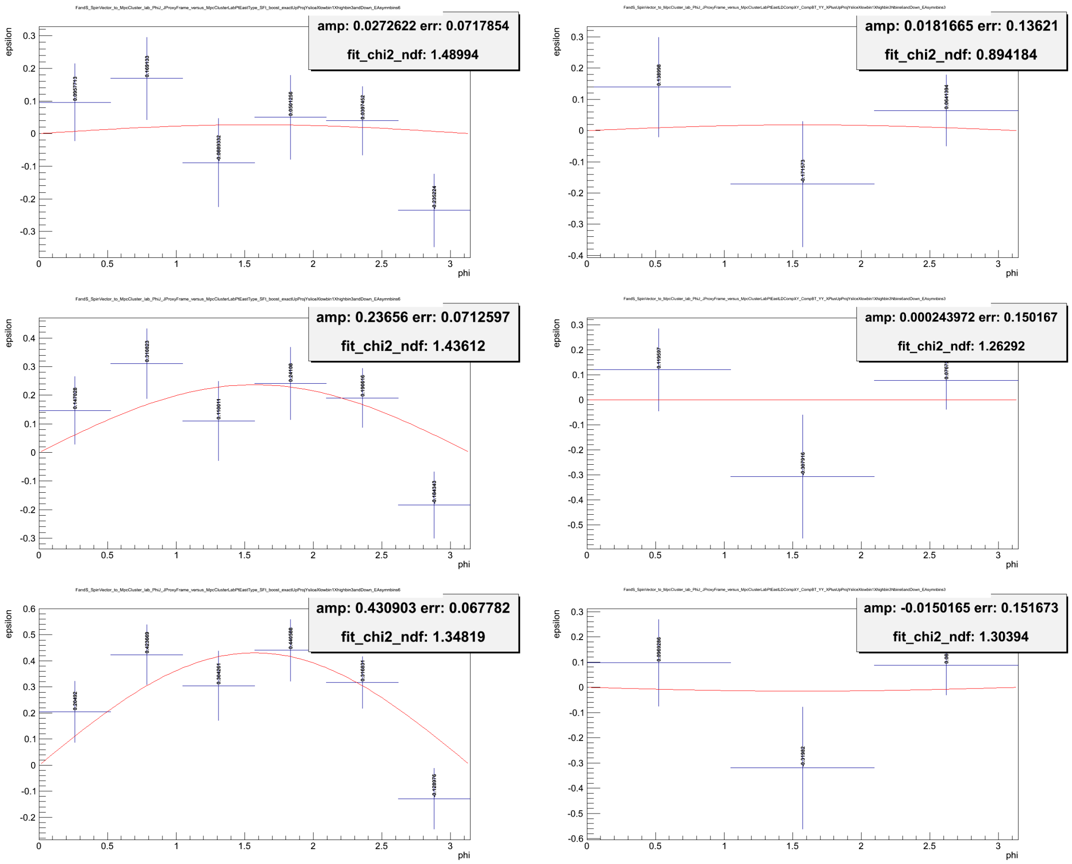

Figure 8.25 Final simulation asymmetry values. Jet in East arm. MPC π^0 with a pT between 1 GeV and 1.3 GeV. Y-axis: Square-root asymmetry values. X-axis: ϕ. Top: 0% input asymmetry. Middle: 20% input asymmetry. Bottom: 40% input asymmetry. Left: Using Pythia truth values of partonic kinematics, Right: Using approximated values for partonic kinematics.

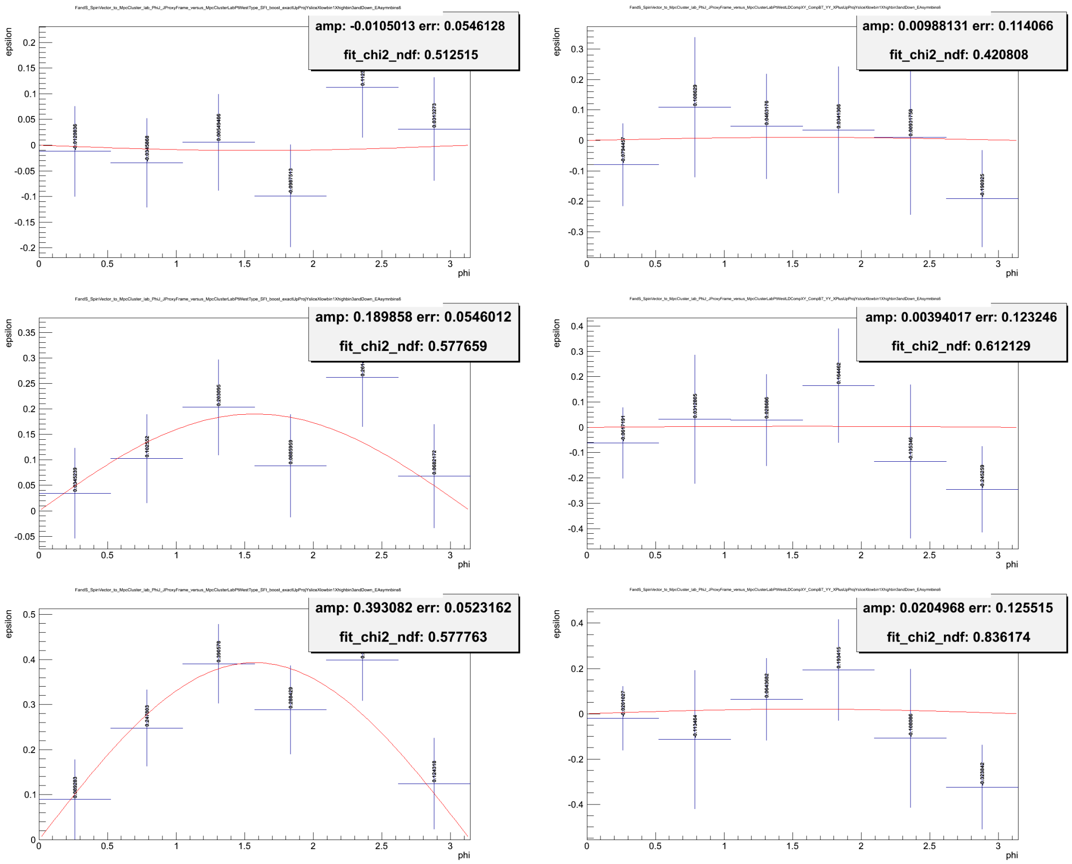

Figure 8.26 Final simulation asymmetry values. Jet in West arm. MPC π^0 with a pT between 1 GeV and 1.3 GeV. Y-axis: Square-root asymmetry values. X-axis: ϕ. Top: 0% input asymmetry. Middle: 20% input asymmetry. Bottom: 40% input asymmetry. Left: Using Pythia truth values of partonic kinematics, Right: Using approximated values for partonic kinematics.

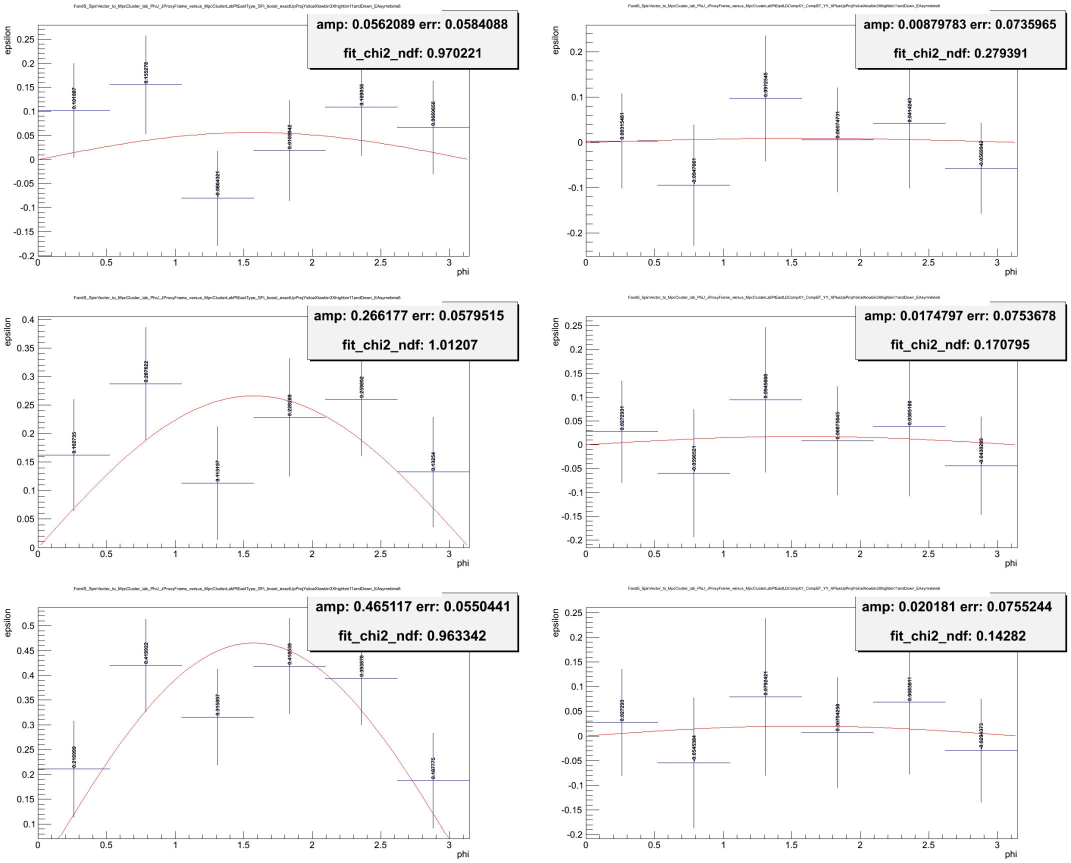

Figure 8.27 Final simulation asymmetry values. Jet in East arm. MPC π^0 with a pT between 1.3 GeV and 2.0 GeV. Y-axis: Square-root asymmetry values. X-axis: ϕ. Top: 0% input asymmetry. Middle: 20% input asymmetry. Bottom: 40% input asymmetry. Left: Using Pythia truth values of partonic kinematics, Right: Using approximated values for partonic kinematics.

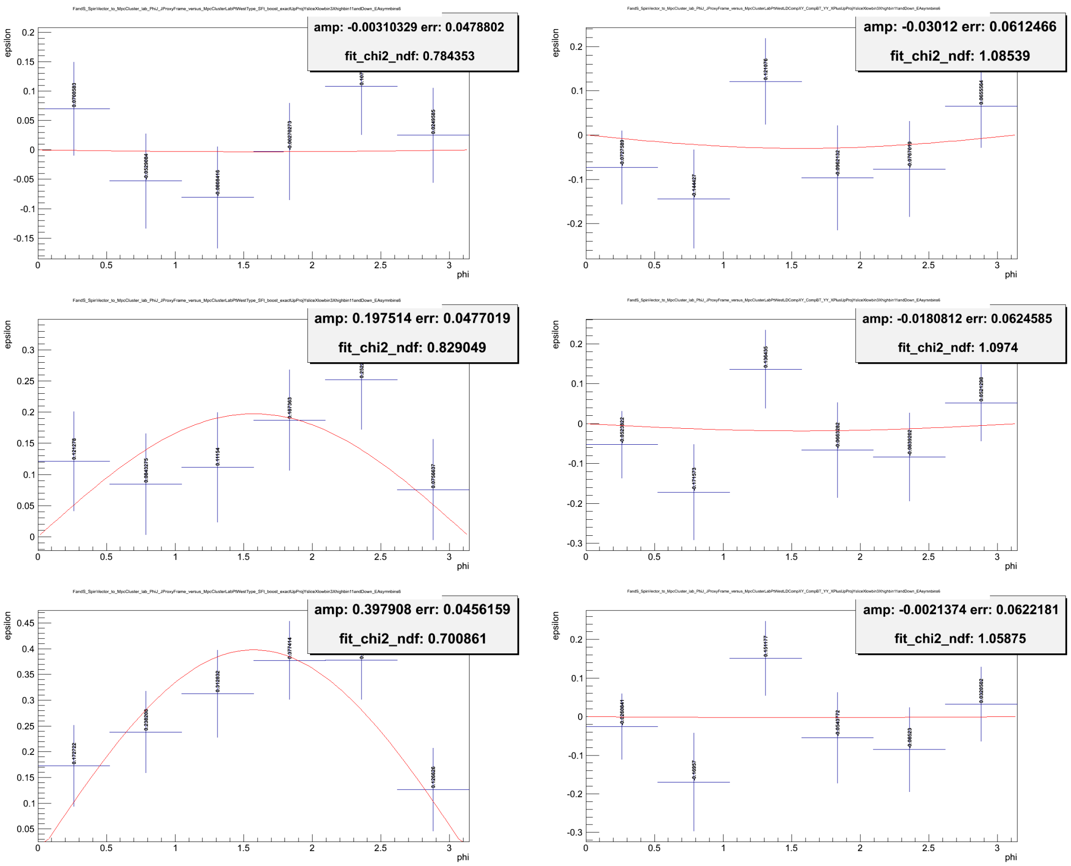

Figure 8.28 Final simulation asymmetry values. Jet in West arm. MPC π^0 with a pT between 1.3 GeV and 2.0 GeV. Y-axis: Square-root asymmetry values. X-axis: ϕ. Top: 0% input asymmetry. Middle: 20% input asymmetry. Bottom: 40% input asymmetry. Left: Using Pythia truth values of partonic kinematics, Right: Using approximated values for partonic kinematics.

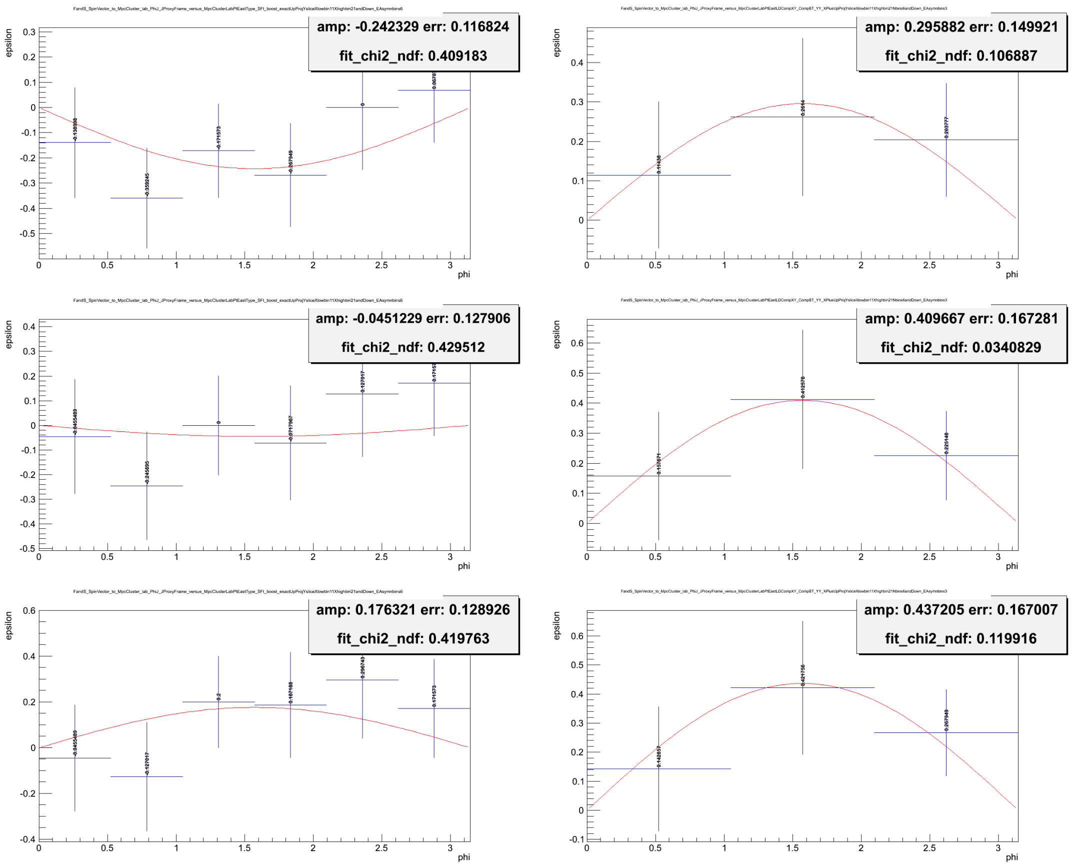

Figure 8.29 Final simulation asymmetry values. Jet in East arm. MPC π^0 with a pT between 2.0 GeV and 3.0 GeV. Y-axis: Square-root asymmetry values. X-axis: ϕ. Top: 0% input asymmetry. Middle: 20% input asymmetry. Bottom: 40% input asymmetry. Left: Using Pythia truth values of partonic kinematics, Right: Using approximated values for partonic kinematics.

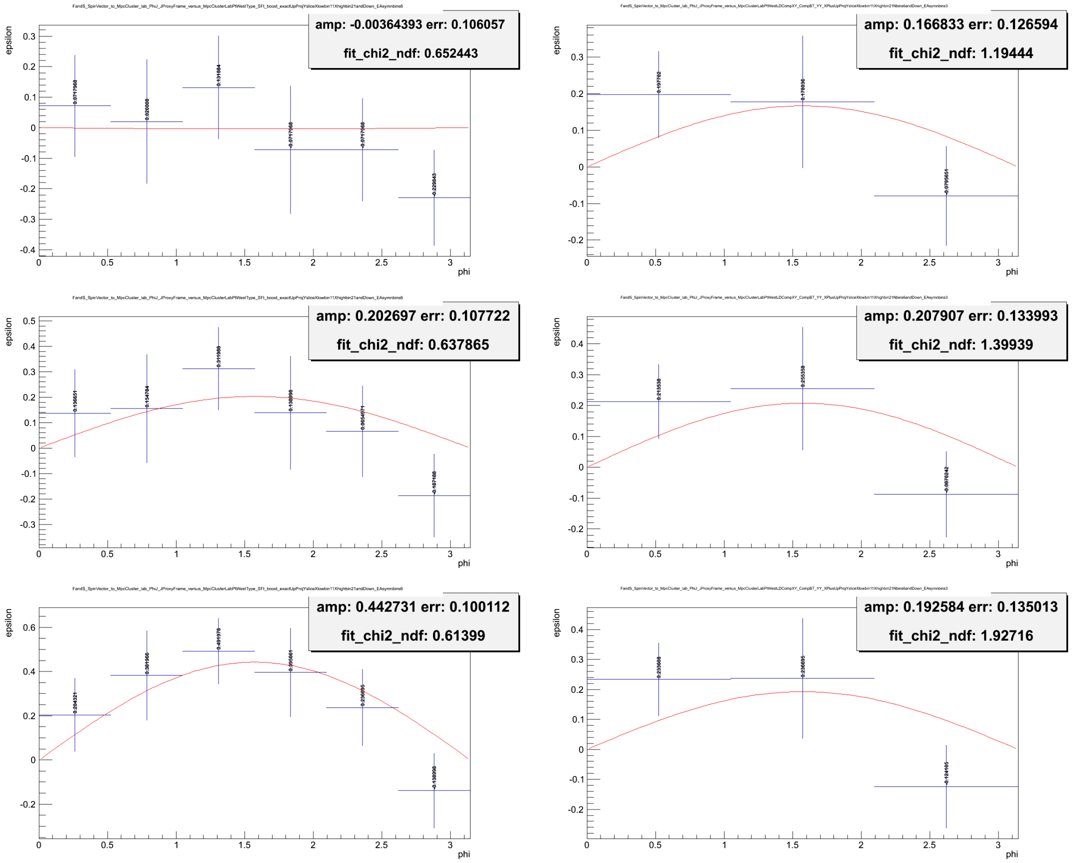

Figure 8.30 Final simulation asymmetry values. Jet in West arm. MPC π^0 with a pT between 2.0 GeV and 3.0 GeV. Y-axis: Square-root asymmetry values. X-axis: ϕ. Top: 0% input asymmetry. Middle: 20% input asymmetry. Bottom: 40% input asymmetry. Left: Using Pythia truth values of partonic kinematics, Right: Using approximated values for partonic kinematics.

Tables of the extracted fit amplitudes and amplitude errors are shown below for ease of comparison. Tables 8.1 to 8.4 shows the extracted asymmetries using the Pythia truth values for the Boost, Flip, and Swap method (left-hand sides of Figures 8.19 to 8.30). Tables 8.5 to 8.8 use only the approximated parameterizations (right-hand sides of Figures 8.19 to 8.30). A simple comparison of the input and output asymmetries shows extremely large differences and inconsistencies when the approximated parameterizations are used (Tables 8.5 to 8.8). Further discussion of the topics addressed in this section can be found in Section 8.8.

	Output Asymmetry (East, Truth, MPC π^0 p_T ranges)		
Input Asymmetry	1.0 - 1.3 GeV/c	1.3 - 2.0 GeV/c	2.0 - 3.0 GeV/c
0%	0.03 ± 0.07	0.06 ± 0.06	-0.24 ± 0.12
20%	0.24 ± 0.07	0.27 ± 0.06	-0.05 ± 0.13
40%	0.43 ± 0.07	0.47 ± 0.06	0.18 ± 0.13

Table 8.1 Jet in East arm. Pythia truth values used for Boost, Flip, and Swap procedure. MPC π^0 p_T ranges used.

	Output Asymmetry (West, Truth, MPC π^0 p_T ranges)		
Input Asymmetry	1.0 - 1.3 GeV/c	1.3 - 2.0 GeV/c	2.0 - 3.0 GeV/c
0%	-0.01 ± 0.05	0.00 ± 0.05	0.00 ± 0.13
20%	0.19 ± 0.05	0.20 ± 0.05	0.20 ± 0.13
40%	0.39 ± 0.05	0.40 ± 0.05	0.44 ± 0.14

Table 8.2 Jet in West arm. Pythia truth values used for Boost, Flip, and Swap procedure. MPC π^0 p_T ranges used.

	Output Asymmetry (East, Truth, Jet p_T ranges)		
Input Asymmetry	5.0 - 5.5 GeV/c	5.5 - 6.5 GeV/c	6.5 - 8.0 GeV/c
0%	0.07 ± 0.06	0.00 ± 0.07	-0.12 ± 0.15
20%	0.27 ± 0.06	0.21 ± 0.07	0.07 ± 0.15
40%	0.47 ± 0.06	0.43 ± 0.07	0.29 ± 0.15

Table 8.3 Jet in East arm. Pythia truth values used for Boost, Flip, and Swap procedure. Jet p_T ranges used.

	Output Asymmetry (West, Truth, Jet p_T ranges)		
Input Asymmetry	5.0 - 5.5 GeV/c	5.5 - 6.5 GeV/c	6.5 - 8.0 GeV/c
0%	-0.01 ± 0.05	-0.03 ± 0.05	-0.04 ± 0.11
20%	0.19 ± 0.05	0.18 ± 0.05	0.15 ± 0.11
40%	0.40 ± 0.05	0.38 ± 0.05	0.38 ± 0.11

Table 8.4 Jet in West arm. Pythia truth values used for Boost, Flip, and Swap procedure. Jet p_T ranges used.

	Output Asymmetry (East, Approximate, MPC π^0 p_T ranges)		
Input Asymmetry	1.0 - 1.3 GeV/c	1.3 - 2.0 GeV/c	2.0 - 3.0 GeV/c
0%	0.02 ± 0.14	0.01 ± 0.07	0.30 ± 0.15
20%	0.00 ± 0.15	0.02 ± 0.08	0.41 ± 0.17
40%	-0.02 ± 0.15	0.02 ± 0.08	0.44 ± 0.17

Table 8.5 Jet in East arm. Approximated parameterizations used for Boost, Flip, and Swap procedure. MPC π^0 p_T ranges used.

	Output Asymmetry (West, Approximate, MPC π^0 p_T ranges)		
Input Asymmetry	1.0 - 1.3 GeV/c	1.3 - 2.0 GeV/c	2.0 - 3.0 GeV/c
0%	0.01 ± 0.11	-0.03 ± 0.06	0.17 ± 0.12
20%	0.00 ± 0.12	-0.02 ± 0.06	0.21 ± 0.13
40%	0.02 ± 0.13	0.00 ± 0.06	0.19 ± 0.14

Table 8.6 Jet in West arm. Approximated parameterizations used for Boost, Flip, and Swap procedure. MPC π^0 p_T ranges used.

	Output Asymmetry (East, Approximate, Jet p_T ranges)		
Input Asymmetry	5.0 - 5.5 GeV/c	5.5 - 6.5 GeV/c	6.5 - 8.0 GeV/c
0%	-0.02 ± 0.06	0.07 ± 0.08	-0.02 ± 0.22
20%	-0.01 ± 0.07	0.08 ± 0.08	NA
40%	0.00 ± 0.07	0.10 ± 0.08	NA

Table 8.7 Jet in East arm. Approximated parameterizations used for Boost, Flip, and Swap procedure. Jet p_T ranges used.

	Output Asymmetry (West, Approximate, Jet p_T ranges)		
Input Asymmetry	5.0 - 5.5 GeV/c	5.5 - 6.5 GeV/c	6.5 - 8.0 GeV/c
0%	0.02 ± 0.05	0.02 ± 0.07	0.01 ± 0.14
20%	0.03 ± 0.05	0.05 ± 0.07	-0.01 ± 0.15
40%	0.04 ± 0.05	0.07 ± 0.07	0.03 ± 0.15

Table 8.8 Jet in West arm. Approximated parameterizations used for Boost, Flip, and Swap procedure. Jet p_T ranges used.

8.8 Conclusions

In an ideal scenario there would exist a detector system at forward rapidity (large η) that is capable of jet reconstruction at a polarized proton-proton accerator/collider facility, but this just does not exist. This novel method was pursued in order to take advantage of the current detector systems that do exist at the PHENIX experiment at RHIC. The work presented here shows the viability of this novel method. Due to the limited nature of simulated event generation (Chapter 6), the systematic errors due to the parameterization (Chapter 7) remain too large to perform a meaningful extraction of the measured asymmetry (Tables 8.5 to 8.8). New event generation techniques are required for this measurement and are being explored by the Experimental Nuclear Physics group at Iowa State University with the hope that the event generation rate can be significantly increased. A larger simulated event sample would lead to dramatically lower systematic and statistical errors imposed on the analysis due to the parameterization extraction and application procedure (Chapter 7 and Section 8.7). With lowered parameterization error one can see that the method itself is viable as the input and output asymmetries in Tables 8.1 to 8.4 are in good agreement.

Due to the unexpectedly low statistical sample of real data available (roughly four times smaller than anticipated, Section 4.7) no firm conclusions about the relative contribution of the Collins effect to the observed single spin asymmetry can be made. Run-15 at RHIC is will contain a larger sample of transversely polarized proton-proton running at $\sqrt{s} = 200\frac{GeV}{c^2}$ [71] that will increase the size of the statistical sample available for this analysis by over a factor of five. Run-15 will also include the MPC-EX upgrade to the MPC detectors which adds silicon tracking in front of the existing MPC detectors [72]. The MPC-EX upgrade will allow for charged-jet reconstruction which enables a more direct method for measuring the Collins contribution to the asymmetry.

Forward jet physics will continue to be a topic of great interest and research in the future. The PHENIX experiment plans for a large detector upgrade (sPHENIX) in tandem with upgrades to the RHIC accelerator with data taking occurring in 2021 and beyond [73]. The sPHENIX upgrade largely emphasises jet physics in the forward rapidity region which will help to further disentangle the Collins effect contribution from the observed single spin asymmetry.

BIBLIOGRAPHY

[1] Geek3. Vfpt charges plus minus thumb. `http://commons.wikimedia.org/wiki/File:VFPt_charges_plus_minus_thumb.svg`, May 2010.

[2] A. Vairo. The QCD potential. *AIP Conf.Proc.*, 964:102–109, 2007.

[3] FLIP TANEDO. Qcd and confinement. `http://www.quantumdiaries.org/2010/10/22/qcd-and-confinement/`, October 2010.

[4] J. Kang. The PHENIX experiment at RHIC. *AIP Conf.Proc.*, 494:487–492, 1999.

[5] N. Saito et al. Spin physics with the PHENIX detector system. *Nucl.Phys.*, A638:575–578, 1998.

[6] J. C. Collins. Leading twist single transverse-spin asymmetries: Drell-Yan and deep inelastic scattering. *Phys.Lett.*, B536:43–48, 2002.

[7] M. Derrick et al. Measurement of the F2 structure function in deep inelastic e+ p scattering using 1994 data from the ZEUS detector at HERA. *Z.Phys.*, C72:399–424, 1996.

[8] R. Placakyte. Parton Distribution Functions. 2011.

[9] J. Pumplin, D. Stump, J. Huston, H. Lai, P. M. Nadolsky, et al. New generation of parton distributions with uncertainties from global QCD analysis. *JHEP*, 0207:012, 2002.

[10] W. Vogelsang. Next-to-leading order evolution of transversity distributions and Soffer's inequality. *Phys.Rev.*, D57:1886–1894, 1998.

[11] G. Altarelli and G. Parisi. Asymptotic Freedom in Parton Language. *Nucl.Phys.*, B126:298, 1977.

[12] M. Anselmino, V. Barone, A. Drago, and F. Murgia. Nonstandard time reversal and transverse single spin asymmetries. 2002.

[13] A. Prokudin. Transversity Parton Distribution. *PoS*, CD12:082, 2013.

[14] M. Anselmino, M. Boglione, U. D'Alesio, A. Kotzinian, S. Melis, F. Murgia, and A. Prokudin. Transversity and collins fragmentation functions: Towards a new global analysis. *AIP Conference Proceedings*, 1149(1):465–470, 2009.

[15] M. Anselmino, M. Boglione, U. D'Alesio, S. Melis, F. Murgia, et al. Simultaneous extraction of transversity and Collins functions from new SIDIS and e+e- data. *Phys.Rev.*, D87:094019, 2013.

[16] A. Adare et al. Measurement of transverse-single-spin asymmetries for midrapidity and forward-rapidity production of hadrons in polarized p+p collisions at $\sqrt{s}$ =200 and 62.4 GeV. 2013.

[17] Z.-B. Kang and J.-W. Qiu. QCD evolution of naive-time-reversal-odd parton distribution functions. *Phys.Lett.*, B713:273–276, 2012.

[18] M. Anselmino, M. Boglione, U. D'Alesio, S. Melis, F. Murgia, et al. A_N in inclusive lepton-proton collisions. 2014. arXiv:1407.3802 [hep-ph].

[19] M. Anselmino, M. Boglione, U. D'Alesio, A. Kotzinian, F. Murgia, et al. The Role of Cahn and sivers effects in deep inelastic scattering. *Phys.Rev.*, D71:074006, 2005.

[20] D. de Florian, R. Sassot, and M. Stratmann. Global analysis of fragmentation functions for pions and kaons and their uncertainties. *Phys.Rev.*, D75:114010, 2007.

[21] S. Adler et al. Mid-rapidity neutral pion production in proton proton collisions at $\sqrt{s} =$ 200-GeV. *Phys.Rev.Lett.*, 91:241803, 2003.

[22] M. Anselmino, D. Boer, U. D'Alesio, and F. Murgia. Spin effects in the fragmentation of transversely polarized and unpolarized quarks. pages 571–575, 2000.

[23] M. Anselmino, M. Boglione, U. D'Alesio, E. Leader, S. Melis, et al. Sivers and Collins effects in polarized pp scattering processes. 2008.

[24] M. Anselmino, M. Boglione, U. D'Alesio, E. Leader, S. Melis, et al. On the potential role of the Collins effect in A_N in $pp \to \pi X$. *Nuovo Cim.*, C036(05):95–99, 2013.

[25] M. Anselmino, M. Boglione, U. D'Alesio, A. Kotzinian, F. Murgia, A. Prokudin, and C. Türk. Transversity and collins functions from sidis and e^+e^- data. *Phys. Rev. D*, 75:054032, Mar 2007.

[26] M. Anselmino, M. Boglione, U. D'Alesio, S. Melis, F. Murgia, et al. Extraction of Transversity and Collins functions. *PoS*, DIS2013:234, 2013.

[27] Brookhaven National Lab. Rhic complex, February 2013.

[28] A. Zelenski et al. The rhic optically-pumped polarized h- ion source. *AIP Conf. Proc.*, 980:221–230, 2008.

[29] A. Zelenski. Polarized sources at rhic. In *RHIC/AGS User Meeting*, 2007.

[30] International Particle Accelerator Conference IPAC12. *RHIC POLARIZED PROTON OPERATION IN RUN 12*, 2012.

[31] A. Zelenski. Rhic polarized source upgrade. In *NA PAC'13*, 2013.

[32] V. Schoefer. Rhic polarized proton operation - run 12. In *RHIC/AGS User Meeting*, 2012.

[33] V. Bargmann et al. Precession of the polarization of particles moving in a homogeneous electromagnetic field. *Physics Review Letters*, 2:435, 1959.

[34] E. Courant. Spin motion and resonances in accelerators and storage ring. Technical report, Collider-Accelerator Department, Brookhaven National Laboratory, January 2008.

[35] M. Bai. Polarized protons and siberian snakes. In *Univeristy of Virginia Nuclear Physics Seminar*, 2010.

[36] I. Alekseev et al. Run-09 pc polarimeter analysis. Technical report, Collider-Accelerator Department, Brookhaven National Laboratory, August 2010.

[37] H. Okada et al. Measurement of the analyzing power in p p elastic scattering in the peak cni region at rhic. *Phys. Lett., B*, 638:450–454, 2006.

[38] J. Koster. *Measurement Of Transverse Spin Asymmetries In Polarized Proton-Proton Collisions, And The Realization Of New Electromagnetic Calorimeters For Forward Physics.* PhD thesis, University of Illinois at Urbana-Champaign, 2010.

[39] Y. Fukao et al. Single transverse-spin asymmetry in very forward and very backward neutral particle production for polarized proton collisions at $\sqrt{s} = 200$ gev. *Physics Letters*, B650:325–330, 2007.

[40] C. Adler et al. The rhic zero degree calorimeter. *Nucl. Instrum. Meth.*, A470:488–499, 2001.

[41] M. Togawa. *Measurements of the leading neutron production in polarized pp collision at* $\sqrt{s} = 200\ GeV$. PhD thesis, Kyoto University, 2009.

[42] J. C. Hill et al. Phenix detector overview. *Nuclear Instruments and Methods in Physics Research Section A: Accelerators, Spectrometers, Detectors and Associated Equipment*, 499:469–479, 2003.

[43] M. Allen et al. Phenix inner detectors. *Nuclear Instruments and Methods in Physics Research Section A: Accelerators, Spectrometers, Detectors and Associated Equipment*, 499(2-3):549 – 559, 2003.

[44] K. Ikematsu et al. A start-timing detector for the collider experiment phenix at rhic-bnl. *Nuclear Instruments and Methods in Physics Research Section A: Accelerators, Spectrometers, Detectors and Associated Equipment*, 411(2-3):238 – 248, 1998.

[45] L. Aphecetche et al. PHENIX calorimeter. *Nucl.Instrum.Meth.*, A499:521–536, 2003.

[46] K. Adcox et al. PHENIX central arm tracking detectors. *Nucl.Instrum.Meth.*, A499:489–507, 2003.

[47] M. Aizawa et al. PHENIX central arm particle ID detectors. *Nucl.Instrum.Meth.*, A499:508–520, 2003.

[48] R. Zhu et al. A study on the properties of lead tungstate crystals. *Nuclear Instruments and Methods in Physics*, A376:319–334, 1996.

[49] Application Software Group, Computing and Networks Division, CERN. Geant – detector description and simulation tool. `http://wwwasd.web.cern.ch/wwwasd/geant/`, June 2014. Accessed: 2014-06-22.

[50] J. Perry. Global momentum scale and beam offset recalibration for the run12pp200 dataset. Technical report, PHENIX Experiment, July 2013.

[51] J. Beringer et al. Review of particle physics. *Phys. Rev. D*, 86:010001, Jul 2012.

[52] J. Perry. Pc3 and emc charged tracking recalibration for the run12pp200 dataset. Technical report, PHENIX Experiment, July 2013.

[53] J. Mitchell et al. Event reconstruction in the phenix central arm spectrometers. *Nuclear Instruments and Methods in Physics Research Section A: Accelerators, Spectrometers, Detectors and Associated Equipment*, 482(1-2):491 – 512, 2002.

[54] J. Perry. Muon piston calorimeter north arm calibration for run12 pp200 data. Technical report, PHENIX Experiment, March 2013.

[55] Brookhaven National Laboratory Nuclear and Particle Physics Program Advisory Committee. Recommendations. In *Brookhaven Nuclear and Particle Physics Program Advisory Committee Meeting*, June 2011.

[56] The PHENIX Collaboration. Phenix beam use proposal for rhic run-12 and run-13. In *Brookhaven Nuclear and Particle Physics Program Advisory Committee Meeting*, June 2011.

[57] The STAR Collaboration. Rhic beam use request for runs 12 and 13. In *Brookhaven Nuclear and Particle Physics Program Advisory Committee Meeting*, June 2011.

[58] W. Fischer. Run overview of the relativistic heavy ion collider. `http://www.agsrhichome.bnl.gov/RHIC/Runs/`, July 2014. Accessed: 2014-08-05.

[59] Sasha Lebedev. Private communication. Email, October 2013.

[60] Arbin Timilsina. Private communication. Email, October 2013.

[61] M. Tannenbaum. Hard-scattering and Jets from RHIC to LHC: A Critical review. *PoS*, LHC07:004, 2007.

[62] M. Cacciari, G. P. Salam, and G. Soyez. FastJet User Manual. *Eur.Phys.J.*, C72:1896, 2012.

[63] M. Cacciari, G. P. Salam, and G. Soyez. The Anti-k(t) jet clustering algorithm. *JHEP*, 0804:063, 2008.

[64] M. Chiu. Mpc cluster decomposition estimates at $\sqrt{s} = 200$ gev. Technical report, PHENIX Experiment, March 2013.

[65] T. Sjostrand, S. Mrenna, and P. Z. Skands. PYTHIA 6.4 Physics and Manual. *JHEP*, 0605:026, 2006.

[66] M. G. Albrow et al. Tevatron-for-LHC Report of the QCD Working Group. 2006.

[67] P. Z. Skands. Tuning Monte Carlo Generators: The Perugia Tunes. *Phys.Rev.*, D82:074018, 2010.

[68] R. S. Elke Aschenauer, John Lajoie. A comparison of the perugia6 and tunea pythia tunes for focal simulations. Technical report, PHENIX Experiment, January 2010.

[69] R. Field. The universality of pythia tune a. In *Fermilab Monte-Carlo Workshop*, June 2004.

[70] R. Field. Pythia 6.206 tune set a (cteq5l). `http://www.phys.ufl.edu/~rfield/cdf/tunes/py_tuneA.html`, November 2002. Accessed: 2014-08-05.

[71] Brookhaven National Laboratory Nuclear and Particle Physics Program Advisory Committee. Recommendations. In *Brookhaven Nuclear and Particle Physics Program Advisory Committee Meeting*, June 2014.

[72] S. Campbell et al. A proposal for the muon piston calorimeter extension (mpc-ex) to the phenix experiment at rhic. 2013.

[73] The PHENIX Collaboration. Future opportunities in p+p and p+a collisions at rhic with the forward sphenix detector. *http://www.phenix.bnl.gov/plans.html*, April 2014.